Cape Peninsula
University of Technology

Aerodynamic design and optimisation of a maritime surveillance UAV

Thesis submitted in partial fulfilment of the requirements for the degree

Master of Engineering in Mechanical Engineering

by

Rowan Earp-Jones

Faculty of Engineering

Cape Peninsula University of Technology

Supervisor: Professor Graeme Oliver

2021

I. Plagiarism Declaration

I, Rowan Earp-Jones, declare that the contents of this dissertation/thesis represent my own unaided work, and that the dissertation/thesis has not previously been submitted for academic examination towards any qualification. Furthermore, it represents my own opinions and not necessarily those of the Cape Peninsula University of Technology.

2021/10/27

Signed **Date**

II. Abstract

The aerodynamic design, development, analysis and optimisation of an Unmanned Aerial Vehicle (UAV) for the purposes of surveillance of South African oceans, is presented in this research work. Low order aerodynamic methods, such as the Vortex Lattice Method (VLM) were used to define the initial sizes and to also further develop the UAV design before starting the Computational Fluid Dynamic (CFD) analysis. This was followed by detailed 3D modelling of the aerodynamic surfaces using Solidworks. CFD software, ANSYS Fluent was then used to analyse and determine the aerodynamic coefficients and performance in more detail. Before the detailed CFD work began, a study was performed to compare the results of the Spalart-Allmaras and the Transitional SST turbulence models. The results of the study showed that the Spalart-Allmaras model, which does not model laminar flow, showed a 42% larger viscous drag than the Transitional SST turbulence model, which models laminar flow, and the transition from the laminar to turbulent regimes. For the Reynolds numbers present in the current study, the viscous drag can be a significant portion of the overall drag, thus, the Transitional SST Turbulence model was selected to better capture the transition from laminar to turbulent flow, and to better predict the viscous drag. This matches the results of other studies such as (Chen, et al., 2020). The full CFD analysis was then carried out, the results of which were used as a baseline, and as insight to possible areas of aerodynamic improvement. An updated design was realised, using the insight from the initial analysis to change the aerofoil profile used for the wing to one which maximises the extent of the laminar flow regime, reducing drag. A winglet design was also incorporated in order to reduce the extent of the observed vortices off the wingtips, increasing aerodynamic efficiency. Beyond this, the updated design also incorporated design envelopes within the fuselage for more modular sub-systems, which also resulted in a shift of the Centre of Gravity (COG), and thus a shift in the location of the wing as well. This updated design realised a performance improvement of 13.37% in the endurance over the initial design.

As a final step, ANSYS Fluent Discrete Adjoint Optimisation was used in an attempt to further reduce the drag and improve aerodynamic performance. The drawback of the ANSYS Fluent Adjoint Optimiser is that it does not currently have support for the Transitional SST Turbulence model used for the rest of the simulations. Thus, the fully laminar assumption was made for the adjoint calculations. Due to this restriction, only key areas of the UAV, that involved mostly laminar flow, were selected for the optimisation, keeping other areas constant. The decision was also made to only focus on a reduction in drag for the optimisation, as the lift of the UAV was already designed with cruising flight in mind, and an increase in lift would require a change in cruising speed, and thus a change in overall performance. The results were successful in reducing the drag by 0.25% using only small, laminar areas of the UAV. However, the

optimisation process had an adverse effect on the lift, reducing it by 2.16% in an area not selected for optimisation, namely, the wing, which resulted in an overall loss in performance. This overall loss in performance is believed to be a result of a combination of the laminar assumption used for the optimisation, and the choice to only optimise discrete areas of the UAV, instead of the UAV as a whole.

This resulted in the design iteration previous to the adjoint optimisation, namely, the improved design being selected as the final aerodynamic design. The improved design not only met but exceeded all the defined requirements.

III. Acknowledgements

I wish to thank:

- Laurie Anne-Buxton, my mother, for all her continued support and assistance. Without which, none of this would have been possible.
- Emeline Marrier d'Unienville, my fiancée, for always believing in me, for her endless help allowing me to focus on this research, for her positive words and encouragement, especially in the tougher times. And for holding down the fort during my long hours in front of the computer.
- DeltaV Aerospace, in particular, the CEO, Darren Pierce, for the financial support with regards to my masters.
- The employees of DeltaV Aerospace, particularly from the Thermo-fluids department, for their technical knowledge and assistance with matters of difficulty in this paper. And for all the fun and interesting technical discussions.

IV. Table of Contents

V. List of Figures

VI. List of Tables

VII. Abbreviations

AIAA	American Institute of Aeronautics and Astronautics
CAD	Computer Aided Design
CFD	Computational Fluid Dynamics
COG	Centre of Gravity
CPUT	Cape Peninsula University of Technology
CV	Control Volume
DNS	Direct Numerical Simulation
EEZ	Exclusive Economic Zone
FVM	Finite Volume Method
GCU	Guidance Control Unit
kg	Kilogram
LES	Large-Eddy Simulation
LLT	Lifting Line Theory
LOS	Line-of-Sight
MAC	Mean Aerodynamic Chord
MALE	Medium Altitude Long Endurance
MTOW	Maximum Take-Off Weight
NDP	National Development Plan
NLF	Natural Laminar Flow
PDE	Partial Differential Equation
RANS	Reynolds-Averaged Navier-Stokes
SACAA	South African Civil Aviation Authority
SAR	Synthetic Aperture Radar
SATCOM	Satellite Communications
SST	Shear Stress Transport
STL	Standard Triangle Language
UAV	Unmanned Aerial Vehicle
UOS	Unless Otherwise Stated
VLM	Vortex Lattice Method

VIII. Nomenclature

Ω	Mean Vorticity
Ω_{ij}	Mean Vorticity Tensor
κ	Turbulent Kinetic Energy
λ	Scaling Factor
λ_{TR}	Taper Ratio
μ	Dynamic Viscosity
μ_∞	Freestream Dynamic Viscosity
μ_t	Dynamic Eddy Viscosity
ρ_∞	Freestream Density
ρ	Density
τ	Shear Stress
ϕ	General Variable for Transport Equation
A	Area
A_{prop}	Propeller Area
AR	Aspect Ratio
b	Wingspan
$\bar{C}$	Mean Aerodynamic Chord
C_D	Coefficient of Drag
$C_{D,i}$	Coefficient of Induced Drag
C_L	Coefficient of Lift

C_M	Coefficient of pitching Moment
c_r	Root Chord
c_t	Tip Chord
$\underline{c}$	Vector of a User Specified Value that may affect converged solution
E	Energy
e	Span Efficiency Factor
F_D	Drag Force
F_L	Lift Force
L	Conditions on Each Cell
l	Reference Length
l_H	Distance between Horizontal Tail and Wing Aerodynamic Centres
l_V	Distance between Vertical Tail and Wing Aerodynamic Centres
M	Number of Cells in Problem
M_l	Moment
MAC	Mean Aerodynamic Chord
p	Pressure
Δp_{prop}	Pressure Jump Over Propeller
q_∞	Freestream Dynamic Pressure
$\underline{q}$	Vector of a User Specified Variable in a Cell
$\mathcal{R}$	Flow State
R_e	Reynolds Number

S	Wing Reference Area
S_H	Horizontal Tail Effective Area
S_M	Source Term
S_V	Vertical Tail Planform Area
T_{req}	Required Thrust
t	Time
$\widetilde{U}$	Favre-averaged Velocity
u	X-direction Component of Velocity
u_τ	Skin Friction Velocity
V	Volume
V_∞	Freestream Velocity
$\bar{V}_H$	Horizontal Tail Volume Coefficient
$\bar{V}_V$	Vertical Tail Volume Coefficient
v	Y-direction Component of Velocity
$\tilde{v}$	Kinematic Eddy Viscosity
w	Z-direction Component of Velocity
y^+	First Cell Normal Distance from Wall

CHAPTER 1: Introduction

1.1 Background

Operation Phakisa is a South African government initiative to help speed up the decision-making process, and implementation of solutions, relating to problems highlighted in the National Development Plan (NDP) of South Africa. This operation has brought to light a great need for ocean protection, surveillance and enforcement of South Africa's territorial waters (South African Government, 2018). This need has arisen for a few reasons, the main reason being that South Africa is losing approximately R6-9.8 billion (405-662 million USD) per year to illegal fishing (Glazewski, 2013) (Schraader, 2013).

Piracy and illegal fishing have been a long-standing problem off the coast of South Africa, as illustrated by the many articles published on the topic, with dates ranging from 2013 to current. Some articles even mention the problem existing as early as 2009 (ENCA, 2014). Part of the reason for this, is that South Africa has a large amount of revenue generating ocean area to patrol and monitor, approximately 1.5 million square kilometres of an Exclusive Economic Zone (EEZ), an area larger than its land mass (Kings, 2016). The EEZ being the area of ocean where South Africa owns all the resources, this area extends 370 kilometres off the shores of South Africa (Kings, 2016). Currently, South Africa only employs 14 ships, 4 manned helicopters and 5 manned fixed wing aircraft (Kings, 2016). These surveillance vehicles are too few, outdated and expensive for the purpose of covering this area of ocean. But above all, these vehicles appear incapable of doing enough in order to alleviate the problem at hand. In other words, South Africa requires more surveillance and patrol off its coastline in order to better understand and monitor what is happening in its own oceans. The South African government also recognises this need and is attempting to solve it by investing R462.71 billion (31.3 billion USD) into extending earth observation capacity and implementing a coasting information system (Operation Phakisa, 2014). It can clearly be seen that the problem requires better solutions than what is currently available.

This brings forth the beginning stages of the design, optimisation and analysis of a fixed wing unmanned aerial platform. These platforms can cover areas of land (or water) with a range of up to 15 000 km's efficiently (Northrop Grumman, 2016). They can give law enforcement a "birds eye view" of the oceans using sensors and cameras. They are also relatively cheap when compared to manned aerial platforms, which require higher running costs, mainly since a human is required to be always present in the cockpit during flight (AUVSI News, 2013). This gives rise to safety, certification and maintenance concerns that do not exist with an unmanned platform.

The purpose of this Unmanned Aerial Vehicle (UAV) will, of course, not be to replace naval vessels, but to assist in the patrolling and surveillance of South Africa's EEZ. A network of

UAVs will, in theory, be able to cover and monitor the entirety of South Africa's EEZ, as well as being able to inform the naval vessels of any possible illegal activities and the location of such activities which would allow the naval vessels to operate in more of a "patrol and respond" position rather than surveillance.

The challenge, and research aspects with regards to the UAVs aerodynamic development and optimisation, comes into play when considering the unique requirements of ocean surveillance in South Africa's EEZ. Firstly, as previously stated, the EEZ extends 370 kilometres off the coast of South Africa, this immediately poses the problem that the UAV will require a minimum range of approximately 740 kilometres, just to get to the end of the EEZ and back, with no loiter or mission time included. Furthermore, the UAV will have to meet this range requirement while facing generally higher wind speeds, than that of a UAV flying over a land mass (Manwell, et al., 2010). The UAV will of course, have to meet these requirements, while being as cost effective and efficient as possible. For the UAV to be as efficient as possible, an elaborate and optimised aerodynamic design will be required. This will provide the best range and endurance capabilities, and hopefully result in an optimised design catered just for surveillance of South Africa's EEZ.

1.2 Literature Review

1.2.1 Aerodynamic Design Considerations

1.2.1.1 Requirements Definition

Before work towards the design of the UAV can commence, the requirements need to be properly and accurately defined, as these will help determine the final shape and size of the UAV (Panagiotou, et al., 2016). Requirements need to be defined based on criteria such as mission definition, flight profile, endurance and range requirements, payload requirements, transportation and serviceability requirements, costs etc.

Most studies perform investigations as to what type of mission the UAV is to carry out, and use this as a starting point for the definition of the requirements (Panagiotou, et al., 2016) (Lee, 2004) (Bravo-Mosquera, et al., 2017). The requirements are typically defined in a table such as Table 1-1 below. It should be noted that the values in this table are a current assumption as to what the actual UAV requirements will be. The specific requirements, and reasoning behind them are given in CHAPTER 2:.

Table 1-1: Example Requirements Table (To be properly defined later)

REQUIREMENT	VALUE
Endurance [h]	>20
Range [km]	>1300
Communications Range [km]	>=370
Maximum Take-Off Weight [kg]	<250
Maximum Payload Mass [kg]	20
Stall Speed [m/s]	<25
Cruising Speed [m/s]	30 - 40
Cruising Altitude [m]	4000-5000
Service Ceiling [m]	<6000
Absolute Ceiling [m]	<10 000

1.2.1.2 Size, Weight and Payload Considerations

Once the requirements are defined, iterative calculations are normally started in order to estimate the weight and size of the UAV (unless these parameters are already defined in the requirements section) (Panagiotou, et al., 2016) (Kontogiannis & Ekaterinaris, 2013) (Panagiotou, et al., 2018).

The size of the UAV will fall into one of four size groups: large, medium, small and micro (Bravo-Mosquera, et al., 2017). Again, the mission profile and requirements will help determine the size bracket that the UAV will fit into, and the criteria for the size bracket is a combination of both mass and wingspan (Lee, 2004). Examples of UAVs in different size groups are included in section 1.2.3 below.

The requirements will also help determine the type of payload(s) to be carried by the UAV, which will also directly affect the mass and size. As a simple example, a common payload for a surveillance aircraft is that of a camera (see section 1.4.1 below).

1.2.2 Computational Considerations

1.2.2.1 Geometry Modelling and Fluid Domain

In order for a CFD study to be performed, the geometry of the UAV will have to be modelled in 3D computer Aided Design (CAD) software. The modelling of a UAV can be challenging as UAVs can frequently involve compound curvature and organic shapes (Kontogiannis & Ekaterinaris, 2013) (Panagiotou, et al., 2016) (Carvalho, 2016). Complex surfacing and multibody techniques will be required in the CAD software package in order to properly and accurately model the geometry.

In order to be solved using CFD, a finite computation fluid domain around the aircraft will be required. The size and shape of this domain can directly impact the results of the CFD simulation, and the fluid domains shape and size around the aircraft will have to be carefully

selected based on current aircraft CFD practice or a validation case. Because a UAV is symmetrical about its centre line, most studies, when looking at UAV aerodynamics without cross wind or propeller effects, model only half the UAV geometry, using the symmetry to their advantage (Carvalho, 2016) (Kontogiannis & Ekaterinaris, 2013) (Panagiotou, et al., 2016) (Panagiotou, et al., 2018). This allows only half the model to be considered, without affecting the results, reducing computational requirements on the study to be carried out, which can mean either a finer grid may be used, increasing accuracy, or half the number of cells will be required, reducing time required per computation. Of course, a combination of these two advantages may also be used. Bodies may also be added into the fluid domain as grid sizing bodies, which help control the size of the grid in areas of interest in the simulation (Bravo-Mosquera, et al., 2017). An example of a fluid domain with aircraft geometry, fluid domain and grid control bodies are shown in Figure 1-1 below.

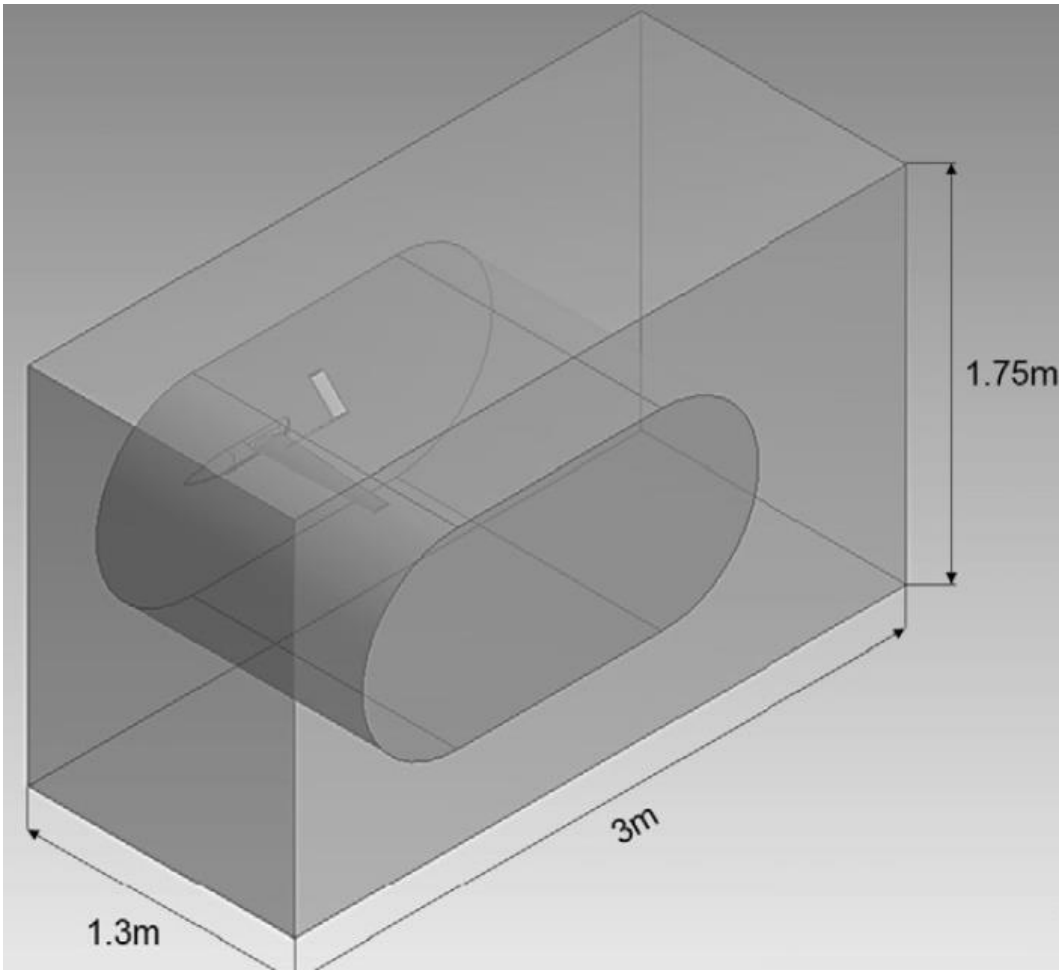

Figure 1-1: Example of a Fluid Domain with Aircraft Geometry (Bravo-Mosquera, et al., 2017)

1.2.2.2 Grid Generation and Associated Considerations

Possibly the most important step in the CFD workflow, is that of the grid generation. The grid needs to be sufficiently fine in key flow areas, particularly where high gradients may be present, or where certain effects such as flow separation may occur, in order to accurately capture the physics. But the grid must also be coarse in areas where there are no large gradients or

interesting flow phenomena, in order to reduce the total cell count, and thus solve time per calculation. Total cell count can vary greatly from simulation to simulation, with current literature using anywhere between 6 (Panagiotou, et al., 2016) to 22 (Carvalho, 2016) million cells in order to accurately solve the problem.

Certain key areas need to be considered for external aerodynamic simulation grid generation, particularly for aircraft. The most critical area likely being that of the grid generation near the wall of the aircraft. In this area, in order to accurately predict the boundary layer, and possible flow separation phenomena, a large number of cells is frequently needed. With the first layer height off the wall of the aircraft commonly being set as small as 10-2 x 10^{-5}. For example, (Panagiotou, et al., 2018) sets the first layer cell height off the wall at 2.5 x 10^{-5}, with 20 inflation layers in order to resolve the boundary layer as accurately as possible.

Another key area for the grid generation is that in the wake of the aircraft, particularly near the wing tips and fuselage. A finer grid is needed in these areas in order to accurately resolve phenomena such as wing tip vortices and the flow in the wake of the fuselage.

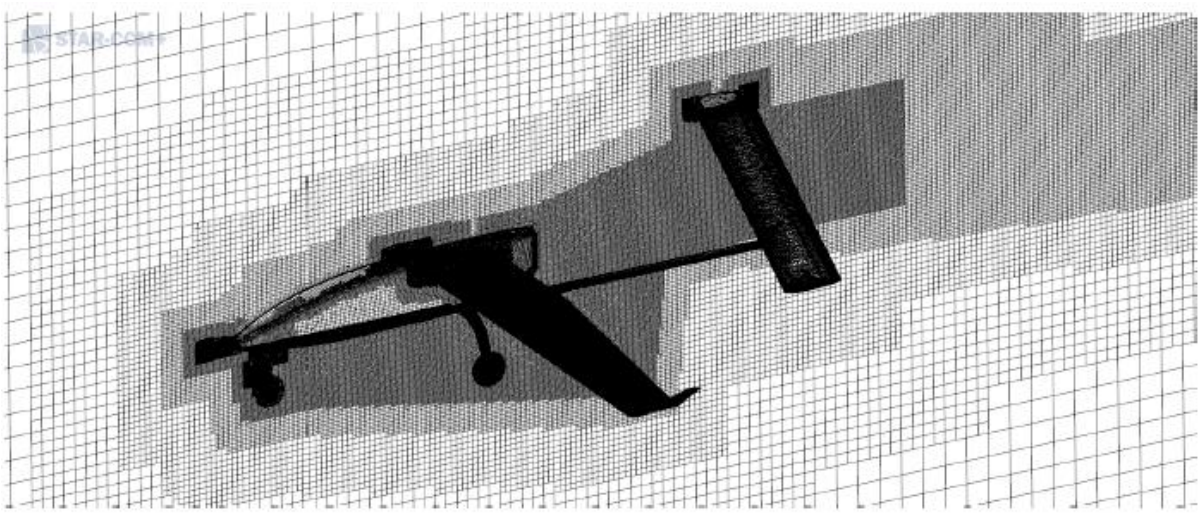

Figure 1-2: Wake Refinement Example (Carvalho, 2016)

Besides the general cell size considerations, though also needs to be put into what shape of cell will be employed.

1.2.2.3 Solution and Post-Processing

Once the geometry and grid generation are complete, the setup of the solution is the next key step. Decisions need to be made here such as what type of solution method will be employed, what turbulence model will be chosen (if applicable), what boundary conditions will be employed, and what factors and residuals of the solution need to be monitored.

Either Direct Numerical Simulation (DNS), Large-Eddy Simulation (LES) or Reynolds-Averaged Navier-Stokes solution methods can be employed in order to solve the flow field. For most practical cases involving real world complex geometry, the RANS method is

employed (Tu, et al., 2018). The reason for this is that both DNS, and LES are computationally expensive, and will not be practical, or maybe even possible for most real-world cases, and are seen as more “advanced” techniques (Tu, et al., 2018). All the literature already mentioned involving CFD has used the RANS method.

With RANS, also comes the selection of a turbulence model (Tu, et al., 2018). The turbulence model is used in order to close the equations and time-average the solution, particularly in the turbulent zones of the flow (ANSYS INC, 2018). Without going into great detail on all the turbulence models available, the referenced literature, including (Carvalho, 2016), (Kontogiannis & Ekaterinaris, 2013) and (Panagiotou, et al., 2016), which all involve turbulence modelling on aircraft and UAVs, select one of two turbulence models, either the Spalart-Allmaras (SA) or the k-ω SST transitional turbulence model. It can be seen by the various articles, using either of these models for different reasons, that the turbulence model best suited to the particular case can vary based on geometry and conditions. Therefore, careful consideration will have to be given regarding the turbulence model choice for the UAV analysis to be carried out.

As for the post processing, this step in the process is not one of the most critical, it is however, still important, as correct post-processing can directly result in easier communication and identification of areas of interest, particular flow phenomena and possible problems arising in the simulation. For example, the post-processing can help visualise the formation of vortices off the tip of a wing as in (Carvalho, 2016), or flow separation as in (Panagiotou, et al., 2016). Examples of images of the post-processing of these two phenomena from the mentioned articles is shown in Figure 1-3 and Figure 1-4 below.

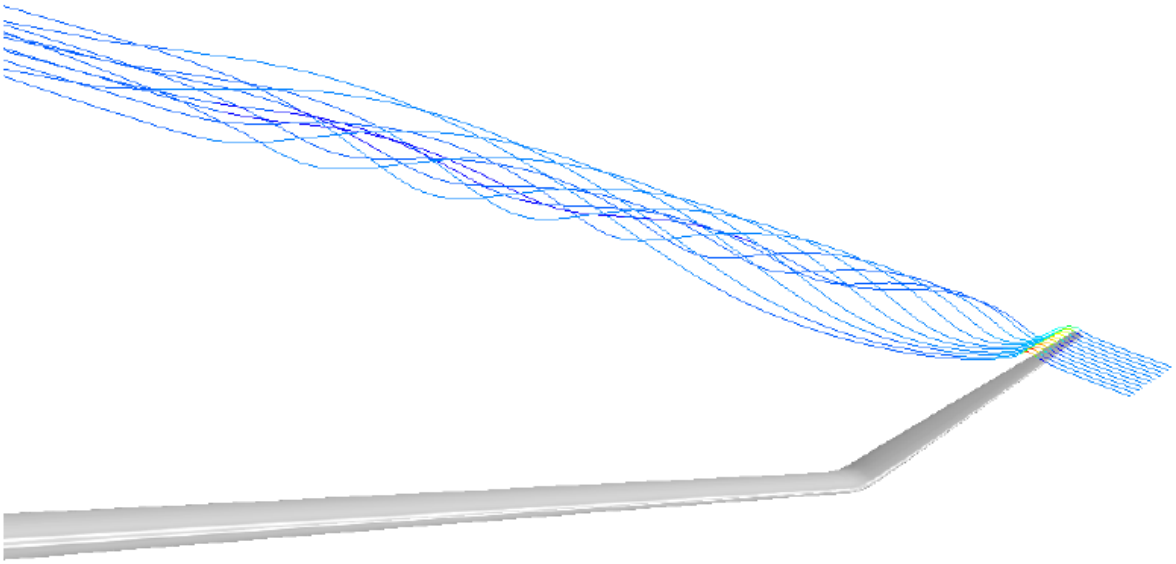

Figure 1-3: Post-Processing showing Wingtip Vortex Formation (Carvalho, 2016)

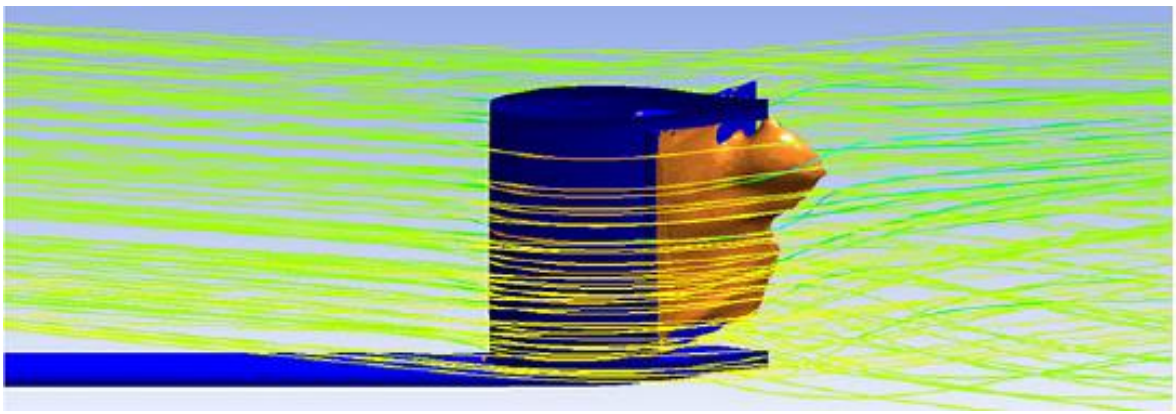

Figure 1-4: Post-Processing showing flow separation on a control surface (Orange region) (Panagiotou, et al., 2016)

1.2.2.4 Verification and Validation

When performing numerical simulations, certain errors and uncertainties may present themselves (Tu, et al., 2018). Any CFD simulations, therefore, need to be properly validated and verified in order to be credible (Tu, et al., 2018). According to (Tu, et al., 2018), verification and validation is a means to quantitatively estimate the errors and uncertainties of a CFD solution. Verification and validation are two different processes, both need to be performed in order for a CFD simulation to be credible.

Most of the current studies using CFD for UAV aerodynamics problems compare experimental results of a 2D wing section, to a 2D simulation in order to validate the boundary conditions and turbulence models used (Kontogiannis & Ekaterinaris, 2013). Another option for validation is to simulate a more complicated case than what is being undertaken, which is well documented and has wind tunnel results available, and then to compare the results of the simulation to the wind tunnel results. Verification normally arises as a grid independency study, which compares the results sensitivity to the number of cells in the fluid domain (Carvalho, 2016).

Some studies, where resources are available, also prepare wind tunnel models in order to more directly compare the CFD results to real world results (Bravo-Mosquera, et al., 2017). This is the most preferred and accurate method of validating CFD results if the wind tunnel tests are of a high quality.

1.2.3 Relevant Existing UAVs

To see what is currently available in terms of availability, technology and capability, some existing UAVs relevant to the research topic are presented here in various size groups. Where possible, UAVs of local origin (South African) will be presented. It should also be noted that the focus of the UAVs tip more towards the large variants, as they are the only UAVs capable of the range and endurance requirements for maritime surveillance.

1.2.3.1 Northrop Grumman MQ-4C Triton

A UAV designed specifically for ocean and coastal surveillance, falling into the large UAV category, is the MQ-4C Triton, built by Northrop Grumman (Northrop Grumman, 2016). This is one of the few UAVs found designed specifically for maritime surveillance, shown in Figure 1-5 below. The specifications of the Triton are given in Table 1-2 below. It should be noted that the Triton uses Satellite Communications (SATCOM) in order to communicate with its associated ground station, allowing its large communication range capabilities (Jane's By IHS Markit, 2017).

Figure 1-5: Northrop Grumman MQ-4C Triton (Northrop Grumman, n.d.)

Table 1-2: Northrop Grumman MQ-4C Triton (Northrop Grumman, 2016)

PROPERTY	VALUE
Wingspan [m]	39.9
Length [m]	14.5
Maximum Take-Off Weight (MTOW) [kg]	14 628
Maximum Velocity [m/s]	170
Endurance [h]	24+
Service Ceiling [ft.]	56 500
Maximum Payload [kg]	1089
Range [km]	15 186

1.2.3.2 General Atomics MQ-9 Reaper

Another reconnaissance UAV is the General Atomics MQ-9 Reaper, as seen in Figure 1-6 below. Also falling into the large UAV category, however, coming in slightly smaller in size and mass than the Triton, as can be seen by Table 1-3 below. The Reaper also uses SATCOM in order to maintain its communications link over extended ranges (Erwin, 2017).

Figure 1-6: General Atomics MQ-9 Reaper (Wikipedia, n.d.)

Table 1-3: General Atomics MQ-9 Reaper Specifications (U.S. AIR FORCE, 2015)

PROPERTY	VALUE
Wingspan [m]	20.1
Length [m]	11
Maximum Take-Off Weight (MTOW) [kg]	4760
Maximum Velocity [m/s]	134
Endurance [h]	14
Service Ceiling [ft.]	50 000
Maximum Payload [kg]	1701
Range [km]	1850

1.2.3.3 Denel Dynamics Bateleur

The first local UAV featuring on this list, is the Denel Dynamics Bateleur, which is both designed and built by Denel Dynamics (Wikipedia, n.d.). This UAV also falls into the large category, and limited information is available, but the UAV is a strong local contender for the local air force and maritime surveillance. However, the Bateleur is expensive, and to the authors knowledge, is not yet in use because of its cost (Wikipedia, n.d.). The Bateleur also

uses SATCOM to obtain an action radius of 750 km (Wikipedia, n.d.). The Bateleur can be seen in Figure 1-7 below, with its available specifications given in Table 1-4 below.

Figure 1-7: Denel Dynamics Bateleur (Wikipedia, n.d.)

Table 1-4: Denel Dynamics Bateleur Specifications (Wikipedia, n.d.)

PROPERTY	VALUE
Wingspan [m]	15
Length [m]	N/A
Maximum Take-Off Weight (MTOW) [kg]	1000
Maximum Velocity [m/s]	69.4
Endurance [h]	18-24
Service Ceiling [ft.]	26 000
Maximum Payload [kg]	N/A
Range [km]	750

1.2.3.4 Alti Transition

The Alti Transition is another locally produced UAV, produced by Alti in Knysna, South Africa (Alti, n.d.). The Alti is smaller on the scale than the rest of the UAVs considered, and thus, falls into the medium sized UAV category. The Transition also has the unique feature of being able to take off vertically (Alti, n.d.), and is one of the few non-military grade UAVs. The Transition does not use SATCOM for communications, and thus has a limited Line of Sight (LOS) range (Alti, n.d.).

Figure 1-8: Alti Transition (Alti, n.d.)

Table 1-5: Alti Transition Specifications (Alti, n.d.)

PROPERTY	VALUE
Wingspan [m]	3
Length [m]	2.3
Maximum Take-Off Weight (MTOW) [kg]	18
Maximum Velocity [m/s]	N/A
Endurance [h]	12
Service Ceiling [ft.]	13 000
Maximum Payload [kg]	1.5
Range [km]	150

1.2.3.5 AeroVironment RQ-11 Raven

For comparison, at least one UAV from the small size range had to be considered. The AeroVironment RQ-11 Raven is a small UAV, capable of being launched by hand (AeroVironment, n.d.). The raven is highly limited in terms of range and endurance because of its size, but is still suitable for its purpose, which is a small surveillance UAV capable of being launched by hand from troops on the ground (AeroVironment, n.d.).

Figure 1-9: AeroVironment RQ-11 Raven (AeroVironment, n.d.)

Table 1-6: AeroVironment RQ-11 Raven Specifications (AeroVironment, n.d.)

PROPERTY	VALUE
Wingspan [m]	1.4
Length [m]	0.9
Maximum Take-Off Weight (MTOW) [kg]	1.9
Maximum Velocity [m/s]	22.5
Endurance [h]	1.5
Service Ceiling [ft.]	14 000
Maximum Payload [kg]	N/A
Range [km]	10

1.2.4 Summary of Existing UAVs

The question might be asked why none of the UAVs (or other's) are not suitable for the project at hand. The answer is that some are but are not chosen for the topic for a particular reason, or several reasons. These reasons are summarised below in Table 1-7. From this table, it can be seen why it was chosen to develop a UAV specifically for the purpose at hand.

Of all the sources and research mentioned in the literature review sections prior to section 1.2.3, it should be noted that none of the UAVs were designed to meet the endurance and range requirements laid out in this proposal, this is why none of the UAVs in current research can be chosen as the baseline configuration for this development.

Table 1-7: Reasoning for Existing UAV not being suitable for application

UAV	Reasoning for not being suitable
Northrop Grumman MQ-4C Triton	• US military UAV • Expensive to purchase and operate • Overdesigned for current requirements • Provides weapon capabilities not required for this project
General Atomics MQ-9 Reaper	• US military UAV • Expensive to purchase and operate • Overdesigned for current requirements • Provides weapon capabilities not required for this project
Denel Dynamics Bateleur	• Expensive to purchase and operate, although not as expensive as the previous 2 options • Range barely enough to get to end of EEZ and return, let alone loiter in EEZ
Alti Transition	• Requirements for range and endurance not met
AeroVironment RQ-11 Raven	• Requirements for range and endurance not met

1.3 Objectives of the research

The objective of this research is to present the study of the aerodynamic design and optimisation of a UAV developed specifically for the purpose of maritime surveillance off the coasts of South Africa, using computational techniques such as CFD. Solidworks 2018 Computer Aided Design (CAD) software will be used to model the aircraft, and Ansys Fluent 2019R2 will be the CFD software used to solve the external aerodynamics analysis.

The added objective of studying the UAV aerodynamics, and how particular geometric changes can affect the flow patterns, and thus aerodynamic performance of the vehicle, is to be used to gain a deeper understanding of the various factors that affect flight performance.

There is also a particular workflow to work to when running CFD computations as stated by (Ali, 2018) and (CFD Support, n.d.). These workflows are necessary to ensure accuracy of the simulations and consistent information for presentation. It will be required that this workflow is adhered to in order to ensure accurate and credible results.

1.4 Research Design and Methodology

1.4.1 Requirements Definition

To provide an objective to work towards, as a starting point, the requirements of the UAV will have to first be clearly defined and documented, this goes in line with current literature, of which all the journal articles involving design first set out the requirements as seen in section

1.2. This will help with the UAV payload and systems selection, as well as with the initial design of the aircraft. The requirements will of course be based off the goal of designing this aircraft as a UAV specifically for surveillance of South Africa's EEZ.

1.4.2 Systems Selection

Again, with the main goal of the UAV being surveillance of South Africa's EEZ, the UAV will have to carry a payload, and associated systems, in order to meet this goal. A surveillance payload, such as a camera, will have to be selected, along with associated systems such as communications equipment capable of meeting the range requirements to provide live video feedback and UAV control during flight. Camera payloads are normally placed externally of the aircraft in the flow of air, to allow for a greater field of view. This means the payload shape and size will have to be included in the aerodynamics study as it will affect the aerodynamic performance of the UAV. An example of a UAV camera is shown in Figure 1-10 below.

Figure 1-10: UAV Camera Payload (UAV Factory, n.d.)

The UAV will also require a motor to be selected, along with a fuel tank, the weight and size of the motor and fuel tank will have a direct effect on the shape, size and performance of the UAV, as well as its ability to meet its requirements, this will have to be considered for the initial design as well as the mass, endurance and range calculations.

Where specific systems do not have to be defined, the general shape and size of common systems will be used as an average for the UAV CAD modelling and performance calculations.

1.4.3 Initial Design Layout and Modelling

It can be seen from section 1.2 that several shapes and sizes of UAVs can exist, depending on their requirements and payloads etc. Using the requirements and systems defined in the previous 2 stages, the initial configuration and design of the UAV can be carried out. Common aircraft sizing methods and calculations can be used in order to help determine the initial size and design of the UAV. This can involve something as general and simple as Lifting Line Theory (LLT) calculations, or more advanced panel aerodynamics methods such as that used by XFLR5 in order to predict and confirm the initial aerodynamics and size of the UAV.

Solidworks 2018 CAD software will be used in order to physically model the geometry of the UAV and generate items such as the computational domain and any grid control volumes.

1.4.4 CFD of Initial Design

Once the 3D model of the UAVs initial configuration has been modelled, the first CFD set of analysis can be performed as the benchmark. CFD studies normally follow a particular workflow, the workflow to be carried out for this study is given in Figure 1-11 below, and is based off the recommendations from (ANSYS INC, 2018) and the workflow in (Cogan, 2016).

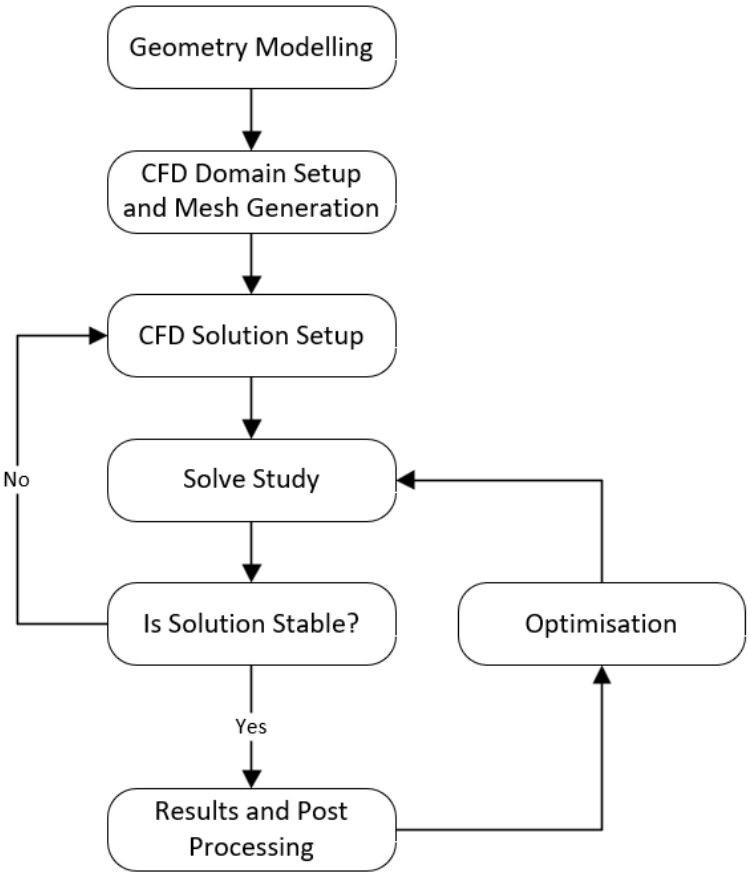

Figure 1-11: Proposed CFD Workflow

The CFD of the initial configuration will be run at various angles of attack (to be confirmed in the actual CFD study) and the drag and lift coefficients at each angle of attack will be calculated and used as the baseline values. Certain flow phenomena, such as flow separation and vortex generation off the wingtips will also be recorded and used as baseline data, as these are possible areas of high drag, and areas that can be focussed on for improvement in the optimisation process. The calculations involved will be steady state, and only half the fluid domain will be modelled as the UAV will be symmetrical down its centre line, and no crosswind effects are to be considered, this follows the common methods employed in current literature.

1.4.5 Improvement and Optimisation

As seen in the workflow given in Figure 1-11 above, once the initial geometry has been analysed, and baseline results are obtained, insights gained from this analysis can be used in order to improve and optimise the design. The improvement of the initial design can be carried out by using the insights gained from the initial design analysis in order to update the geometry of the UAV for better aerodynamic performance. The CFD process is then repeated with the adjusted geometry and compared to the baseline solution (or the previously improved solution). This process is repeated until no further improvement to the aerodynamic performance is deemed necessary or where the results improvement starts to become negligible or even detrimental to the aerodynamic performance. For the purposes of this study, this process of using insight from the obtained CFD results, and sound engineering knowledge to attempt to improve the design is referred to as “improvement”.

Beyond these methods of aerodynamic improvement mentioned above, ANSYS Fluent also includes its own optimisation methods and algorithms in the form of two mesh morphing methods (ANSYS INC, 2018). These tools provided by ANSYS Fluent, known as the adjoint solver and mesh morpher/optimiser can modify the mesh and fluid domain in order to optimise the geometry for certain goals being set (ANSYS INC, 2018). The goals to be considered for this study will be that of an increase in lift (if deemed necessary), and a decrease in drag under cruise conditions, with the overall goal being to improve the range and endurance of the aircraft. It is important to distinguish between the two methods of improvement mentioned here, as such, this method using the ANSYS Fluent mesh morpher will be referred to as “optimisation” for this study.

1.4.6 Verification and Validation

As stated in section 1.2.2.4, in order for the CFD work to be considered credible, verification and validation will have to be carried out in order to quantify the results against published and or experimental data and confirm the fidelity of the numerical calculations. In terms of verification, a grid independency study will be carried out in order to quantify any discretization errors that may be present in the numerical results. This goes along with common practice in the currently available literature.

For the validation, there are 3 options, the first being to compare the numerical results against another calculation method, such as the panel method used by XFRL5, or compare the 3D CFD results of the wing section against published 2D data of the same wing section. This method does not give directly comparable results to the CFD work performed but will give a good indication as to whether the calculations are fairly accurate and trending towards what can be expected. This method involves relatively little effort in terms of time when compared to the methods below, but it is not the most accurate method.

The second option is to take a well-documented research study/case, that has wind tunnel results and published data available (including the geometry used), and to perform CFD simulations on this geometry and compare the results to the published wind tunnel data. The case being analysed should involve similar physics to the actual simulations that are required to be performed, but preferably be more complex. The results and errors between the wind tunnel results and the simulation can then be assumed to be similar to the actual simulation to be carried out. This option can provide acceptable accuracy, and can require a fair amount of time, but it does not require budget. This method is most used in current literature, as seen in section 1.2.2.

The third option is to build an actual scale model of the aircraft geometry and use a wind tunnel to record results and directly compare these results to the CFD calculation performed. This method is the more accurate method if the performed test is done to a high quality but requires a great amount of time and money. The aircraft scale model will have to be manufactured using techniques possibly including 3D printing and CNC machining, and access will be needed to a large wind tunnel in order to accurately record the data and directly compare results.

1.5 Delineation of the Research

- The research and computational simulations will have to be conducted using whatever computer resources are available. Simulations, particularly external aerodynamic simulations requiring high accuracy, can require substantial amounts of computational storage and power, and the research accuracy is limited to what computational power is available.
- Surveillance UAVs are generally low speed aircraft; thus, the research will be limited to the subsonic flow regime.
- Simulations will not involve internal flow or cooling flow such as engine cooling. Effects such as that of the UAV propeller, or sideways flow (also known as sideslip), will not be considered. The study will focus solely on improving and optimising the UAV flight under normal (cruising) flight conditions.
- The study will focus solely on steady state simulations at various angles of attack, and dynamic simulations will not be performed. This can be the topic of future research if deemed necessary.

- The optimisation of the UAV will be performed at a single angle of attack and speed, the angle of attack and speed to be selected will be the angle and speed at which the initial design of the UAV is most efficient, or its cruising angle of attack.
- As the study focuses on cruising flight, where not much is happening in terms of control surfaces, the control surfaces do not need to be designed or included in this study.
- Where considerations need to be made to items such as UAV mass and component selection. The detailed specification of these parts will not be part of this study. The mass of payloads, engine, and fuel will be stated based on existing products that meet the requirements and be used in the endurance and range calculations.
- As the structural design will make a difference to the centre of gravity of the aircraft, the centre of gravity and aerodynamic neutral point of the aircraft will not be looked at in detail. Crude assumptions can still be made in order to estimate a rudimentary centre of gravity, and the neutral point (and all relevant surfaces) must still be placed in an aerodynamically “correct” position relative to this point.
- An assumed payload will be selected and included as part of the simulations, as this forms part of the aerodynamics study as the payload (e.g. camera), is normally exposed to the flow.

CHAPTER 2: UAV Requirements Definition

Before the aerodynamic design work towards the baseline UAV concept can begin, the requirements the UAV will have to meet need to be accurately and properly defined. For the requirements to be accurately defined, the mission profile, as well as mission specifics for the UAV, need to be kept in mind at all times. This section presents an explanation of the expected mission profile and specifics, in order to give background towards the defined requirements, and will then be closed with the specific requirements relevant to the aerodynamic design and optimisation of the UAV for maritime surveillance of South Africa's EEZ.

2.1 Mission Profile

To begin with, it is best to mention that the UAV is being designed specifically, and only, for the purpose of Maritime Surveillance of South Africa's EEZ. As such, it can be safely assumed that the UAVs mission profile will most likely consist of ground operations such as taxi and take-off, followed by climbing to cruising altitude, the surveillance, then descent, followed by landing and more ground operations until eventually being shut down. This mission profile is shown in Figure 2-1 below.

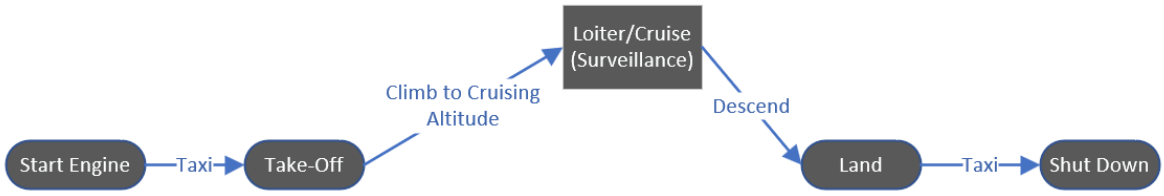

Figure 2-1: Mission Profile for UAV Design

With this mission profile in mind, and since the UAV is being designed for surveillance purposes, it can be assumed that the UAV will spend more than 80% of its flight life under cruise conditions, with the remainder being dedicated to taxi, take-off, climb, descend and land.

2.2 Range and Endurance Considerations

Since the UAV is being designed solely for surveillance of South Africa's EEZ, it can be safely assumed that the UAV will take-off from airfields that are as close to the coast as possible. Figure 2-2 below shows various radii drawn from airfields located close to South Africa's coastline. The radii are each set at just under 500 km and make ample allowance for the 370 km beyond the coastline distance that South Africa's EEZ consists of (Kings, 2016). It can be assumed that the UAVs will require to communicate with ground control station from these airports, and thus the communications distance that the UAV is capable of will need to be 500 km or more. Because the UAV is acting in more of a surveillance role, its flight range is not necessarily of importance, and will be a combination of the UAVs cruising speed, and endurance. Endurance is a much more important parameter for a surveillance UAV than flight range.

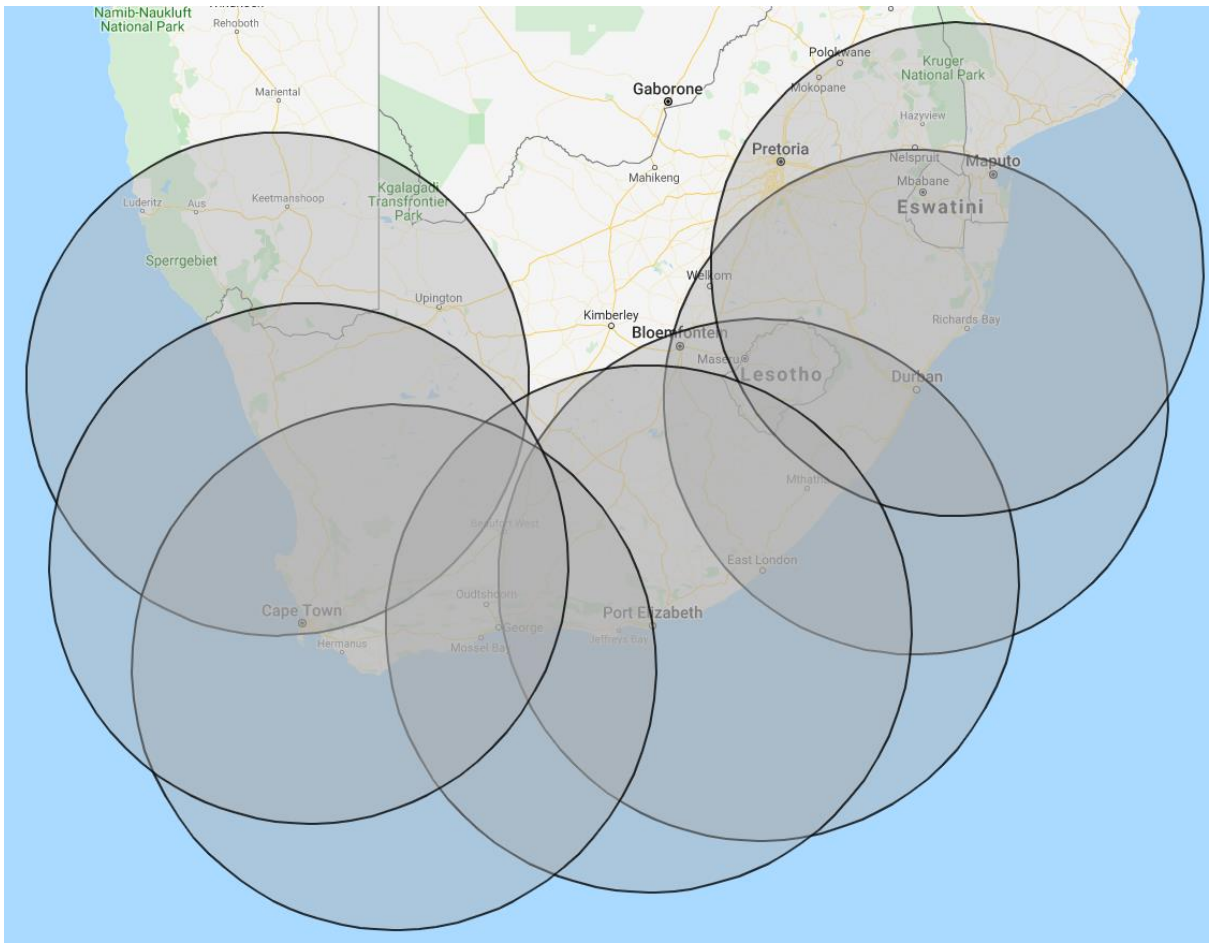

Figure 2-2: 500 km Radii Drawn from Various Coastal Airports Around South Africa

The endurance, or time spent in air, is one of the most important factors for a surveillance UAV. A longer endurance increases time spent loitering and reduces the amount of time between UAV swaps (when one UAV returns to base, and another takes its place for constant surveillance). The goal of the UAV design and optimisation will be to increase the endurance of the aircraft. A minimum, or goal value, will have to be set. A common endurance for current large surveillance UAVs tends to average around 20 hours as seen in section 1.2.3, thus, this is a good starting value for the requirement of the endurance. The endurance will of course, be optimised and extended as far as possible in the later stages of the design.

2.3 Speed and Altitude Considerations

As stated in section 1.1, the area of South Africa's EEZ is approximately 1.5 million square kilometres. This is a large area to properly monitor at a consistent and dependable level. Beyond this, ships, including illegal fishing vessels are generally slow moving, (Digernes & Endal, 1980), with commercial fishing vessels having a maximum speed of approximately 20 knots, or 10.3 m/s. It can be said that it is desired to maximise the cruising speed of the UAV, this will allow the UAV to patrol the required area in a shorter amount of time and will reduce the number of concurrent UAVs busy patrolling the EEZ, while increasing the mission efficiency of each UAV.

Also, if the UAV locates a vessel that is guilty of illegal fishing, the UAV needs to be capable of circling the vessel, while recording video footage of the illegal activities and maintaining a safe and undetectable distance. This will also require a minor amount of speed in order to not only keep up with the vessel but circle it from a large radius while the vessel is in motion as well, further adding to the speed requirements.

All the above points being mentioned, it should still be said, the main goal for the UAV is still not speed, but rather endurance.

In terms of altitude, density decreases with an increase in altitude, and the higher the UAV is required to fly, the more challenging the task becomes, and the larger in size the UAV may become. Reviewing the UAVs provided in the literature review (section 1.2.3), a correlation can clearly be seen between the size of the UAV and the cruising altitude. Medium altitude UAVs are generally classed as being able to fly in the 3000 to 9000m altitude range (Weibel, 2005). The higher in this range the aircraft is required to cruise under general flight conditions, the larger, heavier and more expensive the design becomes (Weibel, 2005). The goal of this UAV design is to keep the UAV as compact and cost effective as possible while still fulfilling its requirements, as such, the altitude requirement will be set at the lower end of this range for cruising flight.

2.4 Clearly Defined Requirements

With the main points to be considered for the requirements discussed in the points above, the final requirements for the UAV are defined in Table 2-1: Defined Requirements of UAV below.

Table 2-1: Defined Requirements of UAV

Requirement	Value	Units
Endurance	>20	hours
Range	>2000	km
Communications Range	>=500	km
Maximum Take-Off Weight	400	kg
Maximum Payload Mass	50	kg
Runway Take-Off Length	1000	m
Stall Speed	25	m/s
Cruising Speed	30 - 50	m/s
Cruising Altitude	~3500	m
Service Ceiling	~6000	m
Absolute Ceiling	~8000	m

CHAPTER 3: Aerodynamics

The engineering branch of aerodynamics mainly concerns the dynamics of gasses and is particularly aimed at the interactions of these gasses with moving objects within an atmosphere (Anderson, 2011). When an object is moving through the air, the fluid moving around it exerts normal pressure forces on the surfaces, as well as tangential shear forces. The combination of these forces induces what is known as lift and drag forces, as well as moments around the body moving through the fluid. With regards to atmospheric flight, these forces and moments are the main concern.

This is of course true with regards to UAV flight, which normally involves complex external flow geometry, with the goal being, for surveillance flight, to maximise the lift forces and reduce the drag forces during balanced, level (cruise) flight. The basics of aerodynamics relevant to the UAV flight will be briefly touched upon.

3.1 Aerodynamic Forces, Moments, and their Coefficients

As previously mentioned, at first glance, where the aerodynamic forces may seem complex due to the complicated flow geometry of objects such as aircraft, the forces and moments acting on the body are due to only two sources, namely, the pressure over the body surfaces, and the shear forces acting along the body surfaces (Anderson, 2011). It is irrelevant how complex the shape is, the only way forces can be translated to a body through a fluid are pressure and shear stress (Anderson, 2011). These pressure and shear forces can be integrated over the body of interest, which results in the resultant force, this force can then be split up into a lift component, a drag component, as well as a resultant moment. The detail and derivation of these integrations are not within the context of this research.

The forces and moments discussed above can be converted into more useful, dimensionless numbers, known as coefficients. These coefficients, which will be frequently referenced in this thesis, are defined as follows as extracted from (Anderson, 2011):

Let the density and velocity of the freestream far ahead of the body of interest be defined as ρ_∞ and V_∞ respectively. Then a dimensional quantity, known as the freestream dynamic pressure, q_∞, can be defined as:

$$q_\infty = \frac{1}{2}\rho_\infty V_\infty^2 \tag{3.1}$$

The units of the dynamic pressure are the same to that of pressure, namely, newtons per square meter, or Pascals. Also, let S be a reference area, and l be a reference length, then the dimensionless coefficients can be defined as below:

Lift Coefficient:

$$C_L = \frac{F_L}{q_\infty S} \tag{3.2}$$

Where C_L is the coefficient of lift, and F_L is the lift force.

Drag Coefficient:

$$C_D = \frac{F_D}{q_\infty S} \tag{3.3}$$

Where C_D is the coefficient of lift, and F_D is the drag force.

Moment Coefficient:

$$C_M = \frac{M_l}{q_\infty S l} \tag{3.4}$$

Where C_M is the moment coefficient, and M_L is the moment force.

In general, in the equations above, the reference area and reference length are chosen according to the type of geometry being looked at. For example, for a UAV, the reference area will generally be the wing planform area, and the reference length may be the Mean Aerodynamic Chord (MAC) of the wing.

3.2 Boundary Layers

When a solid body is moving through a gas such as air, the molecules of air directly in contact with the body have no velocity relative to the surface. In other words, the molecules in contact with the surface, stick to it. This is known in aerodynamics as the no-slip condition (Anderson, 2011). This no-slip condition results in the shear stresses mentioned above, it also results in large velocity gradients near to the surface. The fluid velocity at the surface is zero, and this velocity climbs to the freestream velocity a short distance normal to the surface, resulting in this large velocity gradient. This is known as the boundary layer, and it can have significant effects on the flow fields and forces in aerodynamics.

This boundary layer has a finite (albeit, small) thickness, this thickness increases in the direction of flow (smaller at the front of the body, larger at the rear). The thickness of the boundary layer also depends on the Reynolds number, a dimensionless number that can help characterize the boundary layer. The Reynolds numbers is calculated as equation (3.5) below:

$$R_e = \frac{\rho_\infty V_\infty x}{\mu_\infty} \tag{3.5}$$

Where R_e is the Reynolds number, x is the length to be used for the Reynolds number calculation and μ_∞ is the dynamic viscosity of the freestream.

The boundary layer can have two basic flow states, as defined below:

1. Laminar flow. This is characterized by the flow being stable and smooth, and a single fluid element moves in a smooth motion along streamlines.
2. Turbulent flow. Characterized by unsteady, irregular, chaotic and random movement of flow, in which streamlines break up.

The transition from the laminar to turbulent regime also occurs in a small zone, simply known as the “transition zone”. Transition from laminar to turbulent flow is typically quoted as occurring at a Reynolds number of approximately 500 000 in external aerodynamics applications (Anderson, 2011).

The importance of the resolution of the boundary layer cannot be understated, particularly in a low-speed, surveillance UAV application, where the correct prediction of the laminar, transition, and turbulent zones can result in a noticeable difference in the determination of the lift and drag over the body (Chen, et al., 2020). Particularly with regards to the accurate prediction of the viscous drag, as well as prediction of the separation angle of attack (AOA).

3.3 Separation

Separation is the phenomenon of a flow detaching from the surface of the body which it is flowing over. This detachment of flow results in a substantial increase in the pressure drag on the body, and a substantial drop in lift. Flow separation can also result in a loss of control surface effectiveness, resulting in a loss of control of the UAV, this is not desirable and is to be avoided at all costs. It can go without saying that this is not desired for a surveillance UAV, where the main goal is to do just the opposite, increase lift and decrease drag.

Separation occurs because of an adverse pressure gradient, put in other terms, the pressure increases in the direction of the flow. An adverse pressure gradient is common over the top surfaces of aerofoils, and this is the main area where separation can occur. Cambered, low-speed aerofoils generally consist of an adverse pressure gradient, however, this gradient is not sharp enough at low angles of attack, and separation will only occur at higher angles of attack, depending on the shape of the aerofoil and the flow field.

The boundary layer can play a major role in the location, and severity of flow separation. For example, it has been shown that flow separation occurs later in the flow within a turbulent boundary layer, in comparison to a laminar one. Thus, the resolution and accurate

determination of the boundary layer is of key importance in the flow field calculations of the UAV.

3.4 Key Aerodynamic Design Considerations

There are some key aspects to keep in mind when aerodynamically designing a UAV for surveillance purposes. These aspects can make a significant difference to the aerodynamic forces during flight, and a good baseline with these parameters can be key to designing an aerodynamically efficient UAV. These aspects are briefly touched on in this chapter.

3.4.1 Aspect Ratio

Possibly one of the most important factors for a surveillance UAV, is the wings aspect ratio, AR, which is defined in equation (3.6) below:

$$AR = \frac{b^2}{S} \tag{3.6}$$

Where b is the wingspan, and S is the wing planform area.

In other words, the aspect ratio of a wing is defined as its span squared, divided by its planform area. The aspect ratio of a wing plays a major role in the wings induced drag, which is the drag on a 3D, finite wing as a resultant of the lift distribution over the wing, it is defined mathematically as below:

$$C_{D,i} = \frac{C_L^2}{\pi e AR} \tag{3.7}$$

Where $C_{D,i}$ is the induced drag coefficient and e is the span efficiency factor.

From equation (3.7) above, the induced drag is inversely proportional to the aspect ratio, which means that for constant lift and span efficiency, the higher the aspect ratio of the wing, the less induced drag.

Of course, in theory, it would be preferable to have an infinite aspect ratio. This is of course, not practical, and thus the aspect ratio must be increased as much as possible for a long endurance surveillance UAV. The trade-off is that the higher the aspect ratio, the heavier, and more difficult it will be to design the structural aspects of the wing; thus, the aspect ratio has to be kept within reasonable limits.

3.4.2 Taper Ratio

The taper ratio of the wing, defined as per equation (3.8) below, also plays a role in the induced drag of the wing.

$$\lambda_{TR} = \frac{c_t}{c_r} \tag{3.8}$$

Where λ is the taper ratio, c_t is the tip chord of the wing, and c_r is the root chord.

The taper ratio influences the span efficiency factor of the wing in equation (3.7) above. It has been experimentally shown that a taper ratio between 0.2 and 0.4, yields the maximum span efficiency, and thus the lowest induced drag (Anderson, 2011).

3.4.3 Fuselage Length and Diameter

The main function of the fuselage is, of course, to house the various payloads, electronics, landing gear, engine, and fuel of the UAV. Thus, the fuselage can require a significant volume. The fuselage is not necessarily designed to contribute to the lift of a UAV in general as well (this is not the case for a blended body UAV). Thus, the main aerodynamic concern of the fuselage, is to provide enough volume to house all the required items, and to do so, with as little drag as possible.

Since most of the surveillance UAVs flight will be spent in cruising flight, with the fuselage generating little to no lift, the goal will be to reduce the fuselage drag under no lift.

(Sadraey, 2013, pp. 372-373) mathematically derives a length to diameter ratio for a fuselage that results in the minimum drag during cruising flight. This ratio was found to be 16.3, and this is the value that should be aimed for in the fuselage design.

3.5 Governing Equations

Fluid flow can be described by a set of governing equations, which can be expressed in various forms and co-ordinate systems. For the purposes of this research, the governing equations will be presented in the Partial Differential Equation (PDE) form, using Cartesian (*x*, *y*, *z*) co-ordinate system. This is one of the more common forms to express the governing equations of fluid flow. It should also be noted that, where applicable, the equations are given using the Eulerian approach, namely, the approach for viewing the fluid as passing through a fixed volume in space, instead of the Lagrangian approach, where a fluid particle is followed on its path through space (Versteeg & Malalasekera, 2007).

The conservation laws of physics are used to derive the equations, the laws used are stated below (Versteeg & Malalasekera, 2007):

- Mass cannot be created nor destroyed, and the mass of fluid is conserved.
- The sum of forces on a fluid particle equals the rate of change of momentum, this is Newton's second law.
- The rate of work done on a fluid particle and the rate of heat addition to the fluid particle is equal to the rate of change of energy, this is the first law of thermodynamics.

With these laws in mind, the governing equations of fluid flow can be written as below. The derivations of these equations will not be covered, and only the final version will be stated.

3.5.1 Continuity Equation

The continuity equation, also known as the three-dimensional, unsteady mass conservation equation, is the mathematical equation derived from the statement that the mass of fluid is conserved. It is derived in (Versteeg & Malalasekera, 2007, pp. 10-11), and the final form is shown below.

$$\frac{\partial \rho}{\partial t} + \frac{\partial (\rho u)}{\partial x} + \frac{\partial (\rho v)}{\partial y} + \frac{\partial (\rho w)}{\partial z} = 0 \tag{3.9}$$

A more compact form of the equation can be given as per below, using vector notation.

$$\frac{\partial \rho}{\partial t} + \mathrm{div}(\rho \boldsymbol{u}) = 0 \tag{3.10}$$

It should be stated that the equations above are for a compressible fluid, if required, the continuity equation can also be simplified to equation (3.11) below. This simplification comes about from the fact that the density can be set to be constant in incompressible flow.

$$\frac{\partial u}{\partial x} + \frac{\partial v}{\partial y} + \frac{\partial w}{\partial z} = 0 \tag{3.11}$$

3.5.2 Momentum Equation

The rate of change of momentum on a fluid particle is equal to the sum of the forces on said particle. This is known as Newton's second law. The mathematical representation of this law, for a fluid particle, is shown in equations (3.12), (3.13) and (3.14) below, its derivation is provided in (Versteeg & Malalasekera, 2007, pp. 14-16). The reason there are three equations to represent the momentum, is that each equation is given showing momentum in a different direction. Equation (3.12) shows the x-direction, (3.13) the y-direction and (3.14) the z-direction respectively in conservative form.

$$\frac{\partial (\rho u)}{\partial t} + \mathrm{div}(\rho u \boldsymbol{u}) = -\frac{\partial p}{\partial x} + \mathrm{div}(\mu \, \nabla u) + S_{Mx} \tag{3.12}$$

$$\frac{\partial (\rho v)}{\partial t} + \mathrm{div}(\rho v \boldsymbol{u}) = -\frac{\partial p}{\partial y} + \mathrm{div}(\mu \, \nabla v) + S_{My} \tag{3.13}$$

$$\frac{\partial (\rho w)}{\partial t} + \mathrm{div}(\rho w \boldsymbol{u}) = -\frac{\partial p}{\partial z} + \mathrm{div}(\mu \, \nabla w) + S_{Mz} \tag{3.14}$$

The S_M terms in the equations represent source terms, which include the contributions due to body forces, for example, gravity.

3.5.3 Energy Equation

As stated earlier, the first law of thermodynamics states that the rate of work done on a fluid particle and the rate of heat addition to the fluid particle is equal to the rate of change of energy. Another common way of stating this law is by saying that energy cannot be created or destroyed in a system. Equation (3.15) below gives a mathematical representation in the conservative form of this law with regards to fluid mechanics. Again, the derivation is provided in (Versteeg & Malalasekera, 2007, pp. 16-20).

$$\frac{\partial(\rho i)}{\partial t} + \operatorname{div}(\rho i \boldsymbol{u}) = -p \operatorname{div} \boldsymbol{u} + \operatorname{div}(k \nabla T) + \boldsymbol{\Phi} + S_i \tag{3.15}$$

CHAPTER 4: Computational Fluid Dynamics

Where analytical calculations and methods can provide a particularly good first order guess to simple aerodynamic calculations, and can be quite accurate at times, they can also frequently miss details to individual geometry and designs, and their accuracy tends to degrade with increasingly complex, three-dimensional geometry and flows. Also, analytical methods are normally only applicable to a certain set of well-defined and researched problems. Industrial problems on the other hand, can be more complex and frequently not as well defined, requiring CFD to be solved in an efficient and accurate manner.

There are three main types of numerical solution techniques in CFD, namely, finite difference, finite element, and spectral methods (Versteeg & Malalasekera, 2007). The focus of this thesis shall be on the Finite Volume Method (FVM), a special finite difference formulation that is used by the CFD software package employed for this research, namely, Ansys FLUENT (ANSYS INC, 2018), this formulation is also the formulation used by the most established CFD solvers (Versteeg & Malalasekera, 2007). This chapter will briefly discuss the information relevant to the CFD modelling required for this research.

4.1 Navier-Stokes Equations

The equations covered in section 3.5, namely, the governing equations, contain unknowns in the form of the viscous stress components τ_{ij} (Versteeg & Malalasekera, 2007). Thus, suitable models need to be included to account for the unknowns in the viscous stresses. In most fluid flows of interest, the viscous stresses can be expressed as functions of the rate of strain, or rate of local deformation. For a three-dimensional flow, this rate comprises of the linear deformation rate, as well as the volumetric deformation rate. With the assumption that the fluid of interest is isotropic, and without going into too much detail of the derivation of the Navier-Stokes equations, the most useful form, as derived in (Versteeg & Malalasekera, 2007), is provided below in equations (4.1), (4.2) and (4.3), for the x, y and z directions respectively. These equations are the incompressible flow Navier-Stokes equations, and the divergence free condition has already been incorporated.

$$\rho \frac{Du}{Dt} = -\frac{\partial p}{\partial x} + \mathrm{div}(\mu \nabla u) + S_{Mx} \tag{4.1}$$

$$\rho \frac{Dv}{Dt} = -\frac{\partial p}{\partial y} + \mathrm{div}(\mu \nabla v) + S_{My} \tag{4.2}$$

$$\rho \frac{Dw}{Dt} = -\frac{\partial p}{\partial z} + \mathrm{div}(\mu \nabla w) + S_{Mz} \tag{4.3}$$

4.2 Transport Equation

It can be seen from **Error! Reference source not found.** that the governing equations have similarities between them, advantage can be made of this fact, and a universal equation for a general variable property ϕ, known as the transport equation, can be written as equation (4.4) below (Versteeg & Malalasekera, 2007). Where ϕ represents a general variable.

$$\frac{\partial(\rho\phi)}{\partial t} + \mathrm{div}(\rho\phi\boldsymbol{u}) = \mathrm{div}(\Gamma\,\nabla\phi) + S_\phi \tag{4.4}$$

Equation (4.4) above, is the differential form of the transport equation, and is a useful starting point for the computation of the FVM. It is worth noting that this equation takes a form to bring out the commonalities in the governing equations, and that any differences between the equations, are included in the source term, S_ϕ, of the transport equation.

Integration of the transport equation over a three-dimensional control volume (CV), is the key to the Finite Volume Method. Without going through the derivation of the integration of this equation, the final, integrated form of the transport equation is shown in equation (4.5) below (Versteeg & Malalasekera, 2007). This equation represents the time-dependent version of the equation.

$$\begin{aligned} &\int_{\Delta t}\frac{\partial}{\partial t}\left(\int_{CV}\rho\phi\,\mathrm{d}V\right)\mathrm{d}t \\ &+\int_{\Delta t}\int_{A}\mathbf{n}\,.\,(\rho\phi\mathbf{u})\mathrm{d}A\mathrm{d}t \\ &=\int_{\Delta t}\int_{A}\mathbf{n}\,.\,(\Gamma\,\nabla\phi)\mathrm{d}A\mathrm{d}t+\int_{\Delta t}\int_{CV}S_\phi\mathrm{d}\mathrm{V}\mathrm{d}t \end{aligned} \tag{4.5}$$

This integrated version of the transport equation is used to build the numerical methods for the finite volume (also known as control volume) method (Versteeg & Malalasekera, 2007).

4.3 Reynolds-Averaged Navier-Stokes

Turbulent flows, such as that involved in external aerodynamics of a MALE UAV, are inherently unsteady flows, as turbulence is a random and chaotic phenomenon. This can pose a problem for so called “steady state” flow calculations, as such, the Reynolds-averaged Navier-Stokes equations were developed, decomposing the instantaneous continuity and momentum equations into the mean and fluctuating values, thereby allowing a turbulent flow to be “time-averaged”. The Reynolds-Averaged form of the Navier-Stokes equations are provided below, this is the compressible flow form of the equations, along with this, the scalar transport equation is also provided (Versteeg & Malalasekera, 2007).

In the equations below, the symbol $\widetilde{U}$ stands for the Favre-averaged velocity, the overbar indicates a variable that is time-averaged, and the tilde shows a density-weighted (Favre-averaged) variable.

Continuity:

$$\frac{\partial \bar{\rho}}{\partial t} + \operatorname{div}\left(\bar{\rho}\widetilde{\boldsymbol{U}}\right) = 0 \tag{4.6}$$

Reynolds Equations:

$$\begin{aligned} &\frac{\partial(\bar{\rho}\widetilde{U})}{\partial t} + \operatorname{div}\left(\bar{\rho}\widetilde{U}\widetilde{\boldsymbol{U}}\right) \\ &= -\frac{\partial \bar{P}}{\partial x} + \operatorname{div}\left(\mu\,\nabla\widetilde{U}\right) + \left[-\frac{\partial(\overline{\bar{\rho}u'^2})}{\partial x} - \frac{\partial(\overline{\bar{\rho}u'v'})}{\partial y} - \frac{\partial(\overline{\bar{\rho}u'w'})}{\partial z}\right] \\ &+ S_{Mx} \end{aligned} \tag{4.7}$$

$$\begin{aligned} &\frac{\partial(\bar{\rho}\widetilde{V})}{\partial t} + \operatorname{div}\left(\bar{\rho}\widetilde{V}\widetilde{\boldsymbol{U}}\right) \\ &= -\frac{\partial \bar{P}}{\partial y} + \operatorname{div}\left(\mu\,\nabla\widetilde{V}\right) + \left[-\frac{\partial(\overline{\bar{\rho}u'v'})}{\partial x} - \frac{\partial(\overline{\bar{\rho}v'^2})}{\partial y} - \frac{\partial(\overline{\bar{\rho}v'w'})}{\partial z}\right] \\ &+ S_{My} \end{aligned} \tag{4.8}$$

$$\begin{aligned} &\frac{\partial(\bar{\rho}\widetilde{W})}{\partial t} + \operatorname{div}\left(\bar{\rho}\widetilde{W}\widetilde{\boldsymbol{U}}\right) \\ &= -\frac{\partial \bar{P}}{\partial z} + \operatorname{div}\left(\mu\,\nabla\widetilde{W}\right) \\ &+ \left[-\frac{\partial(\overline{\bar{\rho}u'w'})}{\partial x} - \frac{\partial(\overline{\bar{\rho}v'w'})}{\partial y} - \frac{\partial(\overline{\bar{\rho}w'^2})}{\partial z}\right] + S_{Mx} \end{aligned} \tag{4.9}$$

Scalar Transport Equation:

$$\begin{aligned} &\frac{\partial(\bar{\rho}\widetilde{\Phi})}{\partial t} + \operatorname{div}\left(\bar{\rho}\widetilde{\Phi}\widetilde{\boldsymbol{U}}\right) \\ &= \operatorname{div}\left(\Gamma_{\Phi}\,\nabla\widetilde{\Phi}\right) + \left[-\frac{\partial(\overline{\bar{\rho}u'\varphi'})}{\partial x} - \frac{\partial(\overline{\bar{\rho}v'\varphi'})}{\partial y} - \frac{\partial(\overline{\bar{\rho}w'\varphi'})}{\partial z}\right] + S_{\Phi} \end{aligned} \tag{4.10}$$

4.4 Turbulence Modelling

The Reynolds-Averaged equations above (equations (4.6) to (4.9)), represent time averaged equations for steady flows. Extra terms become apparent in these time averaged equations because of the fluctuations and interactions of various values due to turbulence. These extra terms can be modelled using what is known as “turbulence models”, which are used to predict the Reynolds stresses, as well as the scalar transport terms and thus, close the Reynolds-Averaged equations (Versteeg & Malalasekera, 2007).

There are many different turbulence models available, some of which work better under certain conditions, or are more accurate for certain types of flows, than others. This section will focus on the most common turbulence models used for external aerodynamics applications, namely, the Spalart-Allmaras model, and the Menter Shear Stress Transport (SST) $k-\omega$ model (Versteeg & Malalasekera, 2007). These models have proven to be reliable, and accurate, if used correctly, for external aerodynamics applications.

4.4.1 Spalart-Allmaras one-equation model

The Spalart-Allmaras model is a popular model for external aerodynamics applications, it solves one equation involving the kinematic eddy viscosity, this makes it an efficient model, particularly for large problems (such as that of computing boundary layers for external aerodynamics) (Versteeg & Malalasekera, 2007). It should be noted that the Spalart-Allmaras model assumes the entire boundary layer to be turbulent and does not factor transition from laminar to turbulent flow into its calculation. The mathematical representation for the Spalart-Allmaras model is given below, as provided in (Versteeg & Malalasekera, 2007).

$$\begin{aligned}&\frac{\partial(\rho\tilde{\nu})}{\partial t}+\operatorname{div}(\rho\tilde{\nu}\boldsymbol{U})\\&=\frac{1}{\sigma_{\nu}}\operatorname{div}\left[(\mu+\rho\tilde{\nu})\nabla(\tilde{\nu})+C_{b2}\rho\frac{\partial\tilde{\nu}}{\partial x_k}\frac{\partial\tilde{\nu}}{\partial x_k}\right]+C_{b1}\rho\tilde{\nu}\tilde{\Omega}\\&-C_{w1}\rho\left(\frac{\tilde{\nu}}{\kappa y}\right)^2 f_w\end{aligned}\qquad(4.11)$$

Equation (4.11) above represents the transport equation for the kinematic eddy viscosity $\tilde{\nu}$, other important equations to note, relating to the equation (4.11) above and the Spalart-Allmaras model are below.

The dynamic eddy viscosity is related to the kinematic eddy viscosity as equation (4.12) below.

$$\mu_t=\rho\tilde{\nu}f_{\nu 1}\qquad(4.12)$$

Where $f_{\nu 1}$ is a wall damping function and is equal to $f_{\nu 1}\left(\frac{\tilde{\nu}}{\nu}\right)$.

The Reynolds stresses are computed as equation below (4.13).

$$\tau_{ij} = 2\mu_t S_{ij} = \rho f_{v1}\left(\frac{\partial U_i}{\partial x_j} + \frac{\partial U_j}{\partial x_i}\right) \quad (4.13)$$

The local mean vorticity and the rate of production of the dynamic eddy viscosity is related in equation (4.14) below.

$$\widetilde{\Omega} = \Omega + \frac{\tilde{v}}{(\kappa y)^2} f_{v2} \quad (4.14)$$

Where $\Omega = \sqrt{2\Omega_{ij}\Omega_{ij}}$ which represents the mean vorticity and $\Omega_{ij} = \frac{1}{2}\left(\frac{\partial U_i}{\partial x_j} - \frac{\partial U_j}{\partial x_i}\right)$, which represents the mean vorticity tensor.

Furthermore, the two functions $f_{v2} = f_{v2}\left(\frac{\tilde{v}}{v}\right)$ and $f_w = f_w\left(\frac{\tilde{v}}{\widetilde{\Omega}\kappa^2 y^2}\right)$ represent further wall-damping functions.

It can also be noticed that the equations contain constants, these constants can be tuned to be suitable for external aerodynamic flows, which results in the constants given in Table 4-1 below (Versteeg & Malalasekera, 2007). There are three more constants provided that are not shown in the table below, these are hidden in the wall functions. These constants have been proven to give accurate results in boundary layers that involve adverse pressure gradients (Versteeg & Malalasekera, 2007).

Table 4-1: Spalart-Allmaras model constants

σ_v	$\frac{2}{3}$
κ	0.4187
C_{b1}	0.1355
C_{b2}	0.622
C_{w1}	$C_{b1} + \kappa^2 \frac{1 + C_{b2}}{\sigma_v}$

4.4.2 Menter SST $k - \omega$ model

Before covering the detail of the Menter SST model, two other models need to be mentioned, namely, the Wilcox $k - \omega$ model, and the $k - \varepsilon$ model.

The latter of these two models is widely used for general purpose CFD solutions, however, in the presence of adverse pressure gradients, it calculates excessive levels of turbulent shear

stress, furthermore, it calculates massive levels of turbulence in stagnation regions, resulting in excessively high levels of heat transfer in reattachment regions of flow (Versteeg & Malalasekera, 2007). This model needs to be mentioned, as the Menter SST model is a hybrid turbulence model, using the $k-\varepsilon$ model in the fully turbulent regions far from the wall.

The Wilcox $k-\omega$ model is mentioned because this is the model that is used in the near-wall region. The Menter SST $k-\omega$ model involves the transformation of the ε equation, into that of a ω equation, by substitution of $\varepsilon = k\omega$. Further detail of both the Wilcox $k-\omega$, and the $k-\varepsilon$ models, can be found in most CFD literature, and will not be discussed in further detail here. What will be mentioned however, is the substituted equation that results from the substitution of $\varepsilon = k\omega$ above, this results in equation (4.15) below (Versteeg & Malalasekera, 2007).

$$\begin{aligned} &\frac{\partial(\rho\omega)}{\partial t} + \operatorname{div}(\rho\omega \boldsymbol{U}) \\ &= \operatorname{div}\left[\left(\mu + \frac{\mu_t}{\sigma_{\omega,1}}\right)\nabla(\omega)\right] + \gamma_2\left(2\rho S_{ij}\,.\,S_{ij} - \frac{2}{3}\rho\omega\frac{\partial U_i}{\partial x_j}\delta_{ij}\right) \\ &- \beta_2\rho\omega^2 + 2\frac{\rho}{\sigma_{\omega,2}\omega}\frac{\partial k}{\partial x_k}\frac{\partial \omega}{\partial x_k} \end{aligned} \qquad (4.15)$$

The constants for this model, which have been revised from the Wilcox $k-\omega$ model, are provided below in Table 4-2.

Table 4-2: Menter SST Model Constants

σ_k	1.0
$\sigma_{\omega,1}$	2.0
$\sigma_{\omega,2}$	1.17
γ_2	0.44
β_2	0.083
β^*	0.09

Beyond this, blending functions were also introduced to handle numerical instabilities that result from the differences between the computed values of the eddy viscosity between the standard $k-\varepsilon$ model in the far field, and the transformed $k-\varepsilon$ model near the wall. These blending functions result in a smooth transition between the two models (Versteeg & Malalasekera, 2007). These blending functions replace the model constants C_1 in the original $k-\omega$ model, and the value C_2 in the Menter transformed $k-\varepsilon$ model as equation (4.16) below.

$$C = F_C C_1 + (1 - F_C) C_2 \tag{4.16}$$

Limits are also added to the eddy viscosity and the production of the turbulent kinetic energy, the function of these limits are to improve the performance in wake regions and flows with adverse pressure gradients for the eddy viscosity, and to prevent the overprediction of the turbulence in stagnation regions for the turbulent kinetic energy. The limiters are given below in equations (4.17) and (4.18).

$$\mu_t = \frac{a_1 \rho k}{\max(a_1 \omega, S F_2)} \tag{4.17}$$

Where $S = \sqrt{2 S_{ij} S_{ij}}$, a_1 is a constant and F_2 is a blending function.

$$P_k = \min\left(10\beta^* \rho k\omega, 2\mu_t S_{ij} . S_{ij} - \frac{2}{3}\rho k \frac{\partial U_i}{\partial x_j}\delta_{ij}\right) \tag{4.18}$$

4.4.3 Transition SST model

In low speed, medium altitude flows, such as that involved with a sail plane or a surveillance UAV, the portion of the flow that is laminar may have significant effects on the flow field, as shown by other studies such as (Chen, et al., 2020) and (Swart, 2020). This is particularly true with regards to the calculation of the drag due to skin friction, and flow separation. Thus, information on the Transition SST model, which takes the transition point from laminar to turbulent flow into account, will also be included. This model is also known as the $\gamma - Re_\theta$ model (ANSYS INC, 2018).

This model involves two extra transport equations, one of which involves the transition onset criteria in terms of the momentum-thickness Reynolds number, and the other the intermittency, and couples them with the SST $\mathrm{k} - \omega$ model transport equation (ANSYS INC, 2018).

The two extra transport equations involved in the transition SST model are provided below, as given in (ANSYS INC, 2018). It should be noted that there is much more detail to these equations for the constants, correlations and sources (such as the destruction and relaminarization sources), that are included in (ANSYS INC, 2018), and the detail of these is out of the scope of this brief discussion on the transition model.

The intermittency γ transport equation is given in equation (4.19) below.

$$\frac{\partial(\rho\gamma)}{\partial t} + \frac{\partial(\rho U_j \gamma)}{\partial x_j} = P_{\gamma 1} - E_{\gamma 1} + P_{\gamma 2} - E_{\gamma 2} + \frac{\partial}{\partial x_j}\left[\left(\mu + \frac{\mu_t}{\sigma_\gamma}\right)\frac{\partial \gamma}{\partial x_j}\right] \tag{4.19}$$

The transport equation of the transition momentum thickness Reynolds number $R\tilde{e}_{\theta t}$ is provided in equation (4.20) below.

$$\frac{\partial(\rho R\tilde{e}_{\theta t})}{\partial t}+\frac{\partial(\rho U_j R\tilde{e}_{\theta t})}{\partial x_j}=P_{\theta t}+\frac{\partial}{\partial x_j}\left[\sigma_{\theta t}\left(\mu+\frac{\mu_t}{\sigma_y}\right)\frac{\partial R\tilde{e}_{\theta t}}{\partial x_j}\right] \tag{4.20}$$

4.5 Resolution of the Boundary Layer

Of particular importance with regards to RANS turbulence modelling of external aerodynamic flows, is the correct resolution of the turbulence in the boundary layer. The gradients are often largest near the wall and in the boundary layer, and thus, the solution can be sensitive to correct resolution of the boundary layer (ANSYS INC, 2018).

There are two approaches to modelling the turbulence near a wall in CFD, namely, using wall functions, or using the Near-Wall model. The difference being that the near-wall approach requires a finer grid than a wall function near the wall in order to fully resolve the boundary layer. The wall function approach on the other hand uses semi-empirical formulas in order to mathematically model the turbulent boundary layer (ANSYS INC, 2018), it is worth noting again that the wall function approach does not require as fine a grid near the wall as a near-wall approach.

For external aerodynamics applications, it is generally recommended that the near-wall treatment be used, as the solution can be significantly affected by the correct resolution of the boundary layer, as seen in the literature covered in section 1.2.2. Thus, the near-wall approach will be the focus of this paper.

The near-wall approach has requirements for the grid generation of the CFD simulation, particularly in the case of the Transition SST model. The main requirement in order to correctly resolve the boundary layer, is that of the y^+, which should preferably be less than 1, and not more than 8 (ANSYS INC, 2018). The formula for y^+ is given below in equation (4.21).

$$y^+=\frac{\rho u_\tau y}{\mu} \tag{4.21}$$

Where u_τ is defined as the skin friction velocity, or $\sqrt{\frac{\tau_w}{\rho}}$. And y is the height of the first cell normal to the wall. Therefore, for a particular solution, the main requirement of the grid is that the height of the first cells normal to the wall be lower than a particular value in order ensure a suitable y^+ value that does not degrade solution accuracy.

CHAPTER 5: Initial Design Layout and Modelling

5.1 Initial UAV sizing

The first step in the design of the surveillance UAV was determining an estimate of its overall size and mass. Several, well documented tools exist for the size and mass estimation of more commercial aircraft, such as fighter jets, cargo aircraft, and commercial airliners. However, finding a tool for the initial size and mass estimations of a UAV was more challenging. An interesting concept for the rough initial size estimates, as well as weight estimates of all the different systems, was found in (Bernard Micro Systems, n.d.). This website uses the data of existing UAVs (in a particular engine category) and finds mathematical relations of the size and weight of the existing UAVs. These formulas can then be used to estimate the size and weight of any UAV (of similar engine system) by inputting the required payload mass, the required range, endurance, and by using a constant empirical parameter for the fuel mass. The UAVs used to determine these formulas are of similar engine system and purpose to the surveillance UAV that is required to be designed and is therefore deemed a suitable model to estimate the initial size and mass of the UAV to be designed. More detail can be found in (Bernard Micro Systems, n.d.), and the author used this website and its formulas to write a small Python script for the initial calculations, which is included in APPENDIX A.1.

These calculations worked well for a rough initial estimation; however, a slightly more detailed calculation procedure is required to obtain a better estimate of more performance parameters, including take-off run, cruise ceiling, wing area and engine power requirements. For a more detailed investigation into these extra parameters and their effect on performance, size and mass, the procedure laid out in (Sadraey, 2013, pp. 94-145) was used. Again, a Python script was written to quickly iterate and visualise these equations, the script is included in APPENDIX A.2, along with the parameters used for the final iteration of the calculation. The assumptions made, as well as the final calculated values, include a few factors of safety, as these calculations and their values are only estimating at this stage in the process. The output of the Python script produces a graph, Figure 5-1 below, that calculates and plots the wing and power loading required to meet the requirements of the UAV, the red zones indicate wing/power loading values where the UAV will not meet its requirements, thus, a point needs to be selected where the wing and power loading are maximum, but still able to meet the requirements (in the white zone), this point is indicated by the blue dot on the graph, with a small safety factor of 5% included.

The quantitative results from these calculations are included in Table 5-1 below.

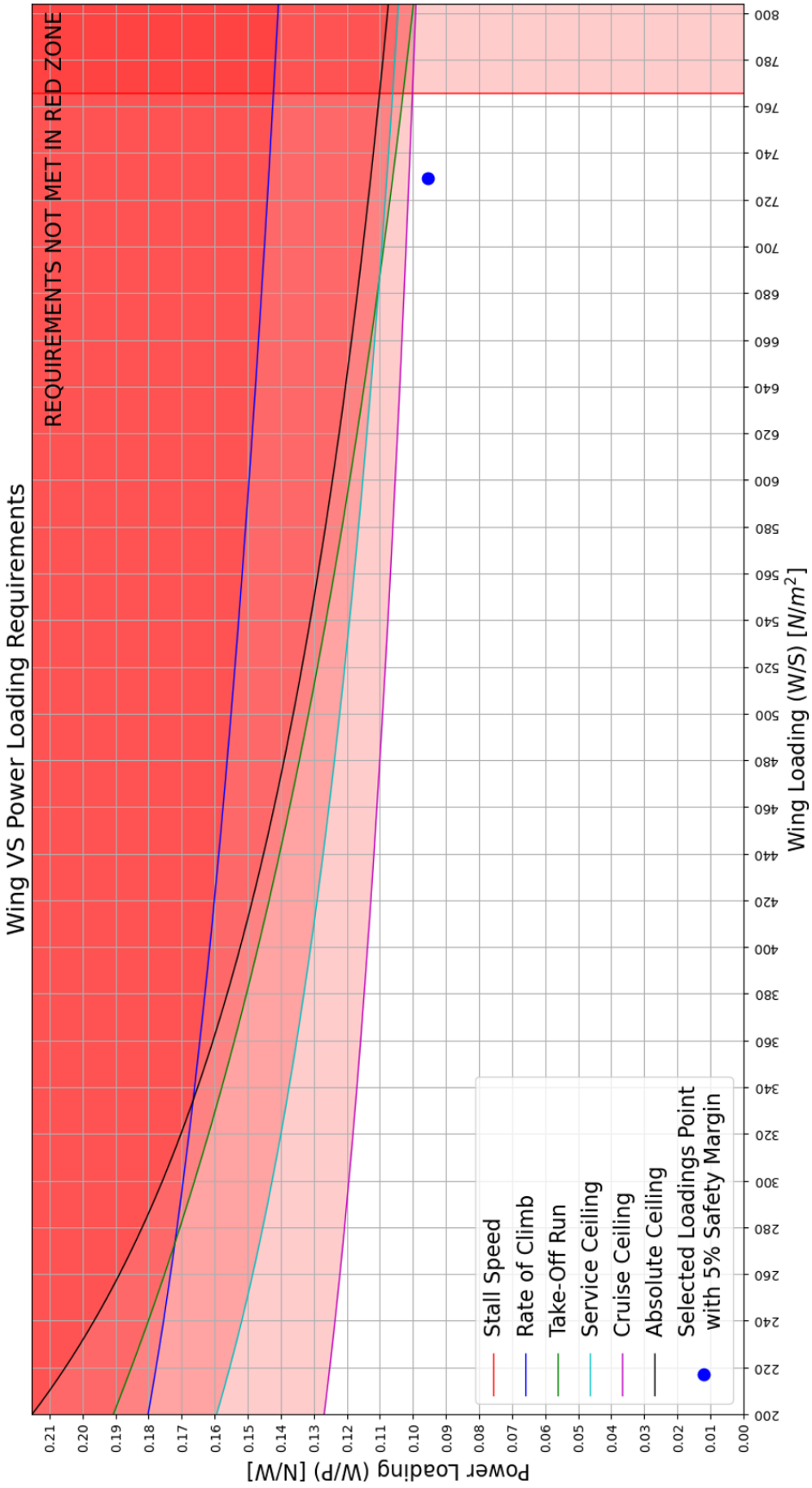

Figure 5-1 Graph Produced from Sizing Calculation Python Script

Table 5-1: Resultant Wing Area and Engine Power from Sizing Calculations

Parameter	Value	Units
Wing Loading	729.17	N/m^2
Power Loading	0.1	N/W
Required Wing Area	5.38149	m^2
Required Engine Power	41.14	kW

The parameters in Table 5-1 above were used for the engine selection, and wing sizing of the initial UAV design.

5.2 Payloads and Systems Selection

In an ideal world, the fuselage of a surveillance UAV would be as thin as a drinking straw (and weigh the same too), and still be able to perform its mission. Unfortunately, the UAV must be capable of carrying several types of systems and payloads, to guide and control the aircraft, provide communications, and help perform its mission. The aircraft must also carry sufficient fuel for its mission, store landing gear (if retractable gear is selected) and provide space for an engine and its systems to provide power.

Where the specific selection of payloads and systems is not part of the scope of this research, current sizes and masses of relevant systems need to be researched and defined in order to more accurately determine the size (internal volume), mass, and Centre of Gravity (COG) position of the UAV. The CAD model of the UAV includes several systems and payloads, that help the UAV perform its mission, and meet the requirements of the UAV, this includes the engine, communication and control equipment, and payloads. The system, and its volume and mass are given in Table 5-2 below. This table is by no means an extensive list of all the systems required by a UAV, but it does cover most of the main systems, extra volume within the UAV will be provided in order to fit more systems and allow for better/more precise fitment of all the systems. The volumes and masses are obtained from datasheets of systems currently available for purchase from aerospace and avionics companies (besides the fuel tank and landing gear, which will have to be designed). Where possible, the systems were selected with the UAV application and requirements in mind, for example, the engine used as an example engine can meet the power requirements determined above in Table 5-1. These systems were all selected as a baseline for the UAV fuselage design.

Table 5-2: Volumes and Masses of Theoretical Systems and Payloads

System	Volume [mm x mm x mm UOS]	Mass [kg]	Source
Engine	324 x 310 x 243	21.2	(Rotron Power Ltd., 2020)
Starter and Alternator	Fits in engine envelope	3.2	(Rotron Power Ltd., 2020)
Water Pump	50 x 50 x 100	0.25	(Rotron Power Ltd., 2020)
Radiator	100 x 260 x 32	1.15	(Rotron Power Ltd., 2020)
Oil Tank	5L	5.5 (including oil)	(Rotron Power Ltd., 2020)
Engine ECU	250 x 110 x 117	0.4	(Northwest UAV, 2019)
Reduction Drive	Fits in engine envelope	2.7	(Rotron Power Ltd., 2020)
Throttle Body	Fits in engine envelope	0.3	(Rotron Power Ltd., 2020)
Exhaust	120 x 120 x 250	2	(Rotron Power Ltd., 2020)
Camera Gimbal	140 x 140 x 189	2	(Octopus ISR Systems, n.d.)
SATCOM Unit	290 x 290 x 210	3.2	(GetSAT, 2019)
Radar System (SAR)	260 x 230 x 185	2.7	(IMSAR, 2017)
Fuel Delivery System	180 x 110 x 70	0.8	(Northwest UAV, 2019)
Battery Backup Module	140 x 210 x 100	1.7	(Northwest UAV, 2019)
Generator Control Unit (GCU)	135 x 125 x 51	1.0	(Northwest UAV, 2019)
Transponder	91 x 57 x 17	0.1	(Northwest UAV, 2019)
Autopilot	117 x 70 x 82	0.7	(Northwest UAV, 2019)
Fuel	150L	128 (including fuel tank)	Designed assumption
Front Landing Gear	1200 x 40 x 150	4.0	Designed assumption
Rear Landing Gear	1200 x 100 x 150	8.0	Designed assumption

5.3 Aerodynamic Configuration and Design

The configuration selection and design of the various key aerodynamic areas will be discussed here. The design methodology and information from (Sadraey, 2013) was used for the configuration selection of the various sub-systems, and a mix of information from (Anderson, 1989), (Anderson, 2011) and (Sadraey, 2013) was used for the information regarding the aerodynamics.

For the initial design steps and calculations, xflr5, a wing design and analysis program which uses Lifting Line Theory, Vortex Panel Method and 3D Panel Method was used (xflr5, 2019). The advantages of xflr5 being that one can quickly iterate between designs and changes and view accurate lift, drag and moment results of wing and tail designs, or a combination of both wing and tail, including the effects of downwash, at low Reynolds Numbers. Different designs can be quickly made and compared, allowing for a lot of insight and information, and the best starting point for a detailed CAD design, to be obtained quickly, easily and accurately. The

disadvantages and shortcomings of xflr5 include but are not limited to the following (Depperois, 2019).

- The mathematical models of xflr5 are only valid in conditions with no, or limited, flow separation.
- The Vortex Lattice Method (VLM) does not calculate viscous drag, it merely interpolates it from 2D results at a local wing section. This can result in an underestimation of the drag coefficient, as well as a completely incorrect transition location from laminar to turbulent flow, as crossflow effects are not included in the calculation.
- When running calculations in xflr5 which include the fuselage of the aircraft, the panels at the wing/body junction are mismatched. The consequence of this is that the interaction of the wing and body flows cannot be accurately modelled.
- The wake in xflr5 is modelled flat, instead of as vortices and streamlines. This results in an over-estimation of the vortex strengths and consequently, of the lift and induced drag.

Even with the drawbacks mentioned above, xflr5 is still a useful tool for the initial design stages, and a good first guess design can be produced using xflr5. The drawbacks have to be kept in mind, and for a program of such cost and complexity as what a surveillance UAV can be, xflr5 calculations alone should never be trusted.

5.3.1 Wing

Possibly the most critical design area of a surveillance UAV, and many aircraft, is that of the wing. The main goal of the wing design for a surveillance UAV, is to provide the required lift, while reducing drag as far as possible. It is also advantageous to design a wing with as light a structure as possible, while still meeting the structural requirements. Several key decisions need to be made with regards to the wing design parameters. These decisions are briefly discussed below in sections 5.3.1.1 to 5.3.1.3, the decisions are then tabulated in Table 5-3.

5.3.1.1 Number of Wings and Wing Vertical location on Fuselage

Olden day aircraft, due to manufacturing and structural limitations, frequently employed more than one wing (Sadraey, 2013). With the advances made in materials such as composites, and aluminium since the invention of the fixed wing aircraft, monoplane (single wing) designs of high span length, and high aspect ratio are entirely possible. As discussed in section 3.4.1, a high aspect ratio is desirable from a drag reduction perspective, thus, a single wing design is chosen.

The vertical location of the wing also plays a role in the aerodynamic performance of the aircraft. The choices for the vertical location of the wing are general described as either high wing, mid-wing, low wing and parasol wing (Sadraey, 2013). For the design of the UAV, the

parasol configuration was ignored, due to it having similar performance to a high wing, with more weight (Sadraey, 2013).

The high wing has the following advantages and disadvantages relevant to the UAV design (Sadraey, 2013).

Advantages:

- Increases the lateral stability of the aircraft, due to the effect of the fuselage contribution to the dihedral affect.
- Wing produces more lift compared to a mid and low wing configuration.
- Generally, the high wing configuration allows more space inside the fuselage for avionics, fuel and payloads.

Disadvantages:

- The aircraft will have a larger frontal area than compared with a mid-wing configuration, increasing the drag.
- The high wing will produce more induced drag, due to the higher lift coefficient.
- The ground effect will be lower when compared to a mid or low wing configuration, increasing take-off run.
- The horizontal tail area of a high wing tends to be approximately 20% larger than a low wing due to the increased downwash.
- A high wing is approximately 20% heavier than a low wing.

On the other hand, the low wing features the relevant advantages and disadvantages below (Sadraey, 2013).

Advantages:

- Take-off performance is better than a high wing.
- The aircraft is lighter when compared with a high wing.
- The frontal area, and thus drag, is less than a high wing.
- The low wing has less induced drag.
- The low wing features less downwash over the tail, so the tail size may be smaller.
- The tail is lighter than a high wing configuration.
- The wing drag produces a nose-down pitching moment, so it is longitudinally stable.

Disadvantages:

- Produces less lift than a high wing configuration.
- The wing is less laterally dynamically stable, due to the lower contribution of the fuselage to the dihedral affect.

In general, the advantages and disadvantages of the mid-wing can be deduced from the reasoning behind the advantages and disadvantages of the high and low wings. In reality, depending on exact location and parameters, the performance of a mid-wing will lie between that of a high wing and low wing, with the extra features listed below (Sadraey, 2013).

- The aircraft is generally slightly heavier, due to the reinforcement requirements of passing the wing directly through the fuselage.
- A mid-wing is more expensive when compared to the other configurations.
- A mid wing is more streamlined than the other configurations.
- The mid-wing features less interference drag than the low or high wing configurations.

With the advantages and disadvantages of the three main vertical wing locations listed above, a mid-wing design was chosen. This was mainly due to the performance benefits between the low and high wings, along with the reduction in interference drag and more streamlined structure, which can have an enormous benefit for a long endurance aircraft.

5.3.1.2 Aerofoil Selection

The aerofoil selection plays a critical role in the performance of the wing. There are hundreds, if not thousands of documented aerofoil sections, developed for many different uses. If desired, an aircraft specific aerofoil section may also be designed, tailoring the performance of the aerofoil to the aircraft mission. The preference for this study would have been to design a mission specific aerofoil, however, this can take an extensive amount of time, and requires extensive aerodynamic experience and knowledge, and is out of the scope of this study. Thus, the decision was made to choose an existing, well documented aerofoil profile.

The aerofoil needs to generate the required lift for the UAV design, while maintaining as little drag as possible. Other beneficial characteristics of the aerofoil will be a high maximum lift coefficient, reducing the stall speed of the UAV, a docile stall profile, if a stall were to occur, making it easier for the pilot or autopilot to recover from the stall, and a low moment coefficient, which needs to be countered with the horizontal tail design, increasing drag.

Several aerofoils were considered for the UAV wing design, after many iterations, the aerofoils selected for detailed analysis were the Clark-Y, the NACA4415 and the NACA 63(4)-421 aerofoil. The quantitative comparison of these aerofoils is given in APPENDIX B.1, as obtained from (Airfoil Tools, 2020). The aerofoils show similar performance at the Reynolds numbers required. After detailed comparison (and a few iterations in xflr5 with 3D wings with all the aerofoil profiles as well), the NACA 63(4)-421 was chosen due to its smaller moment coefficient, and higher thickness to chord ratio, allowing a stiffer, stronger wing structure to be designed during the structural stages of the UAV development.

5.3.1.3 Wing Planform, Setting Angle, Washout, Dihedral and Sweep

A rough size for the wingspan, as well as the required wing area was already determined in section 5.1 and was used as a starting point for the wing planform design. With this defined area and span, the goal of achieving a taper ratio of 0.2 to 0.4 was set, while maximising the aspect ratio as discussed in section 3.4. This will result in the most aerodynamically efficient wing within the given constraints. The combination of the wing setting angle, as well as the washout is selected to give the wing an elliptical lift distribution (increasing the efficiency factor), while generating the required lift during cruising flight, which results in an aerodynamically efficient wing design.

Another parameter to define, is that of the wing dihedral angle. Adding dihedral gives an aircraft roll stability, which is desirable for most aircraft (as long as too much roll stability does not exist) (Sadraey, 2013). However, adding dihedral also reduces the effective planform area of a wing, thus reducing the lift generated and decreasing aerodynamic efficiency (Sadraey, 2013). Along with this, a high aspect ratio aircraft tends to add dihedral due to the elasticity of the wing lifting the wingtip during flight. For these reasons, it was chosen not to add dihedral to the UAV design, and the dihedral angle was left at 0°.

Lastly, the wing sweep angle needs to be defined. Sweep is generally used on high-speed aircraft in order to delay the compressibility effects, and thus, improve wing aerodynamic features such as lift and drag (Sadraey, 2013). An increase in wing sweep angle also decreases the wings efficiency factor and increases wing complexity and manufacturing costs (Sadraey, 2013). For these reasons, the wing sweep angle was kept constant at the quarter chord.

With these constraints and the selected aerofoil, defining the remainder of the wing parameters is an iterative process, having to balance the required lift, while minimising drag. It should be noted that this iterative process also includes the tail design, as the tail, particularly the horizontal tail, needs to be designed in parallel with the wing, as the wing downwash and moment coefficient are all determining factors of the tail design, and can influence the overall performance of the UAV. The tail design is discussed in more detail in the subsequent chapters, but after the performed iterations, the final wing parameters were chosen as Table 5-3 below. The calculated wing area, aspect ratio and Mean Aerodynamic Chord are as reported from the xflr5 calculations, which included a small gap between the centre of the wings for the fuselage.

Table 5-3: Defined Wing Parameters of Initial UAV Design

Wing Parameter	Value	Units
Wing Planform Area	5.58	m^2
Numbers of Wings	1	N/A
Vertical Position on Fuselage	Mid	N/A
Root Aerofoil	NACA 63(4)-421	N/A
Tip Aerofoil	NACA 63(4)-421	N/A
Root Chord	0.8	m
Tip Chord	0.35	m
Wingspan	10	m
Aspect Ratio	~17.9	N/A
Taper Ratio	2.286	N/A
Wing Sweep (at quarter chord)	0	°
Mean Aerodynamic Chord	0.604	m
Wing Setting Angle	6	°
Washout	4	°
Dihedral	0	°

The wing design parameters given above were chosen with aerodynamic efficiency in mind. The taper ratio, high aspect ratio and wing washout all contribute towards an elliptical lift distribution (and thus aerodynamic efficiency), while keeping the wing simple to manufacture. The combination of the root and tip chords and wingspan provide the required wing area, and finally, the aerofoil profile chosen behaves well at the expected Reynolds Numbers.

The resulting wing design proved to be efficient, and with brief initial calculations, met the defined requirements, while adding some extra advantages as well.

5.3.2 Horizontal and Vertical Tail

The primary function of the horizontal and vertical tails is to provide stability and control to the aircraft. The horizontal tail provides longitudinal stability and control, while the vertical tail provides directional stability and control. For a surveillance UAV, the goal is once again to provide the required margins of stability and control with these tails, while minimising weight and drag. The horizontal tail also must be looked at in conjunction with the designed wing, as the downwash from the wing can influence the effective Angle of Attack of the horizontal tail, and the tail is also required to overcome the moment produced by the wing design. Similar parameters must be selected for the tail as that of the wing, again, a brief discussion to the reasoning behind the key decisions made towards these parameters is discussed, followed by the tabulated selected parameters. For the purposes of this research, the theory of stability and control will not be covered, and only the physically selected tail parameters, which resulted in a statically stable UAV design, will be defined.

5.3.2.1 Tail Configuration

There are several tail configuration options to choose from (Sadraey, 2013). Without going into detail on each configuration, and the advantages and disadvantages thereof, only the selected tail configuration, and the reasoning behind its selection, will be discussed here.

The tail configuration for the UAV aerodynamic design was chosen to be a Y-tail configuration, which incorporates a V-tail with an extra vertical tail underneath the fuselage (Sadraey, 2013). The V-tail section provides extra roll stability to the UAV, without sacrificing the performance that would be required by adding this “dihedral” to the main lifting surface, the wing. The V-tail, on its own, also reduces the total tail area required for stability and control (Sadraey, 2013). However, this tail area benefit is slightly offset in the Y-tail configuration, but the Y-tail configuration has the benefit that, if the control surfaces are sized correctly, a failure of one of the control surfaces during flight, would still allow sufficient stability and control of the UAV. This adds redundancy to the control surfaces and is one of the main reasons for selecting the Y-tail configuration. The Y-tail also has the benefit that most of the tail sits outside of the wake of the wing, reducing downwash over the tail, and improving aerodynamic efficiency. Lastly, the vertical tail portion of the Y-tail also serves as protection for the propeller (in a pusher propeller configuration) during take-off and landing, with an over rotation of the UAV resulting in a strike of the vertical tail, and not the propeller.

5.3.2.2 Tail Aerofoil Selection

A horizontal and vertical tail, depending on the control required, and the centre of gravity location, are sometimes required to generate positive lift, and sometimes negative, thus, a symmetrical aerofoil section, producing similar lift in positive and negative angles of attack, is commonly used (Sadraey, 2013). Several aircraft designs use the NACA 0009 or 0012 sections for this reason (Sadraey, 2013). These symmetrical sections provide a good balance of lift and drag for a tail section, and for both the V-section, as well as the vertical tail, a NACA0012 section was selected as the root aerofoil, and a NACA0009 section as the tip aerofoil. This will allow for greater structural rigidity at the root of the aerofoil, while providing a thinner section, and better aerodynamic performance, towards the tip.

5.3.2.3 Tail Setting Angle

If a non-movable tail is selected, the tail setting angle needs to be determined. The purpose of the tail setting angle for the horizontal tail is to help longitudinally balance the aircraft during cruising flight without any control inputs being required. The horizontal tail setting angle, as discussed in the wing section above, was iteratively determined in combination with the wing design in order to longitudinally balance the aircraft during cruise, while minimising the drag.

The setting angle of the vertical tail can also be used to offset yaw affects, such as a yaw moment being produced by the propeller, and its aerodynamic interaction with the fuselage

(Sadraey, 2013). As the propeller is not the topic of this research, the vertical tail setting angle was set at 0°.

5.3.2.4 Tail Volume Coefficient, Moment Arm, and other parameters

As stated before, the primary concern of the tail is to provide stability and control to the aircraft. In order to accomplish this, the tail needs to be placed and sized correctly in relation to the aircraft wing (Sadraey, 2013). The combination of the tail location and size relative to the wing, can be given a dimensionless parameter known as the tail volume coefficient. It is defined as equation (5.1) below for the horizontal tail volume coefficient, and equation (5.2) for the vertical tail volume coefficient.

$$\bar{V}_H = \frac{l_H}{\bar{C}} \frac{S_H}{S} \tag{5.1}$$

Where $\bar{V}_H$ is the horizontal tail volume coefficient, l_H is the distance between the horizontal tail and wing aerodynamic centres, $\bar{C}$ is the MAC, S_H is the horizontal tail effective area and S the wing planform area.

$$\bar{V}_V = \frac{l_V S_V}{bS} \tag{5.2}$$

Where $\bar{V}_V$ is the vertical tail volume coefficient, l_V is the distance between the vertical tail aerodynamic centre and the wing/fuselage aerodynamic centre, S_V is the vertical tail planform area and b the wingspan.

Typical values for the horizontal and vertical tail volume coefficients for a sailplane (which are normally designed for aerodynamic efficiency) are 0.6 and 0.03 respectively (Sadraey, 2013). Thus, these values were used as a starting point for the tail parameters, however, the volume coefficient of the vertical tail was reduced to account for the V-tail performing some of the function of the vertical tail section.

This, in combination with the aerodynamic decisions relating to the wing, again formed the basis of several iterations towards arriving at a suitable tail design, in combination with the designed wing.

The final parameters for the initial design of the UAV are included in Table 5-4 and Table 5-5 for the horizontal and vertical tails respectively.

Table 5-4: Defined Horizontal Tail Parameters of Initial UAV Design

Horizontal Tail Parameter	Value	Units
Planform Area	0.98	m^2
Tail Configuration	Y-tail	N/A
Root Aerofoil	NACA 0012	N/A
Tip Aerofoil	NACA 0009	N/A
Root Chord	0.5	m
Tip Chord	0.25	m
Wingspan (Projected)	2.61	m
Aspect Ratio	10.26	N/A
Taper Ratio	2	N/A
Horizontal Tail Sweep (at quarter chord)	0	°
Mean Aerodynamic Chord	0.39	m
Horizontal Tail Setting Angle	-1	°
Washout	1	°
Dihedral	36	°
Horizontal Tail Moment Arm	2.42	m
Horizontal Tail Volume Coefficient	0.57	N/A

Table 5-5: Defined Vertical Tail Parameters of Initial UAV Design

Vertical Tail Parameter	Value	Units
Planform Area	0.19	m^2
Root Aerofoil	NACA 0012	N/A
Tip Aerofoil	NACA 0009	N/A
Root Chord	0.5	m
Tip Chord	0.25	m
Wingspan	0.5	m
Aspect Ratio	1.32	N/A
Taper Ratio	0.5	N/A
Vertical Tail Sweep (at leading edge)	0	°
Mean Aerodynamic Chord	0.39	m
Wing Setting Angle	0	°
Washout	0	°
Dihedral	0	°
Vertical Tail Moment Arm	2.42	m
Vertical Tail Volume Coefficient	0.008	N/A

The tail configuration and design parameters outlined above give good aerodynamic performance with low drag, while providing sufficient longitudinal and directional stability to the aircraft.

5.3.3 Landing Gear Configuration

For a UAV that is sized to meet the current requirements, it can be safely assumed that landing gear and a runway will be used as a Take-Off and Recovery method. Other methods, such as hand launch, or catapult launch, are not viable for a UAV of this size. Most UAVs of this size and larger, also feature retractable landing gear as seen in section 1.2.3. Retractable landing gear can be rather complex to design from a mechanical point of view and add significant mass to any aircraft design. However, for a surveillance UAV that requires long endurance, the aerodynamic benefit is needed, as landing gear that are in the airflow for the entire flight regime, can add significant drag. Thus, retractable landing gear will be selected.

Where the design and/or aerodynamic analysis of the landing gear is not required for the current work, the landing gear configuration, as well as a general size and weight must be determined in order to correctly design the fuselage as the landing gear configuration can have a significant impact on this design. The landing gear configuration, its position in the fuselage or wing, and its mass, can have a significant impact on the aerodynamic performance of the UAV. Besides take-off and landing, the landing gear also allow ease of taxiing at any airfield that may be used.

For the initial design, a tricycle landing gear configuration was selected. This configuration is the most popular landing gear configuration (Sadraey, 2013). It features many benefits, including direction stability while on the ground, ease of rotation on take-off, and plenty of ground clearance at the rear-end of the aircraft (Sadraey, 2013). The rear ground clearance is important for the current design, as the selected configuration is a pusher aircraft, which features a propeller at the rear of the aircraft “pushing” it forward. The clearance is important for propeller tip clearance.

Without going into too much detail of the design specifications of the UAV landing gear, the gear was added to the CAD model to represent location, length, as well as a mass estimate, this allowed for a much more accurate design of the fuselage taking the landing gear into account.

5.3.4 Propulsion

The propulsion system of a UAV serves two purposes, the main one being to generate the thrust needed to maintain level flight. However, UAV propulsion systems also have the function of generating power for the UAV electronics and other auxiliary systems (Sadraey, 2013). With this is mind, a propulsion system capable of generating auxiliary power needs to be selected.

The goal of this UAV design is endurance, while speed or power are not deciding factors. Therefore, an engine system that can produce the required power, while being as small, light and efficient as possible is required. Piston-prop and turboprop engine systems offer the highest efficiency and lowest specific fuel consumption (Sadraey, 2013). Turboprop systems

are however too powerful for the required application, and so a piston-prop engine is selected. Other options, such as solar and hydrogen power were considered as well, but these options are either not mature enough, or offer various other disadvantages over a piston-prop, that resulted in their selection being ruled out.

In terms of engine location, a pusher configuration was selected. The pusher configuration offers various advantages for a surveillance UAV, the two main advantages being that the entire fuselage does not sit in the wake of the propeller, which would decrease aerodynamic efficiency, and the fact that with the engine in the rear of the aircraft, all the camera equipment (including that required to fly the UAV remotely), can sit in the front of the UAV without obtrusion. Again, where a specific UAV engine and propeller was not required to be selected for the purposes of the current work, it needs to be considered for the aerodynamic configuration of the fuselage. An NWUAV Rotron RT600LCR-EFI engine was selected, as it provides the required power, and added to the CAD model to assist in engine bay design and Centre-of-Gravity (COG) location (Northwest UAV, 2019). Along with all its required auxiliary systems, including a generator to provide power to all the UAV electronics. The engine, as well as all its sub-system masses and volumes are included in Table 5-2 above.

5.3.5 Fuselage

The main purpose of the fuselage is to house all the required systems, payloads and fuel, while being as aerodynamically efficient, and as light weight as possible. This aerodynamic efficiency can be in the form of generating as little drag as possible, and possibly also assisting with lift generation. Luckily, for a UAV, crew members and human personnel do not have to be accounted for, and most of the items to be housed by the fuselage for the purposes of this work are those in Table 5-2 above.

The fuselage for the initial UAV design was designed around all the required components with their respective volumes, while maintaining COG requirements and aerodynamic efficiency. Extra space was also allowed for volumes not included for the purposes of this work, including control surface motors, and structural requirements.

A fuselage length to hydraulic diameter ratio also exists which will minimise the drag during flight (Sadraey, 2013), this ratio was aimed for during the design of the fuselage. Also worthy of note is that extra features, which also affect aerodynamic performance, were added to the fuselage design in order to obtain a more representative performance. These features are not the purpose of the present study but were added as they do influence the aerodynamic performance of the UAV. These features include the camera payload, the engine cooling cowling, exhaust exit, and the propeller hub. The features added will serve as a starting point for future studies, and more detailed design stages.

5.3.6 Final Design of Initial UAV Configuration

The final design of the initial UAV configuration, with all the features discussed above, is shown in Figure 5-2, Figure 5-3 and Figure 5-4 below. The fuel volumes can be seen in yellow, the extra volume of the wing design was taken advantage of and used as fuel storage, which would also reduce the bending moment of the wing root during flight.

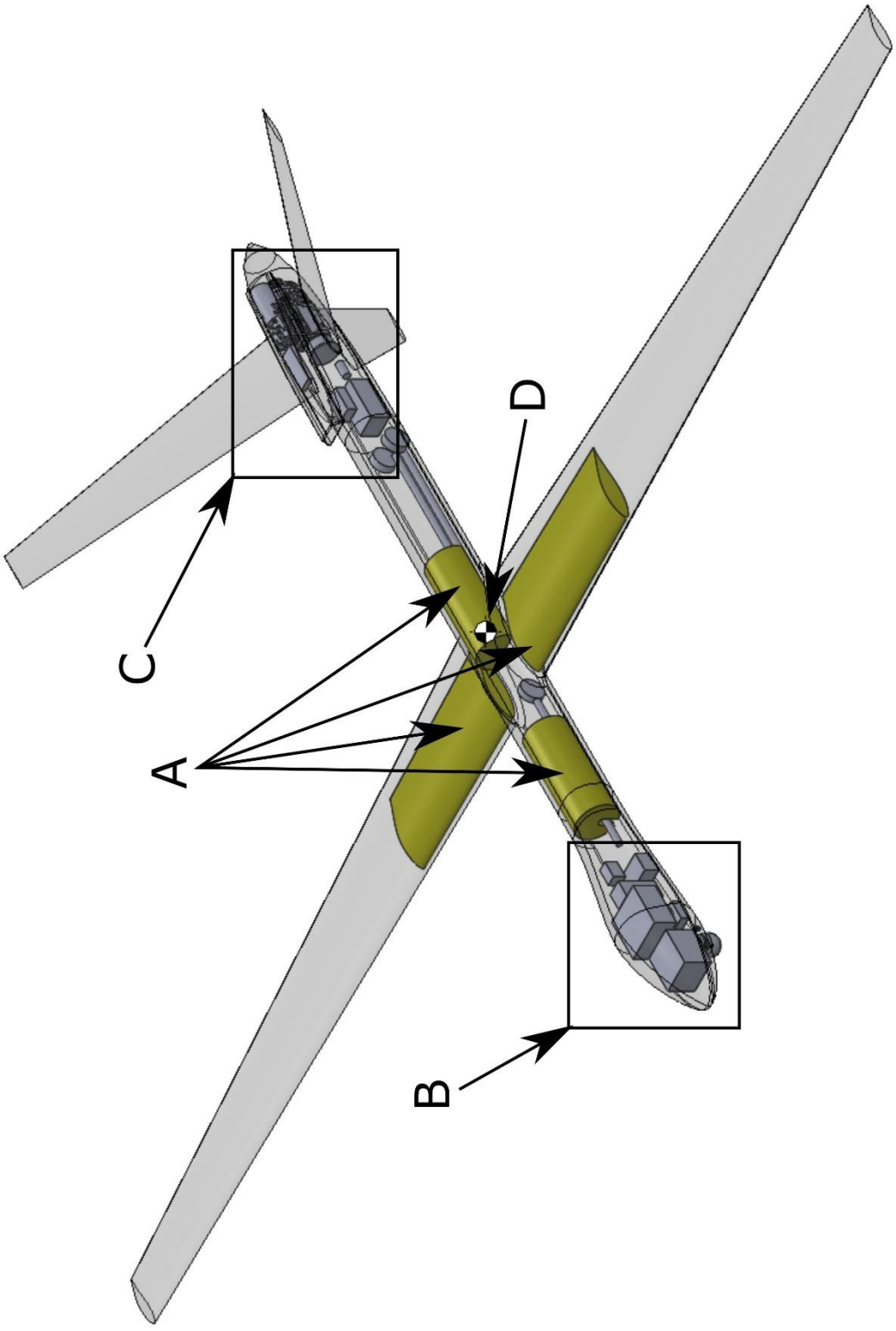

Figure 5-2: Isometric View of Initial UAV Design showing A) Fuel System, B) Payload and communication systems, C) Engine and associated Systems and D) COG Location

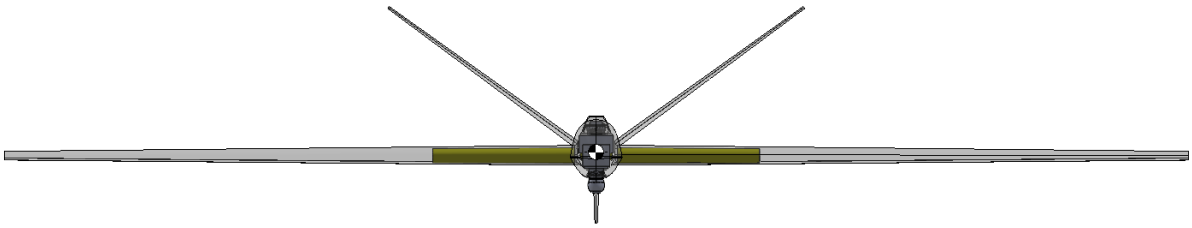

Figure 5-3: Front View of Initial UAV Design

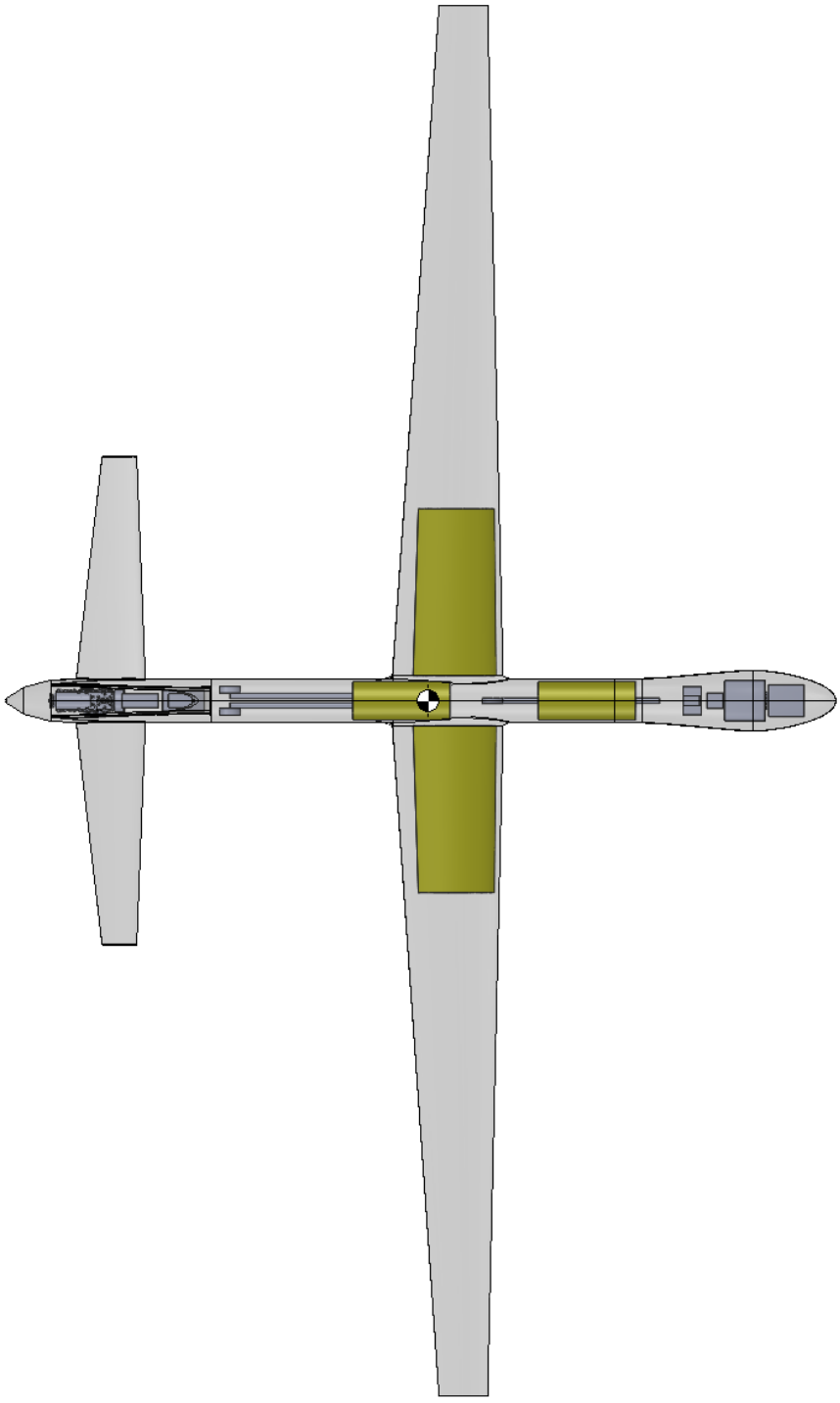

Figure 5-4: Top View of Initial UAV Design

CHAPTER 6: CFD of Initial Design

6.1 Validation

The case selected for validation of the method to be used for the CFD analysis, is that of the American Institute of Aeronautics and Astronautics (AIAA) 1st CFD High Lift Prediction Workshop (also known as HiLiftPW-1). All the details, presentations, and data of this workshop are available from (American Institute of Aeronautics and Astronautics, 2010).

This workshop is a well-documented workshop, with wind tunnel test results, and CFD results available from several authors and companies, with both quantitative and qualitative data available, using many different solvers and turbulence models. The results of which are all tabulated and presented showing the validity of the CFD results using the different grids, turbulence models and solvers. The case itself will briefly be discussed, followed by the performed grid generation, CFD setup and results of the case, and finally, the outcomes of the validation investigation will be presented.

6.1.1 Case and Geometry

The HiLiftPW-1 case was selected as it involves complex geometry and flow patterns (namely, the slats and flaps), this results in not only flow separation, but also flow reattachment, which is challenging to correctly predict using CFD (American Institute of Aeronautics and Astronautics, 2010). Not only this, but the geometry itself is of comparable Reynolds number to the UAV design. This, along with the fact of how well documented the case is, and that it has both wind tunnel tests, and investigation outcomes from leading CFD experts, makes it an ideal case to use for validation purposes. The geometry was downloaded from the workshop and imported into Solidworks and is shown in Figure 6-1 below. In this figure, the fact that symmetry is being used to the advantage of the study is clearly seen (half model). What is also clearly seen is the leading-edge slat, the trailing edge flap, and the main centre wing section, which adds aerodynamic complexity to the case.

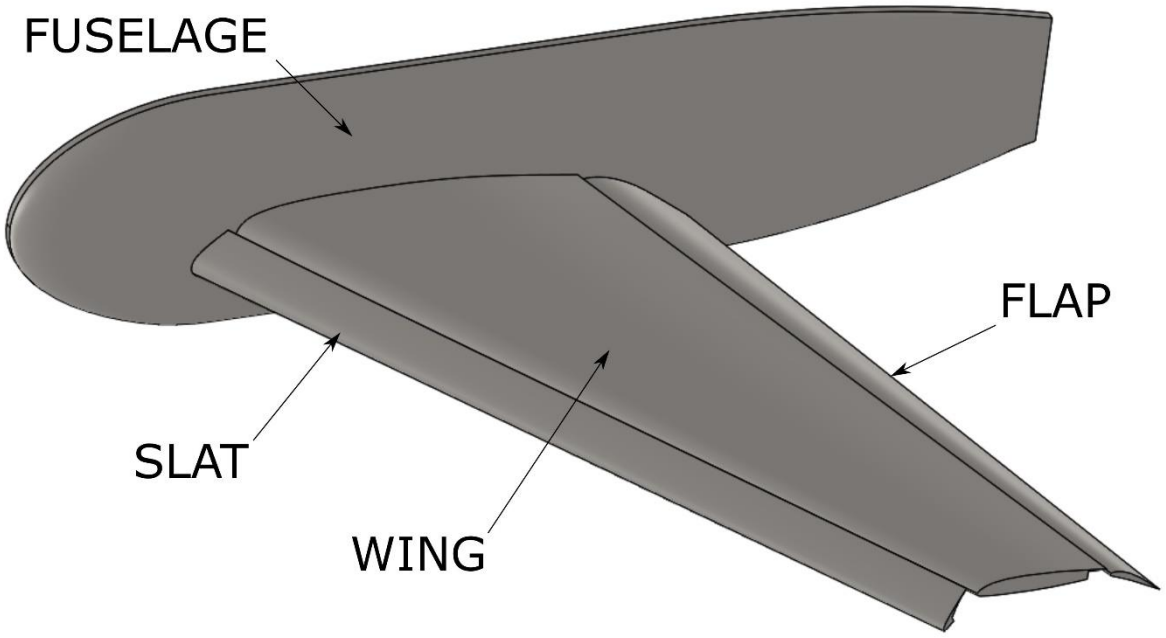

Figure 6-1: HiLiftPW-1 CAD Geometry (American Institute of Aeronautics and Astronautics, 2010)

The key values used for the simulation are included in Table 6-1 below, again, all the data is provided from (American Institute of Aeronautics and Astronautics, 2010), but is repeated here for easy reference. The turbulence intensity included in the table below, is obtained from the NASA wind tunnel report (Neuhart & McGinley, 2004).

Table 6-1: Key Values for HiLiftPW-1

Property	Value	Units
Mach Number	0.2	N/A
Analysed Angles of Attack	6, 13, 21, 28, 32, 34, 37	Degrees
Reynolds Number (based on MAC)	4.3×10^6	N/A
Reference Temperature	288.889	K
Reference Area	2.0465	m^2
Mean Aerodynamic Chord	1.0067	m
Moment Reference	0.8722868, -0.02413, 0 (x, y, z)	m
Turbulence Intensity	0.07	%

6.1.2 Grid Generation

The HiLiftPW-1 workshop provides both gridding guidelines for the workshop and several grids of different resolutions and types (namely, structured, and unstructured grids), allowing participants of the workshop to use either the provided grids, or to generate their own. For the purposes of this study and since the workshop is being used as a validation case for new geometry, a new grid was generated, following the gridding guidelines provided by the workshop where possible. Worthy of note is the fact that the generated grid used a far-field boundary condition of a distance of 100 times the reference chord length (provided in Table

6-1 above) in all directions and used several bodies of refinement in the grid domain to refine the regions of flow where high gradients were expected. This includes the gaps between the wing and the slat and flap, the area near to the geometry of the aircraft, and several refinement zones in the wake of the geometry to correctly capture the wake. Figure 6-2 below shows the entire fluid domain with far-field boundaries, the wake refinement regions can also be seen in the figure as the darker zones in the centre of the domain. Figure 6-3 shows the wake refinement regions in closer detail, three successively larger bodies are used, increasing the cell size with each. And finally, Figure 6-4 shows the refinement regions close to the geometry of interest, the red refinement region controls the cell size near the body, and the blue zones control the cell size in the gaps between the slat, flap, and wing. They are also used to control the cell size on the leading and trailing edges of the wing zones, which are highlighted by (American Institute of Aeronautics and Astronautics, 2010) as areas of required refinement.

As noted by the AIAA grid generation guidelines (American Institute of Aeronautics and Astronautics, 2010), as well as (ANSYS INC, 2018), and discussed in section 4.5 of this paper, possibly the most critical factor required to accurately model the results of this case, is correctly resolving the turbulent boundary layer. As such, the boundary layer grid was generated with all the requirements of the AIAA grid generation guidelines in mind, as well as the recommendations laid out in the ANSYS Fluent Theory Guide for grids using the Transition SST turbulence model (ANSYS INC, 2018, pp. 77-80).

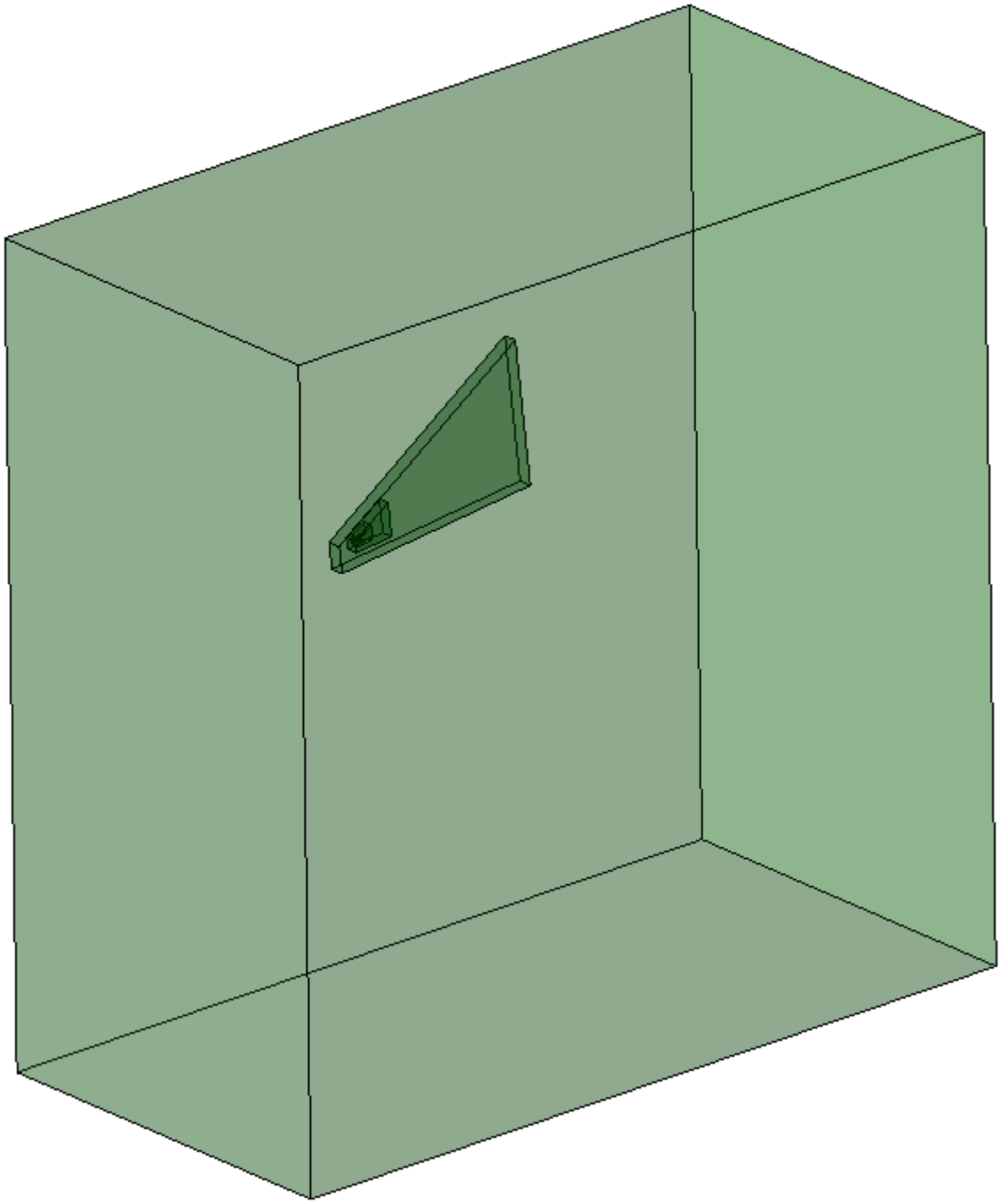

Figure 6-2: Entire Computational Domain for Validation Case

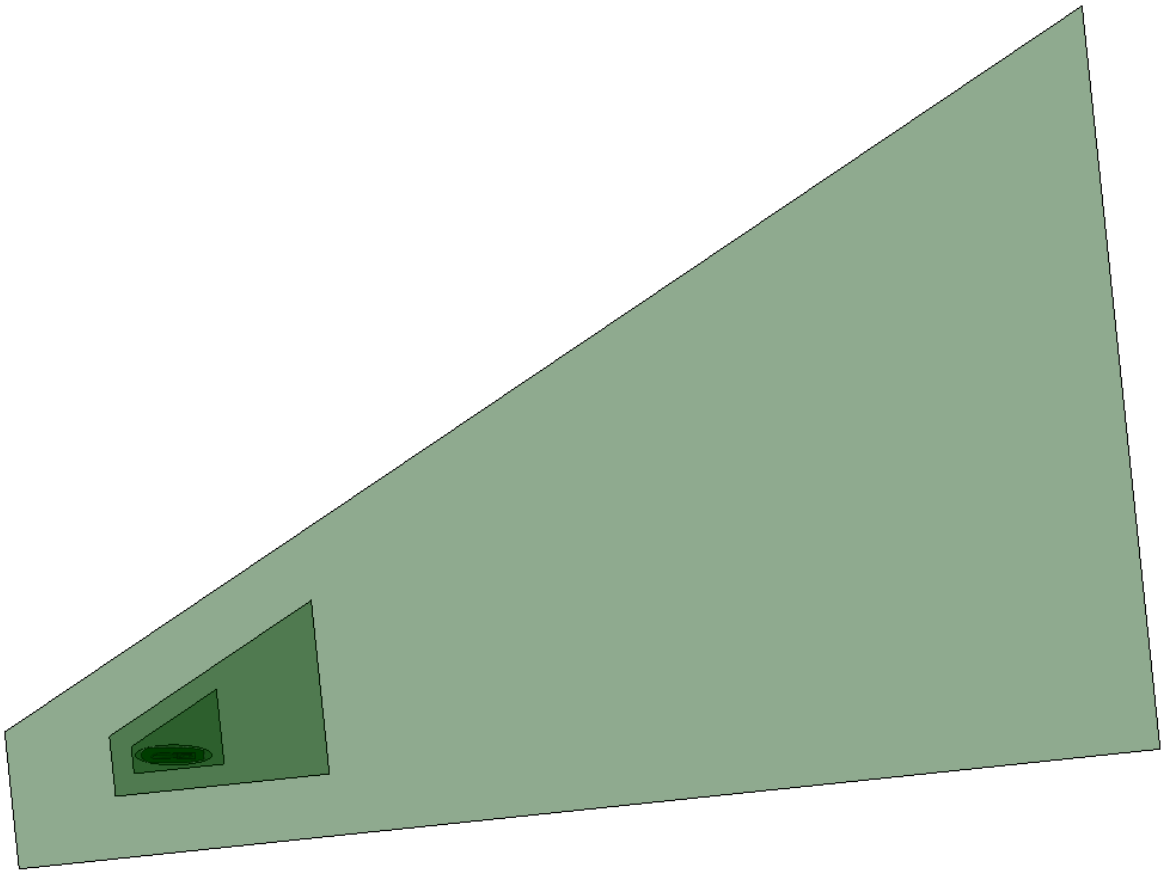

Figure 6-3: Validation Case Wake Refinement Regions (Green)

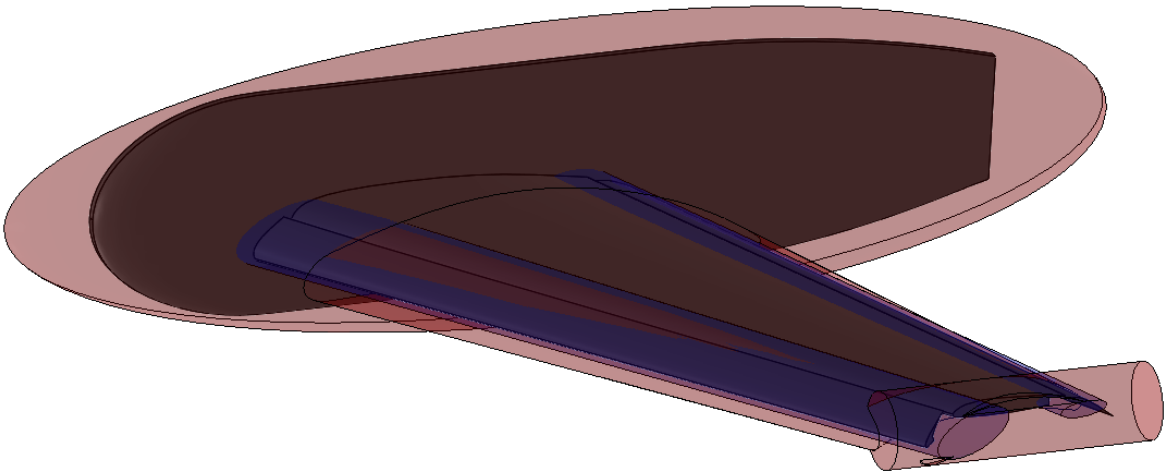

Figure 6-4: Validation Case Body Refinement Regions (Red) and Slat and Flap Refinement Regions (Blue)

Using these refinement zones, and the grid generation guidelines as discussed above, a Poly-Hexcore grid was generated using ANSYS Fluent Meshing. The resulting grid is shown in Figure 6-5, Figure 6-6, Figure 6-7 and Figure 6-8 below, where the refinement near the main body, slat and flap can be clearly seen. Worth noting, is that the HiLiftPW-1 workshop called for several levels of grids, with cell counts ranging from approximately 3 million cells, up to 160

million cells (Chaffin, 2010). With the grid convergence behaviour for unstructured grids showing good agreement to the wind tunnel results for lift, drag and moment behaviour, with approximately 20 to 30 million cells. This was therefore used as a target for the number of cells to be generated for the grid. The final grid contained just less than 22 million cells.

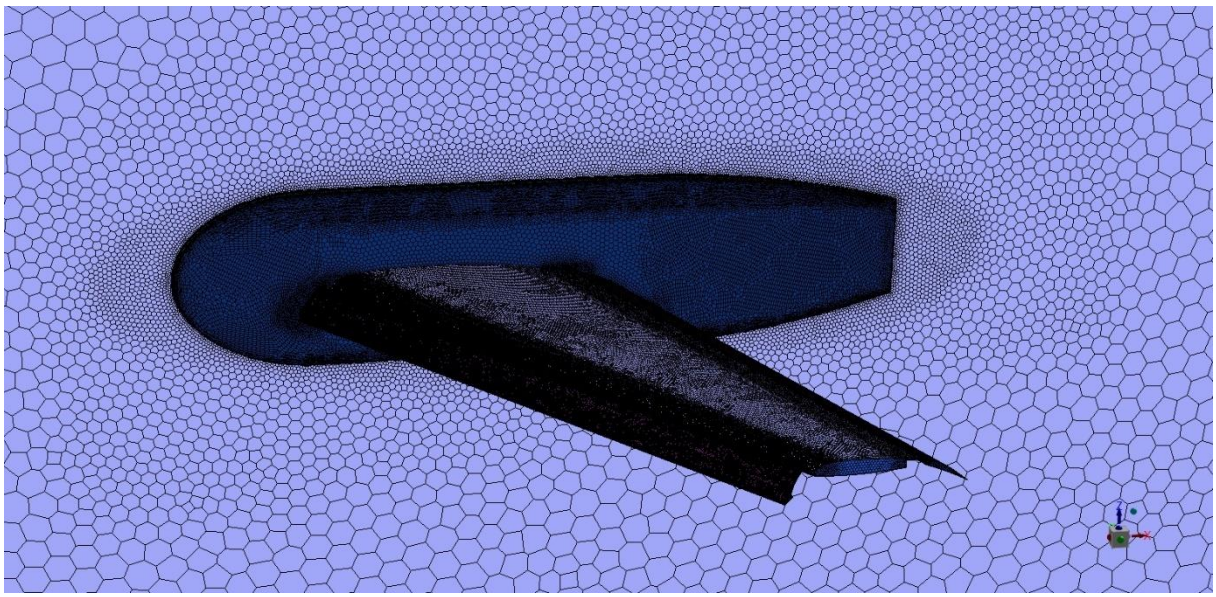

Figure 6-5: Generated Grid for Validation Case

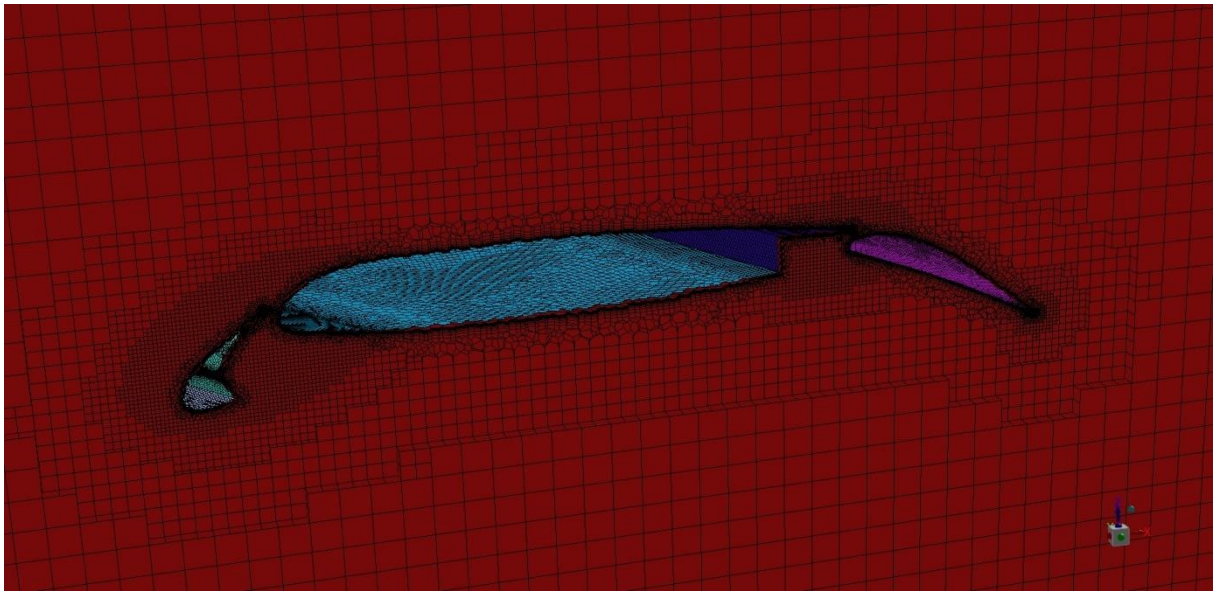

Figure 6-6: Section of Grid through Wing, Slat and Flap Geometry

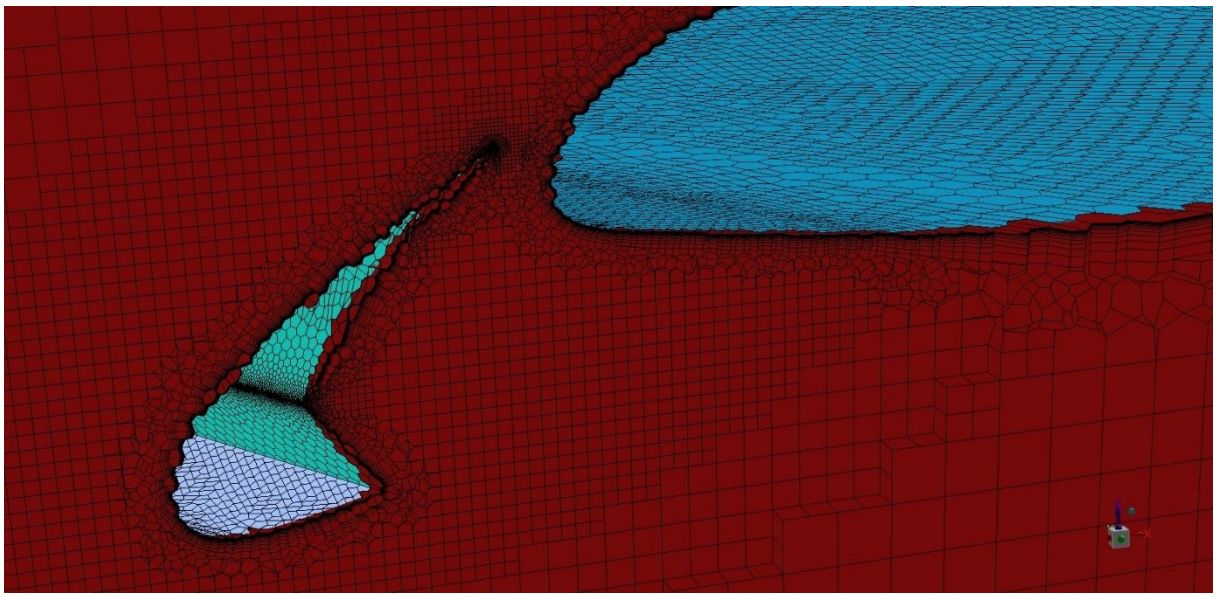

Figure 6-7: Closeup of Section of Grid Near Slat

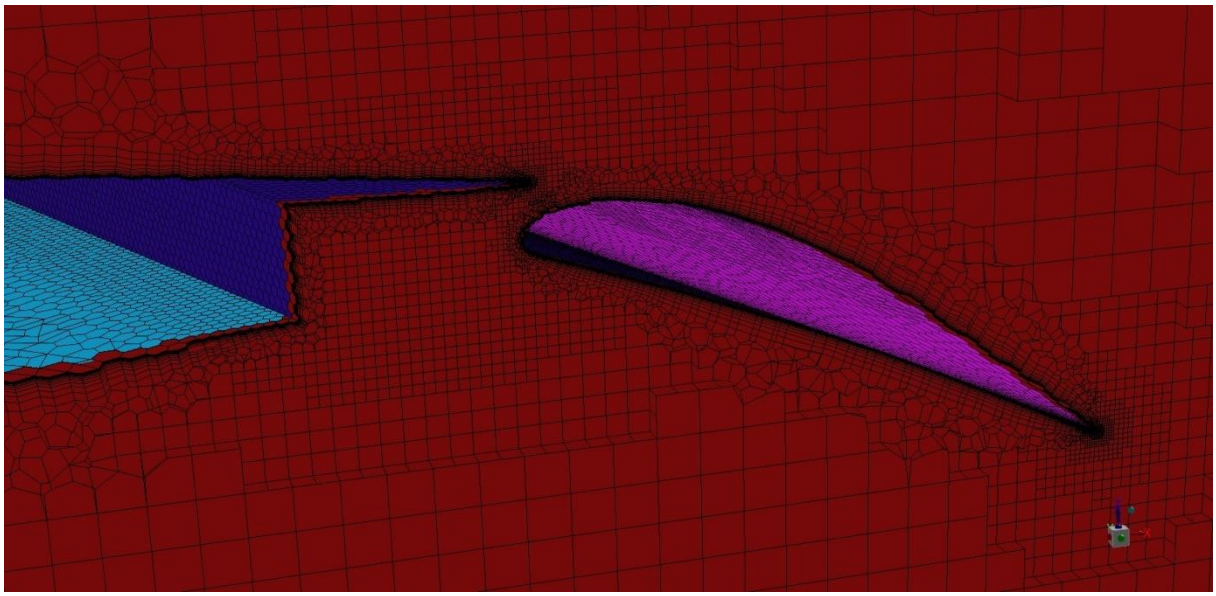

Figure 6-8: Closeup of Section of Grid Near Flap

6.1.3 Simulation Setup

All the required parameters for the simulation setup were already defined by (American Institute of Aeronautics and Astronautics, 2010).

The turbulence model selected for the validation case was the Transition SST model. Where a simpler, full turbulence model such as the Spalart-Allmaras model, would be suitable for the validation case, the Reynolds numbers present in the actual UAV analysis would be lower than the validation case. This lower Reynolds number, and higher area of laminar zones, can play a significant role on the drag predicted in cruising flight (Chen, et al., 2020) (Swart, 2020). As the Transition SST model was selected for the UAV CFD analysis, the validation case will need to follow suit. The other settings used for the solver setup are shown in Table 6-2 below.

Table 6-2: Ansys Fluent General Settings for Validation Case

Property	Value	Units
Precision	Double	N/A
Solver Type	Pressure-Based	N/A
Time	Steady	N/A
Space	3-Dimensional	N/A
Energy	On	N/A
Turbulence Model	Transition SST with Fluent default values	N/A
Density	Ideal-gas with Fluent default values	N/A
Viscosity	Sutherland Law with Fluent default values	N/A
Operating pressure	101325	Pascal
Pressure Velocity Coupling Scheme	SIMPLE	N/A
Spatial Discretization		
Gradient	Least Squares Cell Based	N/A
Pressure	Second Order	N/A
Density	Second Order Upwind	N/A
Momentum	Second Order Upwind	N/A
Turbulent Kinetic Energy	Second Order Upwind	N/A
Specific Dissipation Rate	Second Order Upwind	N/A
Intermittency	Second Order Upwind	N/A
Momentum Thickness Re	Second Order Upwind	N/A
Energy	Second Order Upwind	N/A

The reference values used for the calculation of the coefficients have already been provided in Table 6-1, and where some of the values from this table will be repeated below, the full definitions of the boundary conditions are provided for clarity.

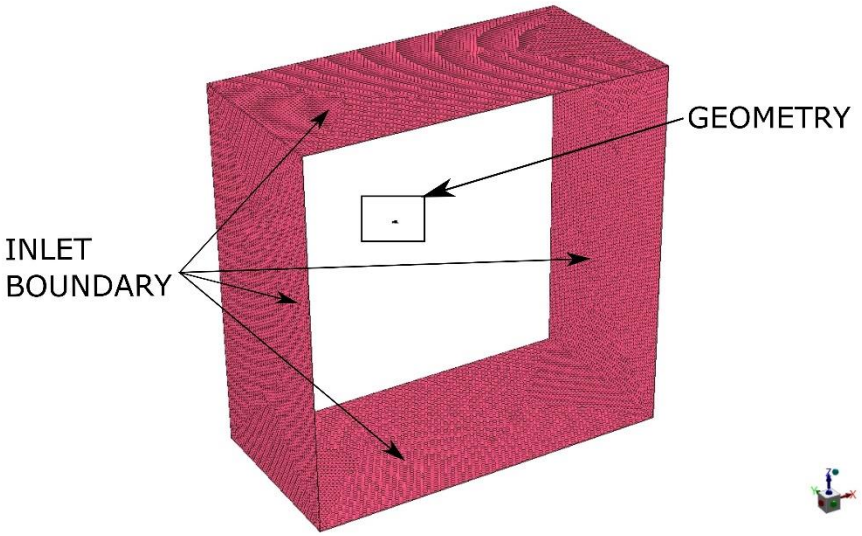

Figure 6-9: Inlet Boundary

Figure 6-9 above shows the inlet boundary surfaces, the small spec in the middle of the image is the HiLiftPW-1 geometry, here the extent of the domain around the geometry can be seen. The values used for the inlet boundary condition are given in Table 6-3 below.

Table 6-3: Properties for Inlet Boundary Condition

Property	Value	Units
Boundary Type	Inlet, Pressure Far-Field	N/A
Gauge Pressure	0	Pascal
Mach Number	0.2	N/A
Turbulence Intermittency	1	N/A
Turbulent Intensity	0.07	%
Turbulent Viscosity Ratio	1	N/A
Temperature	288.89	K

The symmetry plane of the geometry, as well as the plane parallel to the symmetry plane outboard of the wing were given symmetry boundary conditions.

And finally, the HiLiftPW-1 geometry, coloured in grey below, is given the no-slip wall boundary condition.

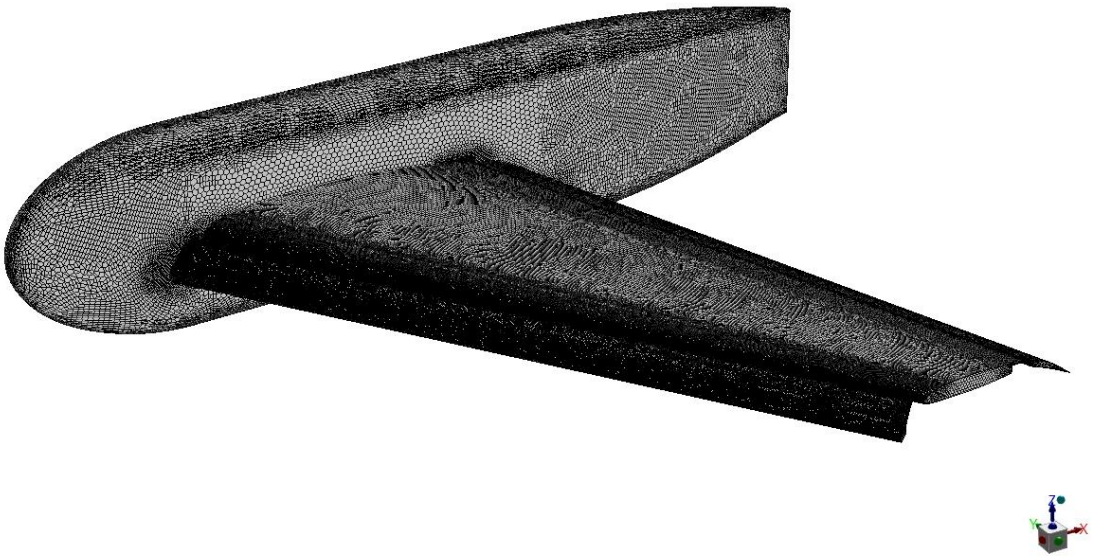

Figure 6-10: No-Slip Wall Boundary Condition (Grey)

6.1.4 Results

Using the grid and simulation setup described above, the results obtained are given in Table 6-4 below with the percentage differences indicated between the author's CFD results, and that of the NASA Wind Tunnel (WT) experiments, where the lift, drag and moment coefficients

are compared to the wind tunnel tests performed by NASA for the AIAA in terms of percentage difference.

Table 6-4: Authors CFD Results with Percentage Difference to NASA WT Results

AOA [°]	Lift Coefficient	Drag Coefficient	Moment Coefficient	Lift Difference [%]	Drag Difference [%]	Moment Difference [%]
6	1.5593	0.201	-0.50665	1.9	-1.3	2.2
13	2.049	0.32823	-0.49974	0.1	-1.5	-0.7
21	2.5899	0.51546	-0.49671	0.3	-1.7	0.1
28	2.9462	0.69146	-0.49666	1.2	0.8	8.9
32	2.9539	0.74098	-0.37993	-1.3	-1.4	-8.3
34	2.9844	0.77776	-0.34734	-0.2	0.2	-7.3
37	2.0282	0.85717	-0.20805	-8.8	-0.8	1.7

These results are also given in the form of graphs, comparing the validation lift, drag and moment coefficients, to that of the NASA WT experimental results below. The lift, drag and moment graphs are given in Figure 6-11, Figure 6-12 and Figure 6-13 respectively.

Good agreement with the experimental results was obtained, with the lift being within 2 percent of the experimental results, besides one point at 37 degrees AOA, where it proved difficult to correctly match wind tunnel results because of the high levels of flow separation, which is difficult to correctly predict using CFD (Rumsey, 2010). The drag was also within 2 percent for all points, and the moment coefficients within 9 percent. The moment coefficients are slightly harder to predict using CFD for such a complex case, as is noted by (Rumsey, 2010). With the other participants of the workshop also struggling to predict the moment coefficients with an accuracy better than 10 percent. The cause of the larger difference in moment coefficients, when compared to the difference of the lift and drag coefficients, are currently unknown.

With the good agreement between the results of the CFD analysis, and that of the wind tunnel experiments using this method for validation, the same method was decided to be used for the actual UAV geometry to be analysed, which being a simpler case should obtain similar, if not better, accuracy.

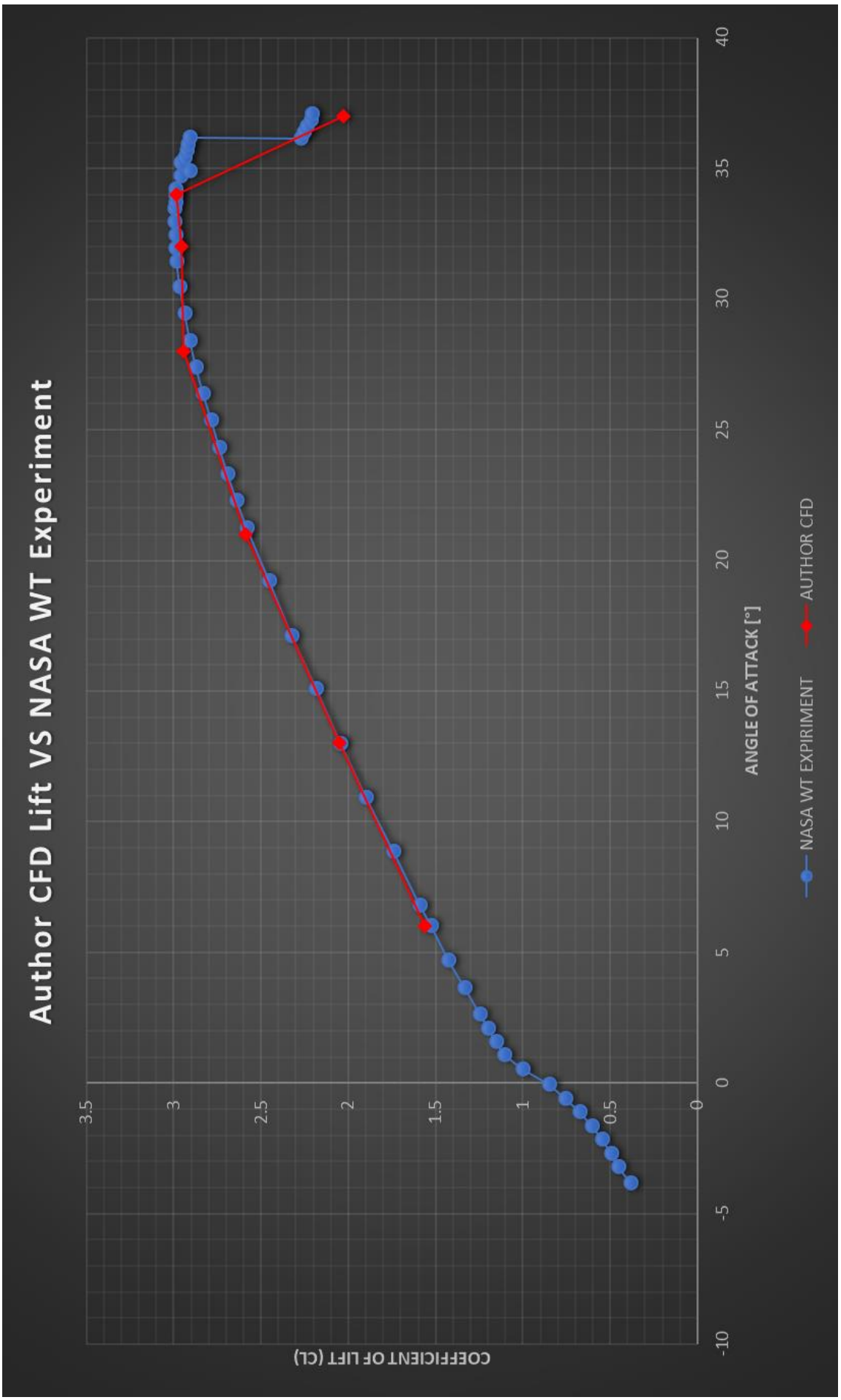

Figure 6-11: Graph of Authors CFD Lift Coefficient Results VS NASA WT Experimental Results

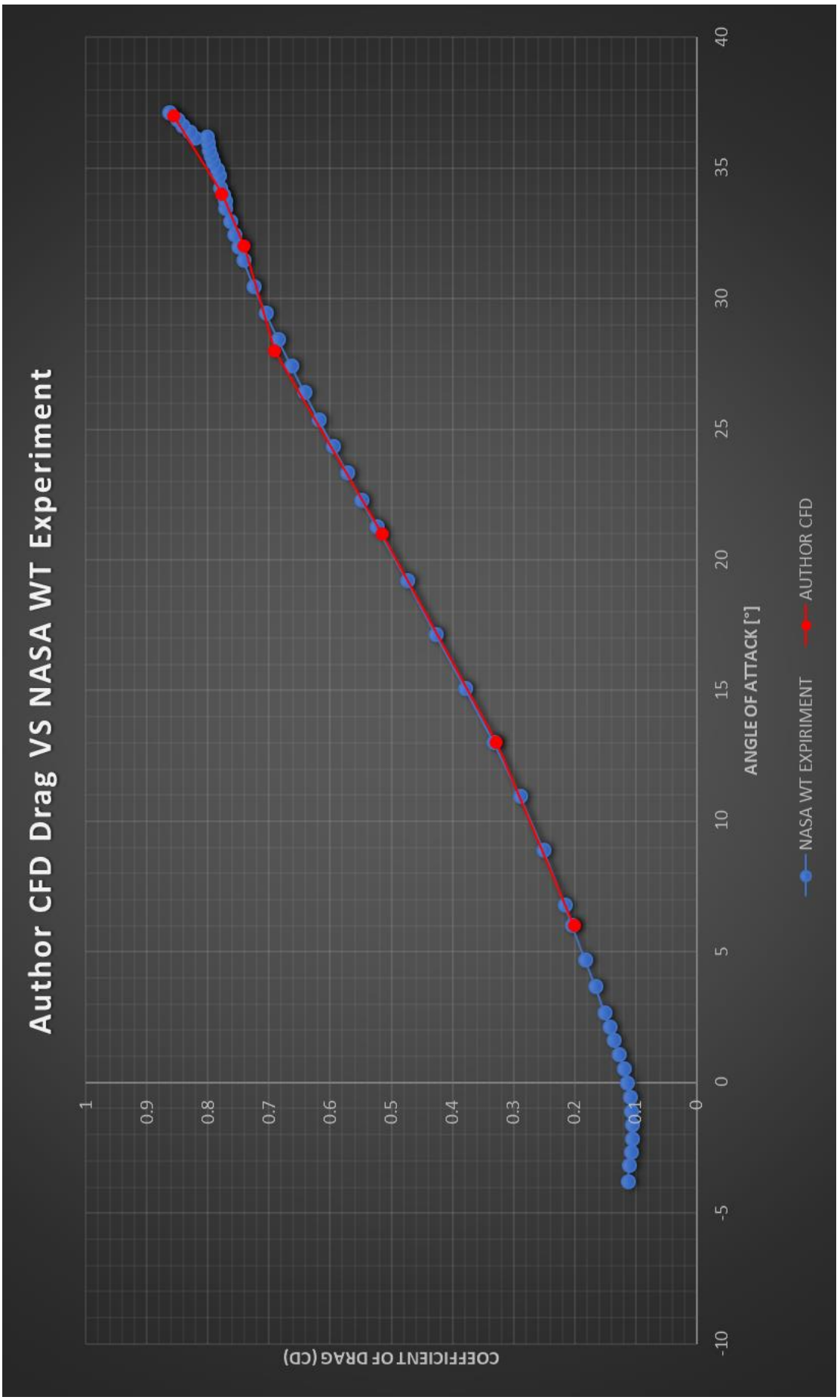

Figure 6-12: Graph of Authors CFD Drag Coefficient Results VS NASA WT Experimental Results

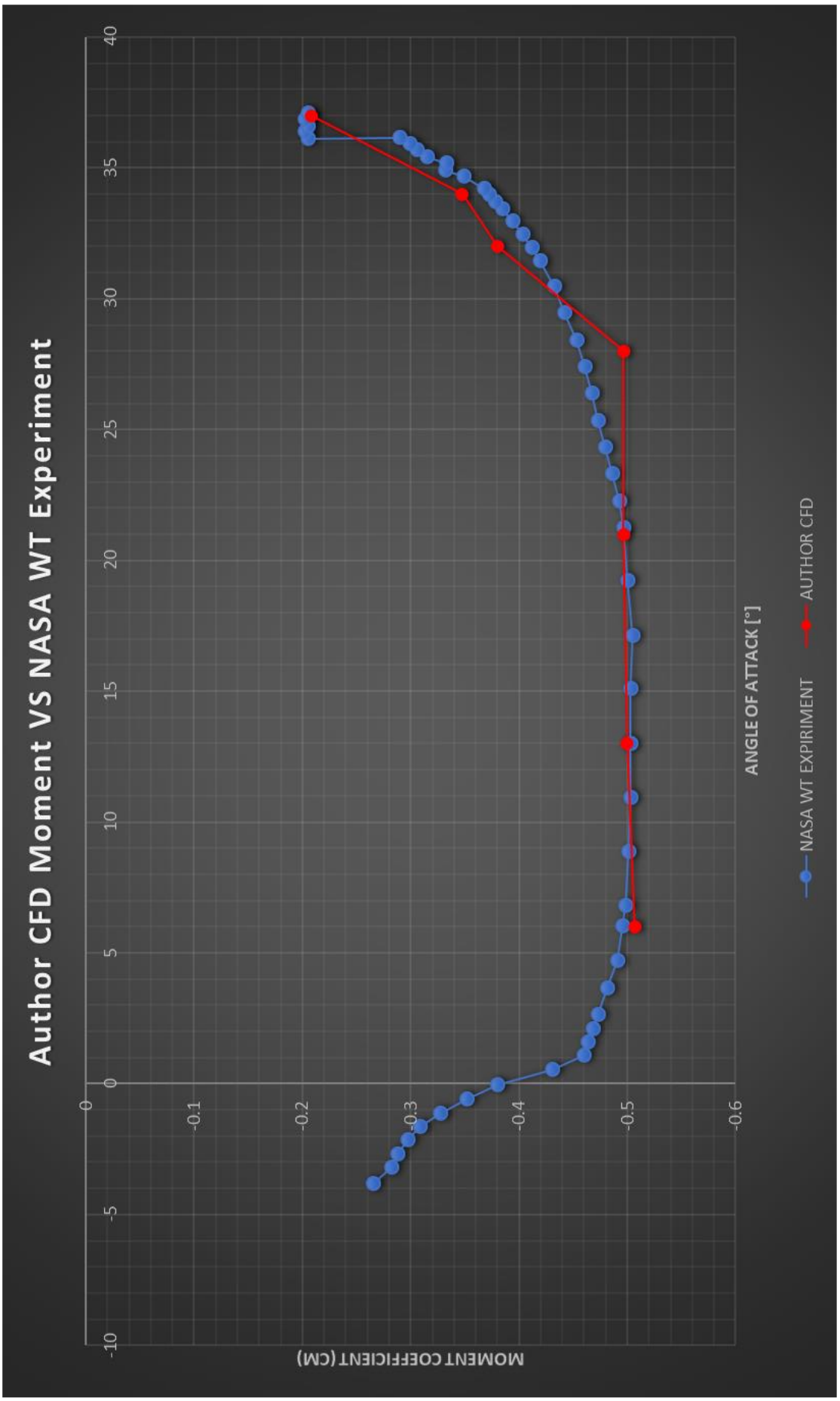

Figure 6-13: Graph of Authors CFD Moment Coefficient Results VS NASA WT Experimental Results

The y^+ values of the simulation at 0 degrees AOA are given in Figure 6-14 below. More than approximately 98% of the first cells have a y^+ less than, or equal to one. The only area with a y^+ larger than 1, is the small area on the tip of the wing. Even with the y^+ of this area being higher than 1, with a maximum value of 3.92, it is only a small area affecting less than 2% of the cells. Small areas of geometry can frequently have a y^+ value higher than 1, without affecting the solution at unreasonable levels, as can be seen by the other CFD participants in the HiLiftPW-1 study which all used the same first cell height. The cell first height was therefore deemed to be suitable. It should be noted that the y^+ was monitored for each angle of attack and deemed to be lower than 1 over at least 90% of the wall area over all angles of attack.

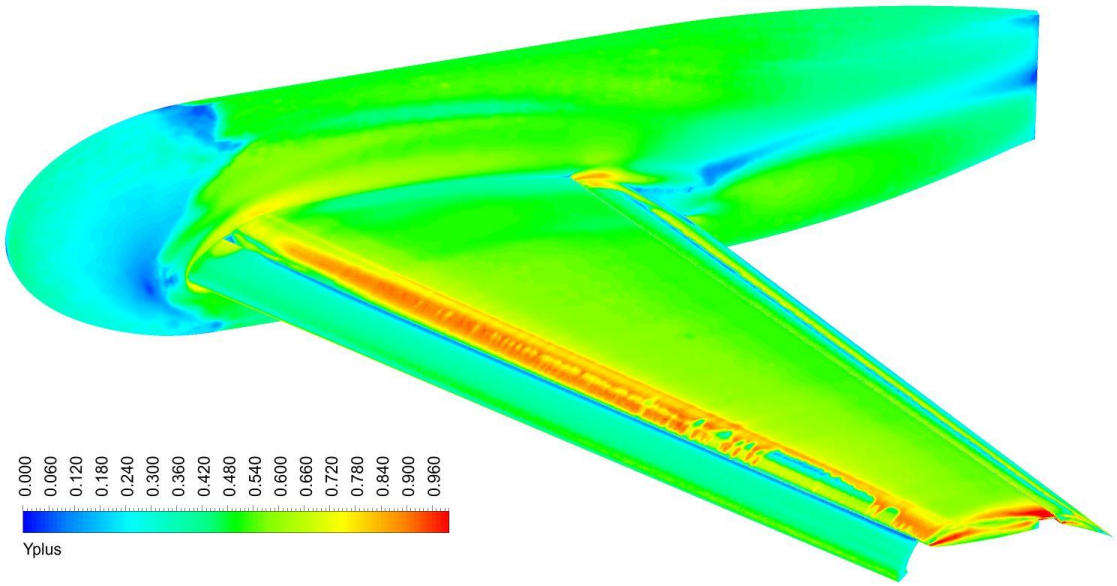

Figure 6-14: y^+ Contour Plot of Validation Case at 0 Degrees AOA

Figure 6-15 below also shows the skin friction coefficient over the HiLiftPW-1 geometry at 28 degrees angle of attack. An interesting phenomenon can be seen here, where in the middle of a high skin friction coefficient, there is a small zone in the streamwise direction of low skin friction coefficient. This small area is believed to be a laminar separation bubble. This phenomenon can be present in the Reynolds number regime expected from the UAV, and thus, the UAV geometry may also contain laminar separation bubbles. If a fully turbulent model, such as the Spalart-Allmaras model was used, this phenomenon would not have been captured or detected in the analysis.

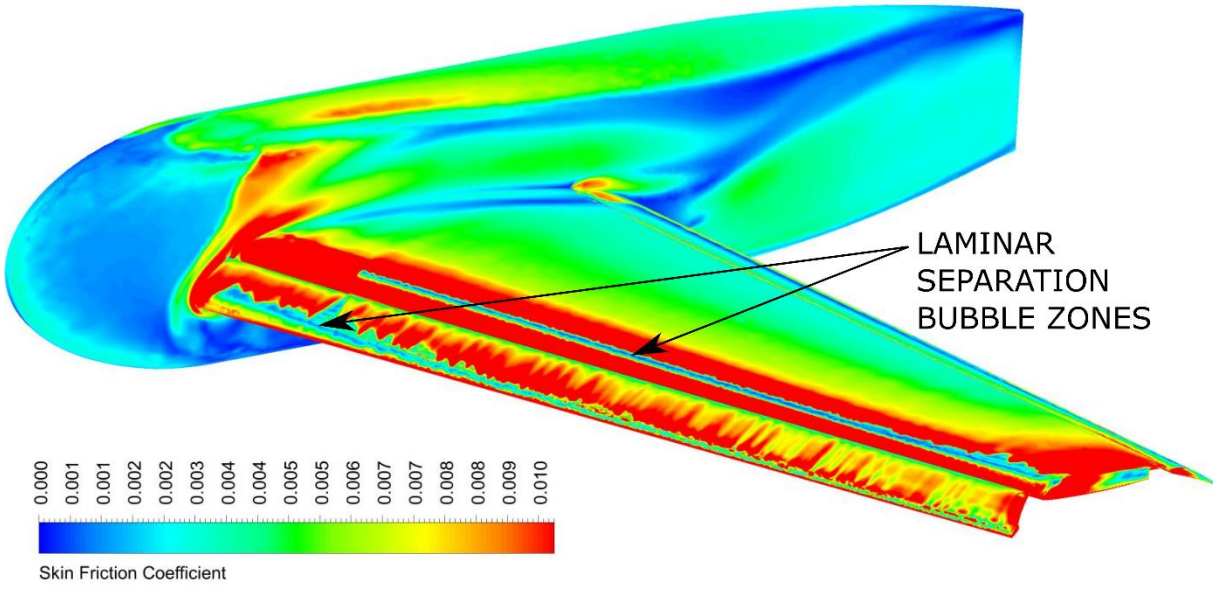

Figure 6-15: Skin Friction Coefficient at 28 Degrees AOA

6.1.5 Outcomes of the Validation Case

Several analysis attempts had to be made to accurately match the NASA WT experimental results. The outcomes of these attempts, that are to be incorporated into the UAV CFD analysis, are briefly discussed here.

6.1.5.1 Cell and Grid Sizing

The main outcome of the validation case was discovering the sensitivity of the results to the size of the grid. The cell sizing in the boundary layer can have significant effects on the onset of separation, the separation location, as well as the severity of the separation. The boundary layer in the validation case had to be refined at angles of attack of 32° and higher in order to correctly capture the separation. If one grid is to be used for all angles of attack, and to capture separation as accurately as possible, a highly refined boundary layer grid will have to be implemented. It should be noted that the solution had to be refined from 22 million to approximately 35 million cells in order to accurately capture the separation at angles of attack of 32° and higher.

6.1.5.2 Hysteresis

The solution displayed hysteresis, particularly near and on the separation angles of attack. In other words, the solution would be different depending on the flow field it was initialised from. The simulation would provide near correct results if initialised from the angle of attack preceding it, for example, starting the 32° simulation, using the results from the 28° angle of attack simulation, would yield near correct results, while starting a 32° solution using the results of the 6° solution, would yield incorrect results. This phenomenon is also documented in the wind tunnel tests (dependent on if the angle of attack was increasing or decreasing), as well

as in the results of other CFD participants of the workshop (Rumsey, 2010). Best practice for the UAV simulations, would be to initialise a new angle of attack simulation, starting from the results of the previous angle of attack.

6.1.5.3 Inlet Turbulence Levels

The results also showed a minor sensitivity (enough sensitivity to be noted), with the inlet turbulence levels used in the simulation. If the ANSYS Fluent default values were used, simulation results could vary by as much as 20%. The turbulence levels present in the wind tunnel experiments by NASA had to be found, and input into the simulation, before more comparable values of lift, drag and moment could be obtained. The turbulence levels, as well as other important criteria in the NASA wind tunnel model used can be found in (Neuhart & McGinley, 2004).

To summarise the outcomes of the validation case, accurate prediction of separation can be difficult to capture using CFD. And CFD results near separation angles of attack, and above should be scrutinized and questioned for accuracy without other data to compare to. The grid and method used for the validation case showed good agreement with the NASA WT results and is deemed acceptable for use with the CFD analysis of the UAV design.

6.2 CFD of Initial UAV Design

With the accuracy obtained using the validation case in section 6.1 above, it was decided to follow the same procedure for the CFD analysis of the initial UAV design, however, with incorporating the outcomes in section 6.1.5 above.

6.2.1 Grid Generation

The grid for the analysis of the UAV was setup using the same guidelines and best practices laid out in section 6.1.2 above. Of course, because the case is slightly different, a few new challenges arose for the grid generation of the UAV geometry.

The UAV geometry is slightly simpler than the validation case in the sense that there are no gaps in the wing for the slats and flaps that require small cells in order to correctly capture the gradients. The cell size for the leading and trailing edges of the UAV geometry was still controlled using Bodies of Influence (BOI) in order to correctly capture the gradients over the wing, and to help with the correct prediction of the separation location over the wing, should separation occur. This is generally best practice for aircraft CFD analysis (American Institute of Aeronautics and Astronautics, 2020). The MAC, and cruise speed of the UAV are also lower than the validation case, allowing for a larger first cell height. This would assist with lowering the cell count in the boundary layer, whilst still having enough cells to correctly capture the boundary layer, and while still meeting the y^+ requirements.

However, the UAV geometry has a much larger surface area than the validation case. Namely, 9.6 m^2 for the validation case, and 12.973 m^2 for the UAV geometry. This would mean that with similar cell settings and sizes on the wall geometry, the UAV geometry would generate a larger number of cells than the validation case geometry, an amount too large for the available computer resources to handle. Thus, the boundary layer cell settings for the UAV case had to be modified slightly, and a balance between cell count and boundary layer settings was found, whilst still maintaining boundary layer cell requirements, y^+ requirements, and best practice guidelines as laid out in (American Institute of Aeronautics and Astronautics, 2010) and (ANSYS INC, 2018).

Similar refinement zones to that of the validation case were used for the UAV grid generation, and they will not be repeated here. A Poly-Hexcore grid was also generated for the UAV geometry, resulting in approximately 34 million cells. This cell count is higher than that used for the validation case for two reasons, namely, to account for the increased surface are of the UAV geometry in comparison to the validation case geometry, and in order to ensure accurate prediction of the separation. As stated in section 6.1 above, the 22 million cell grid of the validation case could not accurately predict the separation, this was considered for the grid generation of the UAV geometry. The resulting grid is shown below in Figure 6-16, Figure 6-17 and Figure 6-18.

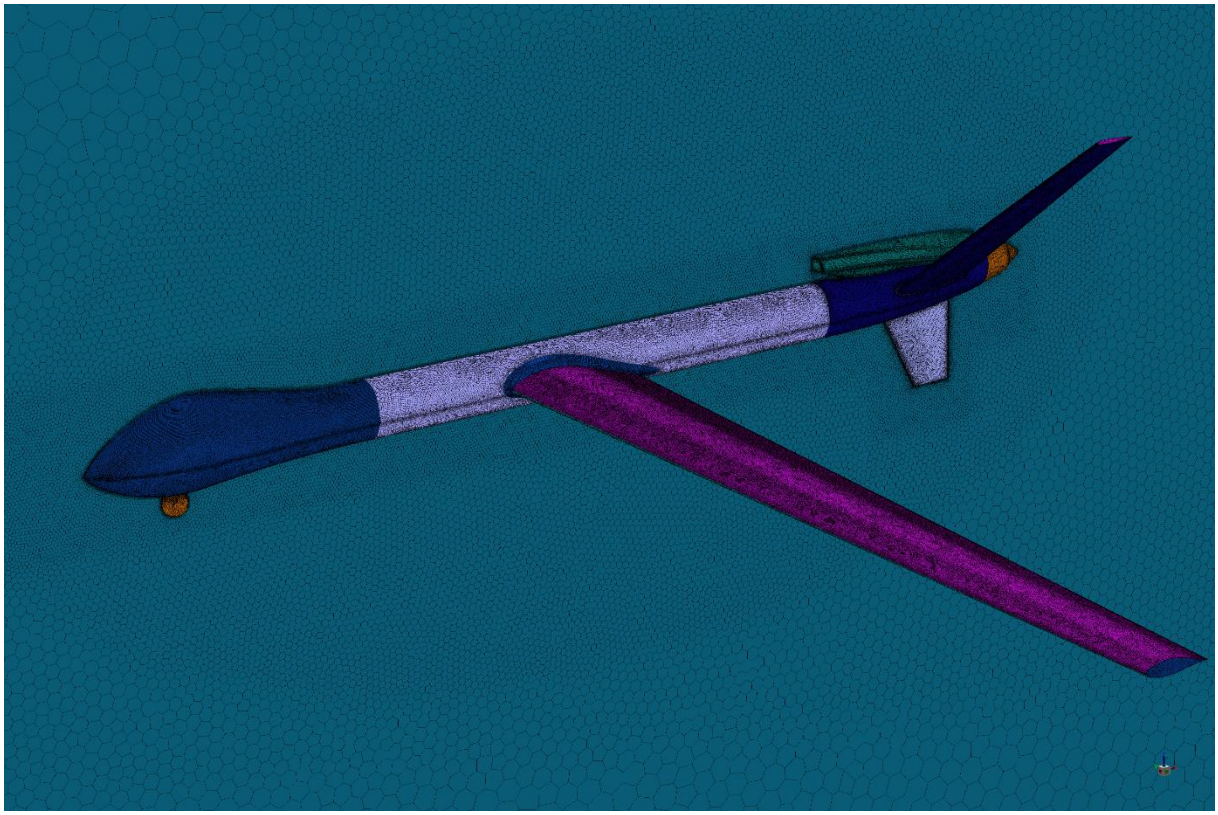

Figure 6-16: Overall Grid of UAV Geometry

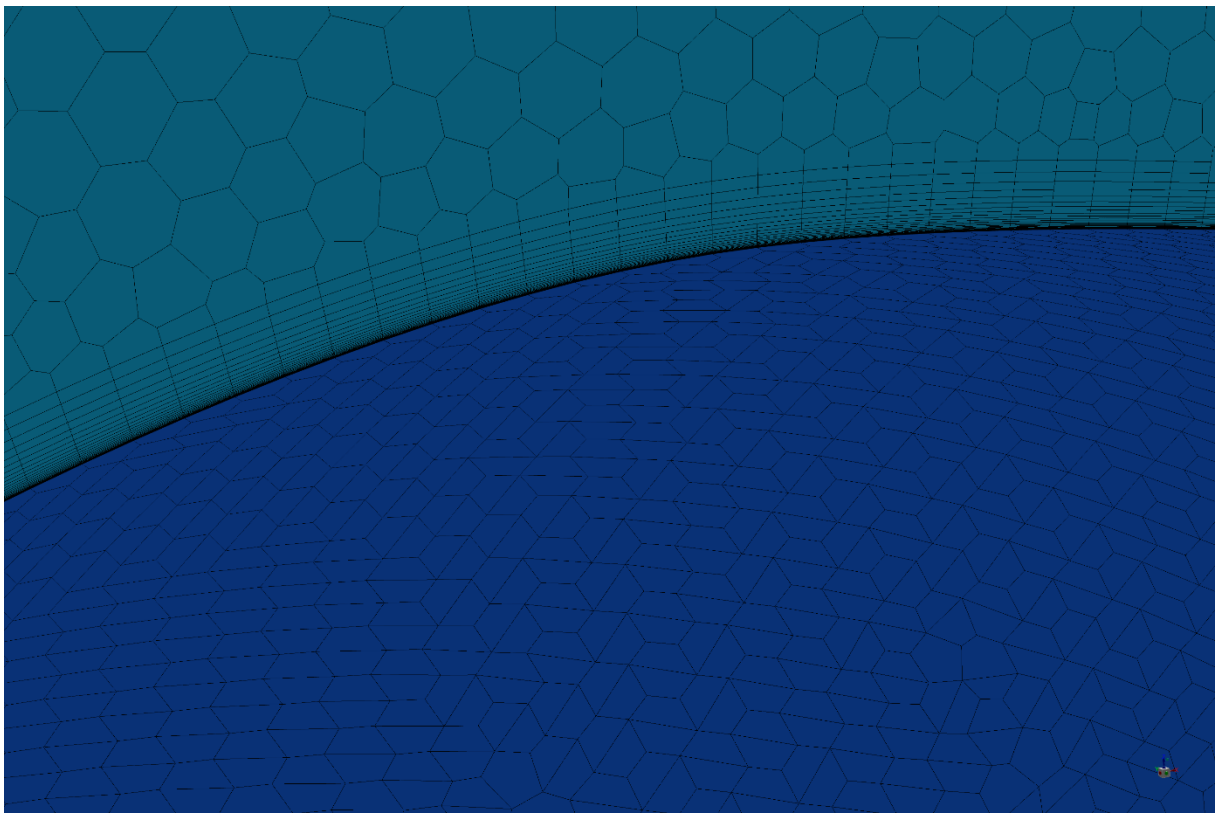

Figure 6-17: Closeup of Grid on Nose of UAV showing Inflation Layers

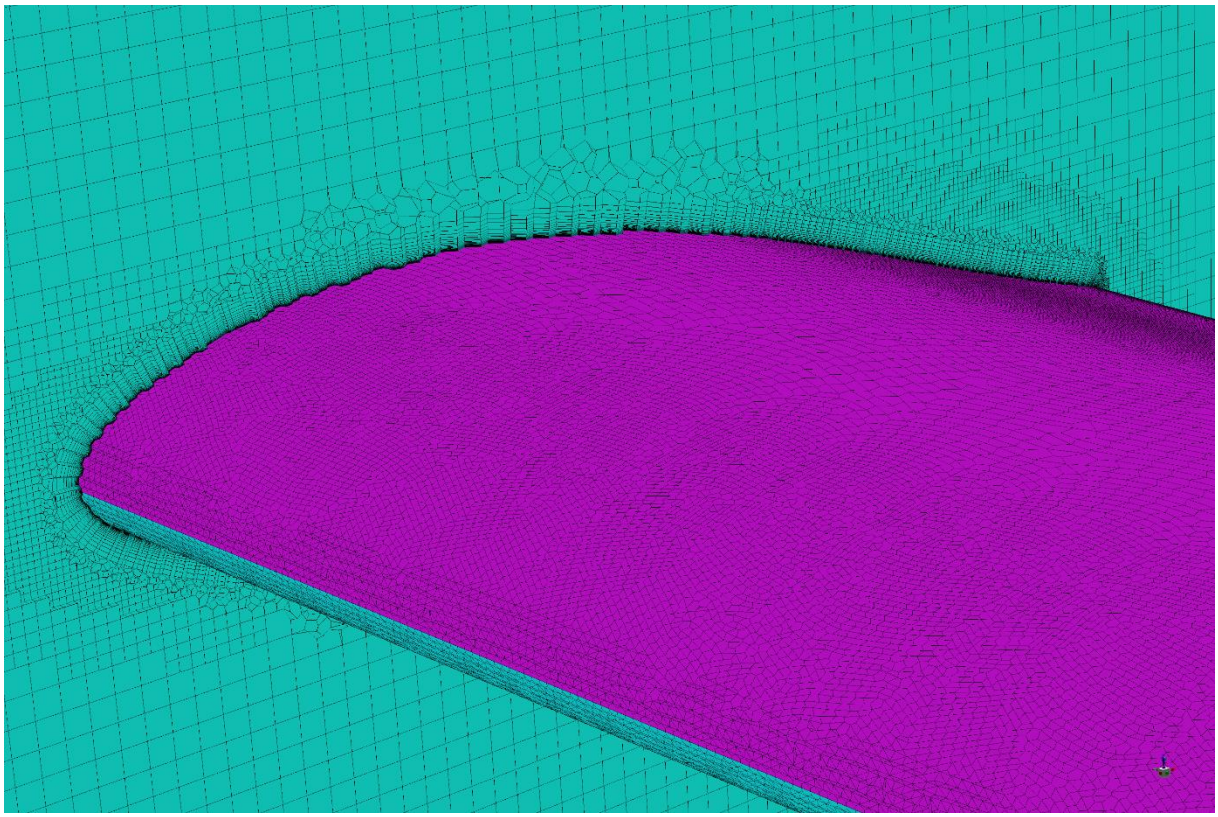

Figure 6-18: Section of Grid over UAV Wing

6.2.2 Simulation Setup

Where possible and applicable, the simulation setup for the UAV CFD was performed with the same parameters as the validation case. However, the UAV, of course, cruises at a particular altitude as defined in the requirements in Table 2-1. This altitude defined the pressure, density and temperature for the UAV CFD analysis. The density at the required altitude, along with the aerodynamic design, determined the required cruise speed, as the air density, the UAV mass and the lift coefficient all play a role in the requirements for steady, level flight. For the purposes of this simulation, the International Standard Atmosphere (ISA) model, at an altitude of 3500 meters (cruise flight) will be used. A small Python script was written, using the Python module named Aerocalc in order to calculate the ISA values, to assist in determining the required CFD input parameters, this script is included in APPENDIX A.3, with the values used for the CFD simulation.

The UAV is designed to be flown at a constant lift coefficient, while varying the speed during flight to account for lost mass as a result of burning fuel. Thus, the UAV, for cruise conditions, has a constant angle of attack, with varying speed during its long endurance cruise. For the initial analysis, it was decided to see the UAV performance over varying angles of attack, to determine an approximate, best performance cruise angle of attack, and help determine areas for optimisation and improvement. Due to limited available computational time and resources, this means that only one speed can be selected for the initial UAV analysis. The speed selected was the minimum cruise speed (using the UAVs lowest predicted mass during cruising flight). The minimum cruise speed was selected, as the airfoil polars of the selected airfoil showed that the performance of the airfoil degrades with the lower Reynolds numbers present at the minimum cruise speed (Airfoil Tools, 2019). These polars are given in APPENDIX B.1 for the readers convenience. Thus, a conservative approach was used for the analysis of the initial UAV simulation by selecting the cruising speed at which lower Reynolds numbers, and thus lower performance, was predicted.

In the case of initial UAV design, common practice seems to be to exclude the effects of the propeller for analysis. Of the 10 papers reviewed in section 1.2 which involve using CFD for initial design of a UAV, only (Kontogiannis & Ekaterinaris, 2013) and (Panagiotou, et al., 2016) include the effects of the propeller. For the purposes of this initial design study, the effects of the propeller will be ignored, this should be the topic of future research and more detailed design. However, a brief study was done to quantify the possible affect a propeller may have after these simulations and is included in section 6.4. The values used for the CFD of the initial UAV design are included in Table 6-5, Table 6-6 and

Table 6-7 below. Images of the boundaries will not be provided, as they are setup in the same manner as the validation case. It should be noted that various moment reference centres were used, as can be seen in Table 6-5 below. This was to assist in the determination of the

aerodynamic neutral point, as the point could not be determined prior to running the simulations, several points had to be used and an interpolation can be performed to confirm that the neutral point is in a suitable area for aircraft stability.

Table 6-5: Reference Values for CFD of UAV

Property	Value	Units
Mach Number	0.107	N/A
Analysed Angles of Attack	-4 to 16 in increments of 2	°
Reynolds Number (based on MAC)	0.971×10^6	N/A
Reference Temperature	265.40	K
Reference Area	2.789	m^2
Mean Aerodynamic Chord	0.575	m
Moment Reference 200	0.2, 0.0, 0.0 (x, y, z)	m
Moment Reference 500	0.5, 0.0, 0.0 (x, y, z)	m
Moment Reference 1000	1.0, 0.0, 0.0 (x, y, z)	m
Moment Reference 1100	1.1, 0.0, 0.0 (x, y, z)	m
Moment Reference 1200	1.2, 0.0, 0.0 (x, y, z)	m
Moment Reference 1300	1.3, 0.0, 0.0 (x, y, z)	m
Moment Reference 1400	1.4, 0.0, 0.0 (x, y, z)	m
Moment Reference 1500	1.5, 0.0, 0.0 (x, y, z)	m

Table 6-6: Ansys Fluent General Settings for CFD of UAV

Property	Value	Units
Precision	Double	N/A
Solver Type	Pressure-Based	N/A
Time	Steady	N/A
Space	3-Dimensional	N/A
Energy	On	N/A
Turbulence Model	Transition SST with Fluent default values	N/A
Density	Idea-gas with Fluent default values	N/A
Viscosity	Sutherland Law with Fluent default values	N/A
Operating pressure	65764	Pascal
Pressure Velocity Coupling Scheme	SIMPLE	N/A
Spatial Discretization		
Gradient	Least Squares Cell Based	N/A
Pressure	Second Order	N/A
Density	Second Order Upwind	N/A
Momentum	Second Order Upwind	N/A
Turbulent Kinetic Energy	Second Order Upwind	N/A
Specific Dissipation Rate	Second Order Upwind	N/A
Intermittency	Second Order Upwind	N/A
Momentum Thickness Re	Second Order Upwind	N/A
Energy	Second Order Upwind	N/A

Table 6-7: Properties for Inlet Boundary Condition for CFD of UAV

Property	Value	Units
Boundary Type	Inlet, Pressure Far-Field	N/A
Gauge Pressure	0	Pascal
Mach Number	0.107	N/A
Turbulence Intermittency	1	N/A
Turbulent Intensity	0.1	%
Turbulent Viscosity Ratio	3	N/A
Temperature	265.40	K

6.2.3 Results

The results for the lift and drag coefficients of the initial UAV design are given below in Table 6-8. Figure 6-19, Figure 6-20 and Figure 6-21 also give results of interest in graph form. The results are discussed after these figures. Suitable convergence was obtained for all results, with the lift, drag, moment, and mass balance all being monitored during each AOA simulation.

Table 6-8: Initial UAV CFD Lift and Drag Coefficient Results

AOA [°]	Lift Coefficient	Drag Coefficient	C_L/C_D	$C_L^{3/2} / C_D$
-4	0.246710	0.020417	12.08	6.00
-2	0.498770	0.023092	21.60	15.25
0	0.741650	0.028361	26.15	22.52
2	0.988760	0.036436	27.14	26.98
4	1.212000	0.047183	25.69	28.28
6	1.414400	0.060288	23.46	27.90
8	1.547200	0.077996	19.84	24.67
10	1.447300	0.127630	11.34	13.64
12	1.434000	0.162190	8.84	10.59
14	1.410000	0.206420	6.83	8.11
16	1.373700	0.259030	5.30	6.22

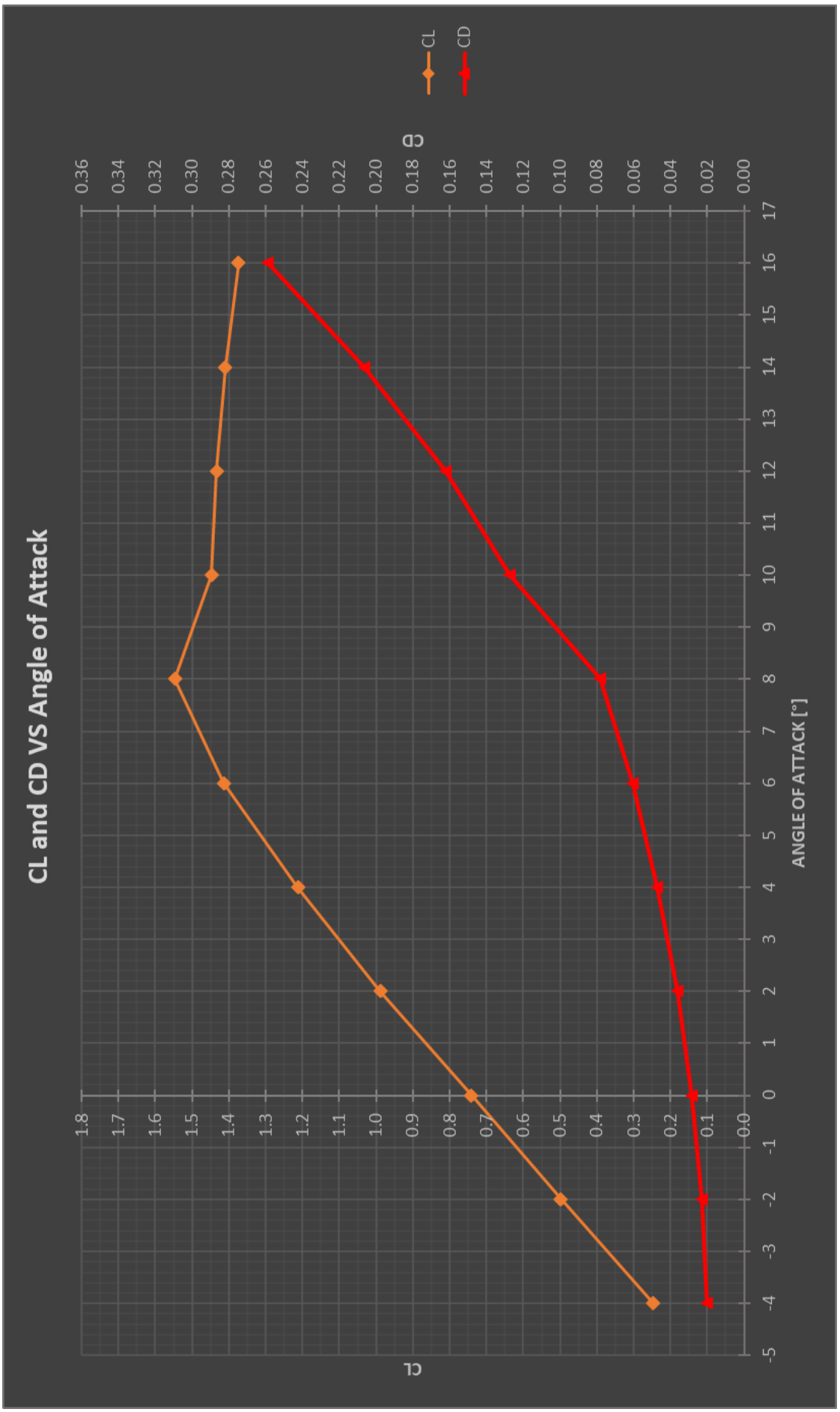

Figure 6-19: Lift and Drag Coefficient Results of Initial UAV CFD

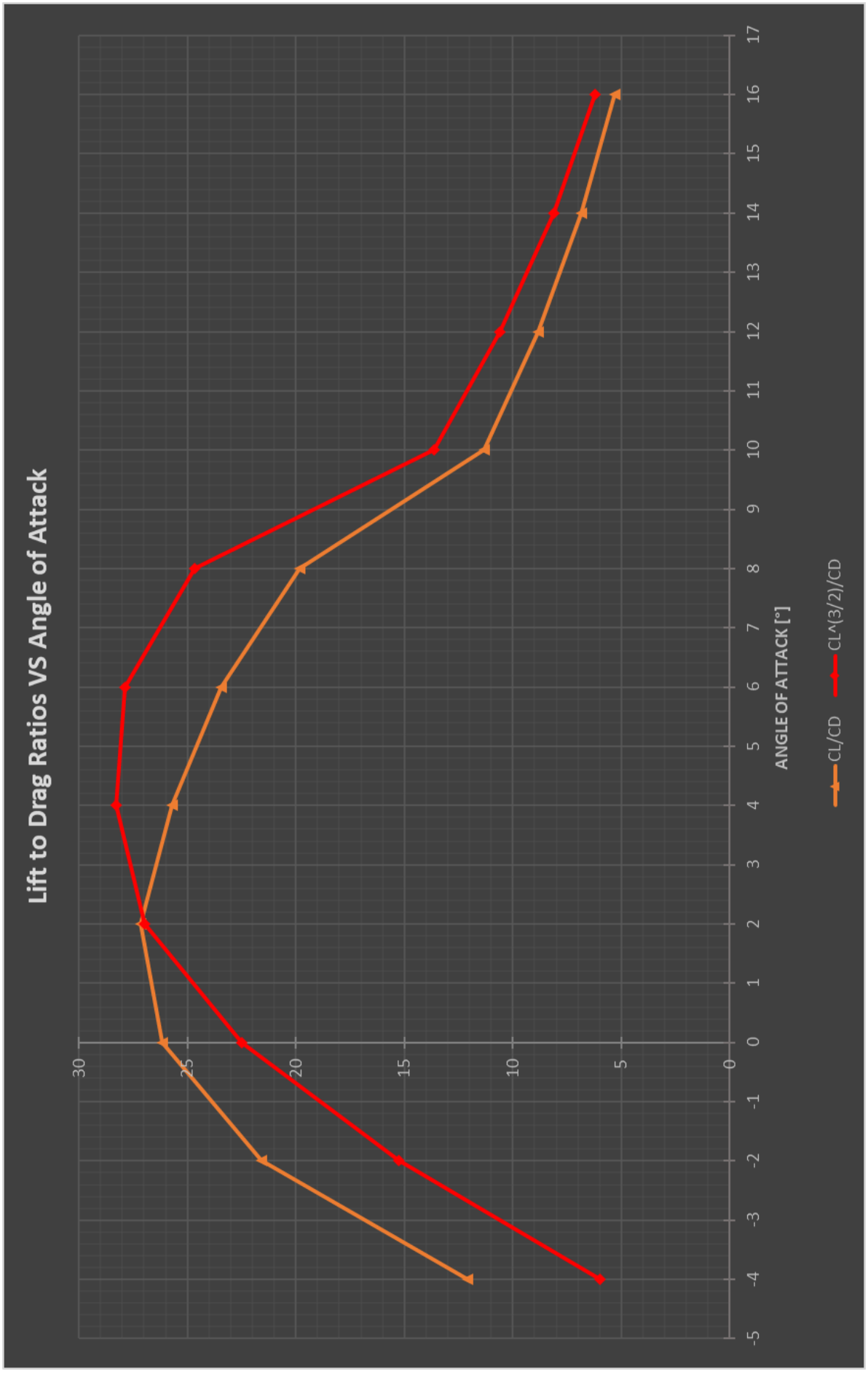

Figure 6-20: Lift and Drag Ratio Results of Initial UAV CFD

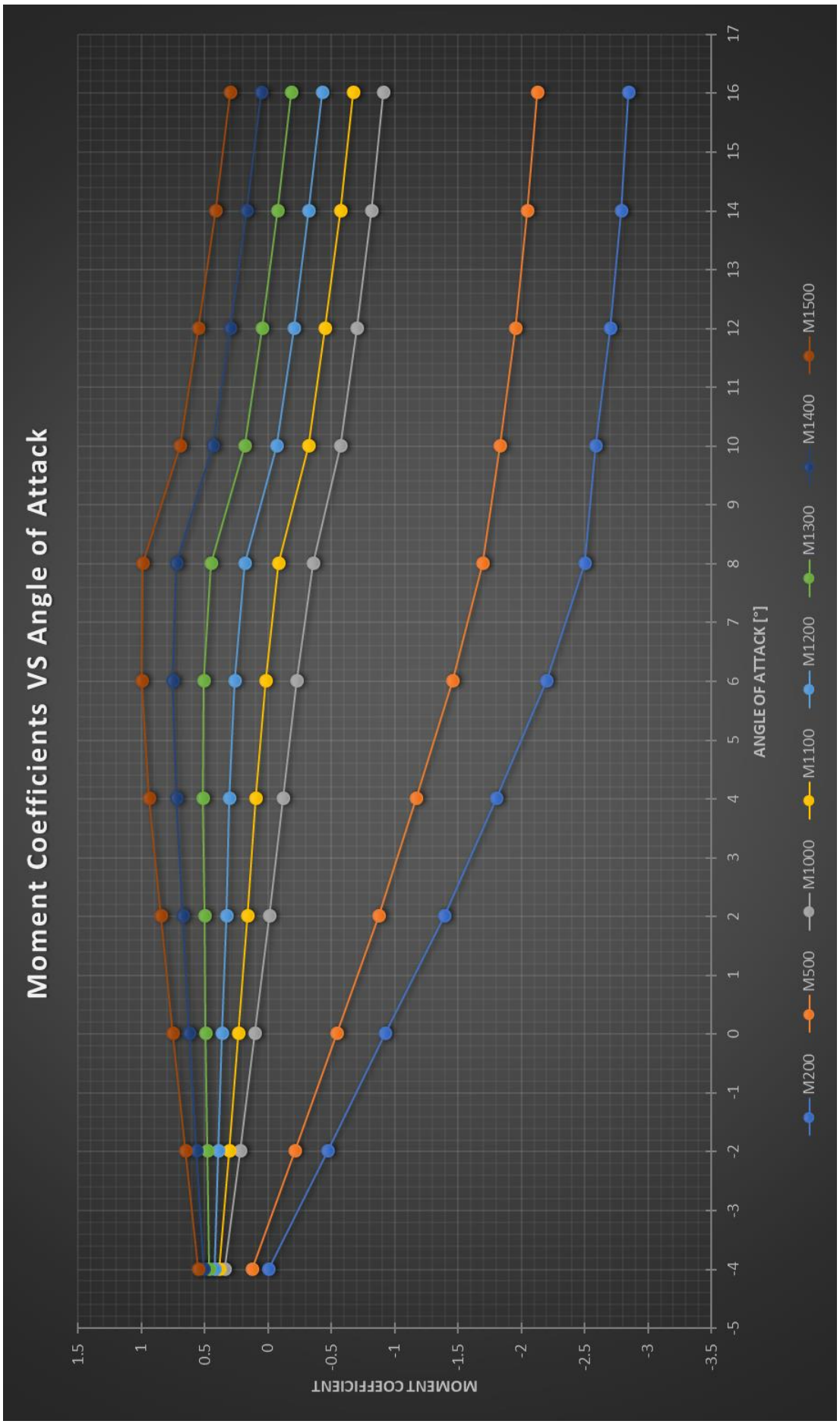

Figure 6-21: Moment Coefficient Results of Initial UAV CFD

As can be seen from Table 6-8, Figure 6-19, Figure 6-20 and Figure 6-21 above, the UAV shows good performance with the initial design. With good lift to drag ratios, which will result in good range and endurance. The aerofoil also shows docile stall behaviour, where this may be a good trait for a pilot occupied aircraft, it is not a necessity for a UAV, nonetheless, it is still advantageous. The aircraft has a relatively low stall angle of approximately 8°. This is due to the high wing setting angle of 6°, as seen in Table 5-3. This high wing setting angle was shown in preliminary calculations to improve the aircraft performance during cruise, and the low aircraft stall angle is not a concern, as this surveillance UAV is not required to perform high AOA manoeuvres. Figure 6-21 also shows the moment coefficients at various lengths along the fuselage. As can be seen, the aircraft is statically stable, with the aircraft neutral point being between 1.3 and 1.4 meters behind the origin of the CAD model (selected as the tip of the nose of the UAV). With the current aerodynamic configuration, efficient, stable, and static flight, can be obtained with a centre of gravity between 1 and 1.2 meters behind the origin in the CAD model (the tip of the nose of the UAV).

Using the values obtained from the CFD analysis above, calculations were done to determine the performance of the UAV and to ensure that the baseline UAV design meets the requirements given in Table 2-1. The calculated values of the requirements that can be confirmed from the CFD are given in Table 6-9 below. A few assumptions had to be made in order to perform the calculations, the assumptions include a propeller efficiency of 75%, a fuel consumption of 600 g/kW hr, and a wing efficiency of 85%. The propeller and wing efficiencies are conservative values obtained from (Sadraey, 2013), and the fuel consumption was determined by taking the lowest fuel consumption of the selected engine and adding 50% to this value. This results in conservative values for the calculations.

The exact calculations, as performed with the values used, are included in APPENDIX C.1.

Table 6-9: Initial UAV Design Calculated Performance

Property	Value	Units	Requirement Met
Endurance	22.8	Hours	Yes
Range	2592	km	Yes
Runway Take-Off Length	550	m	Yes
Stall Speed	27.67	m/s	No
Cruising Speed	40.6 - 35	m/s	Yes
Service Ceiling Rate of Climb	2.75	m/s	Yes
Absolute Ceiling Rate of Climb	1.74	m/s	Yes

As can be seen by the calculated performance in Table 6-9 above, all the requirements, besides that of the stall speed of the aircraft have been met. It is worth mentioning that the calculated stall speed of the aircraft was done using the maximum lift coefficient of the UAV design without any high-lift devices. In the more detailed design stages, the UAV will have at

the very least, a plain flap high lift device which would, in theory, increase the maximum lift coefficient of the UAV by 0.7 to 0.9 or higher (Sadraey, 2013). Assuming an increase of 0.5 in the maximum lift coefficient (bringing the maximum lift coefficient up to 2.0), which is again conservative, the stall speed would in theory drop to 23.96 m/s, which meets the requirement of 25 m/s for the stall speed. The control surfaces and flaps are not the topic of this study and should be the work of future research and more detailed design work. It is believed, using the facts stated above, that adding flaps to the design would enable it to meet the stall speed requirement.

Images of the results from the initial study were also generated in order to gain engineering insight into the design. Firstly, in order to ensure the grid was meeting the requirements for accurate resolution of the boundary layer, the y^+ values were monitored, as can be seen in Figure 6-22 below. The grid met the requirements for y^+ resolution, with more than 99.9% of the cells having a y^+ value of below 1. Figure 6-23 below also shows areas of high vorticity by using ISO clips of vorticity in discrete axial planes along the length of the fuselage. Observed are the areas of high vorticity near the wing tip (wing tip vortex), as well as the area of high vorticity near the wing root junction to the fuselage, showing separation in this location. These are areas for potential aerodynamic improvement.

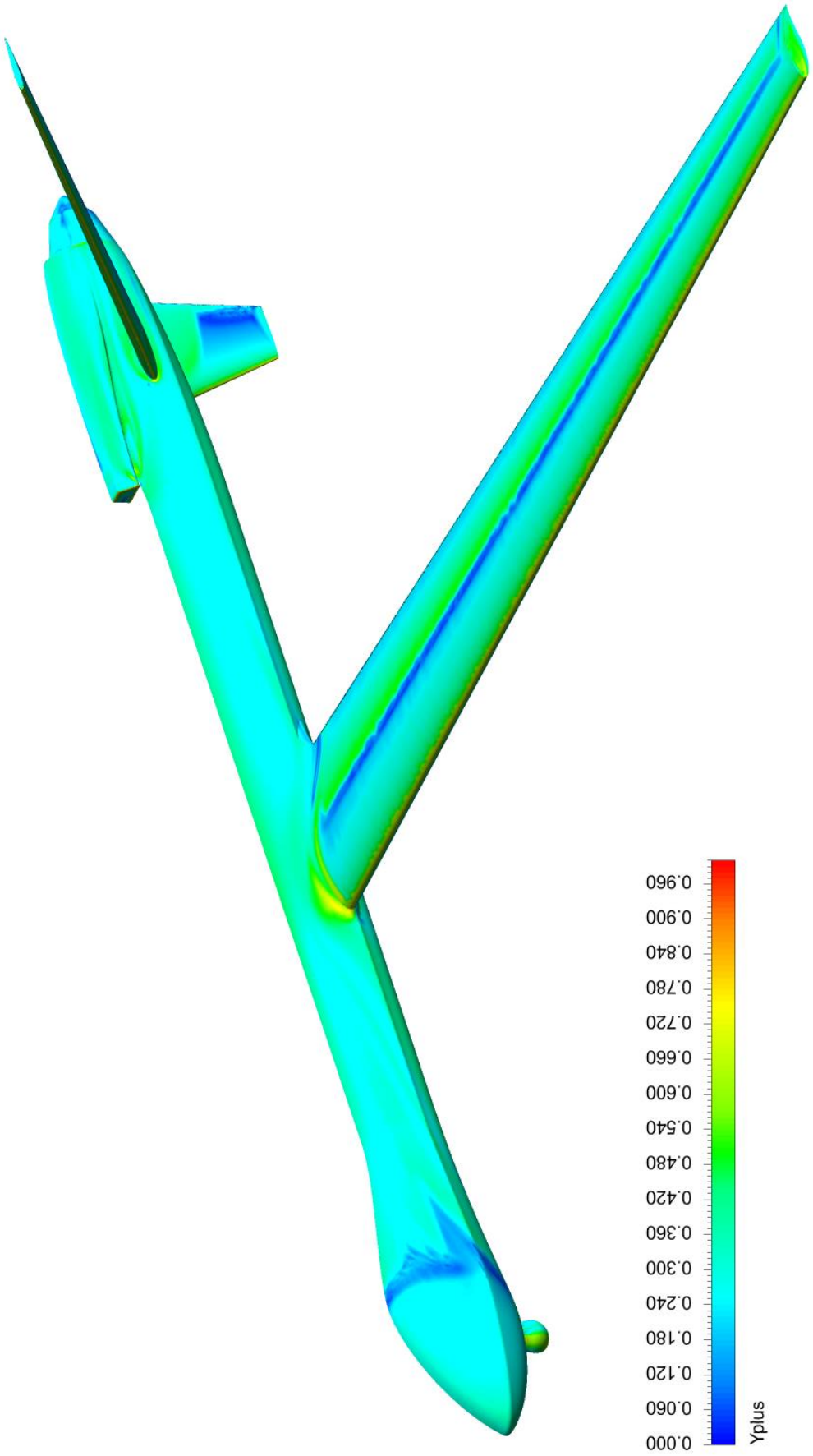

Figure 6-22: Contour Plot of y^+ on Body of UAV at 2° AOA

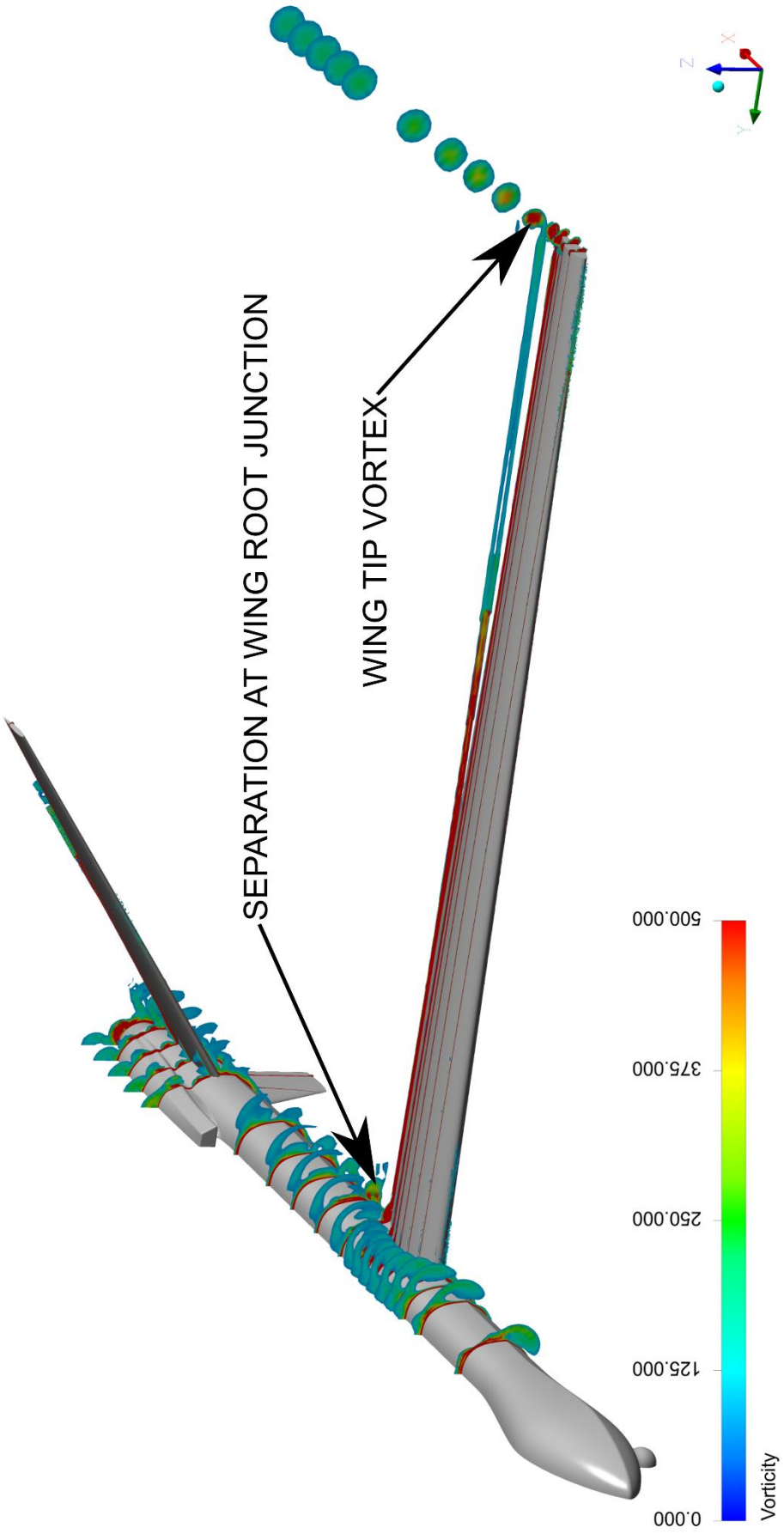

Figure 6-23: ISO Clip showing areas of high Vorticity at Various Planes in the Streamwise Direction at 2° AOA

6.3 Grid Independency Study

A grid independency study was performed at the angle of attack of most interest in order to quantify the change in result variables due to a change in grid size, and to help determine a cell count to aim for in the optimisation CFD studies. The chosen angle of attack was 2°, as this angle of attack will most likely be the nearest to the cruise condition angle of attack. The same setup as the initial CFD study performed was used, with grids of differing sizes. In general, the cell sizes between grids varied by approximately $\sqrt[3]{3}$ in all directions, with minor modifications being made to the boundary layer cells between grid sizes as well. The variables monitored for the grid independency study were the lift and drag coefficients. Five different grids were analysed, with cell counts ranging from approximately 8 million, to 41 million. The results of the grid independency study are shown in Figure 6-24 below.

Figure 6-24 shows that asymptotic convergence is not being reached, however, both the lift and drag values change less than 0.3% after the 34 million cell count, and the results begin to settle there. This accuracy was deemed appropriate for the current study, which involves only the initial design stages. It would have been preferred to carry out another simulation with more cells than the maximum 41 million, just to see the effect on the results, however, available computational resources did not allow for this. The grid selected for the analysis, as well as the optimisation, will be the 34 million cell grid, which displays a good balance between solution accuracy, and computational expense. This cell count is larger than what is typically found in literature, for example, (Bravo-Mosquera, et al., 2017) and (Panagiotou, et al., 2016) use 8 million and 7 million cells respectively. There are a few possible reasons for this discrepancy in cell count. Firstly, the geometry of both of these studies is smaller than what is currently being investigated, requiring fewer cells, secondly, these studies use the Spalart-Allmaras turbulence model, which does not have the same strict grid requirements as that of the Transitional SST (ANSYS INC, 2018), and lastly, both of the studies use far field boundaries much smaller than that of the current study, requiring fewer cells. The validation case performed in section 6.1 showed the importance of the higher cell count, particularly near separation angles of attack. Thus, the higher cell count was deemed necessary when compared to other research. Also observed were the results for drag not monotonically decreasing with increasing cell count, with an increase in drag being present with the 12 million to 22 million cell count results. The exact reason for this is currently unknown but could possibly be attributed to the increased cell count beginning to capture phenomena that the lower cell count was unable to capture, or the boundary layer only beginning to be properly resolved after the 12 million cell count. This could possibly be the topic of future research.

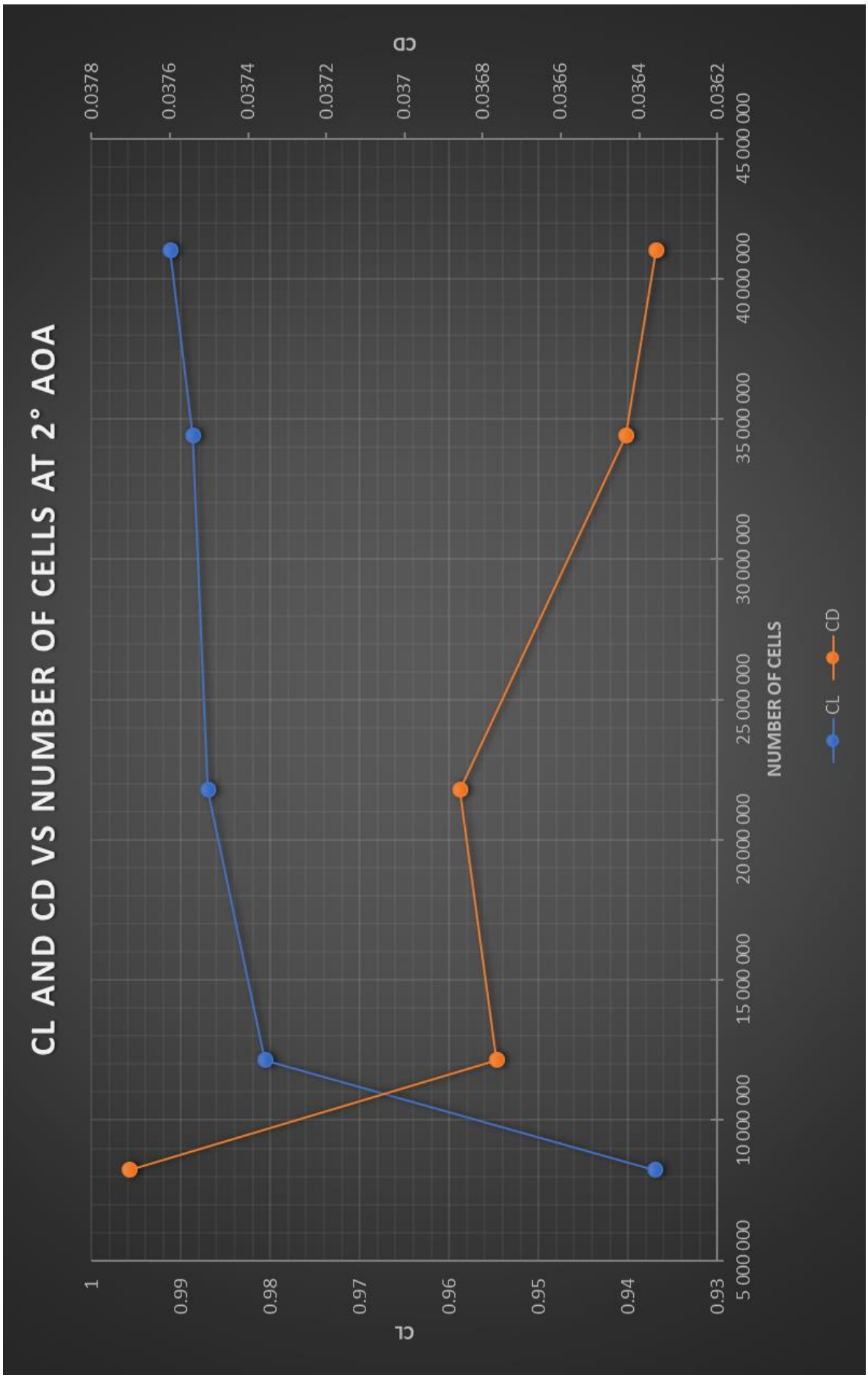

Figure 6-24: Results of the Grid Independency Study Performed at 2° AOA

6.4 Effect of Propeller on Control Surfaces

CPUT has a small UAV design of its own produced by a company known as UAV-SYSCO (Pty) Ltd (Stofberg, 2019). It was noted in an e-mail from Professor Graeme Oliver on the 30th of November 2020 that this UAV struggles with directional control, possibly from the effect the propeller has on the rear stability and control surfaces. The CPUT UAV design shares the pusher configuration, and as such, it was deemed necessary to briefly study the effect a propeller might have on the rear stability surfaces at cruise conditions. The same check will have to be performed once control surfaces are designed, in order to ensure suitable controllability of the UAV. This is out of the scope of the current study and is the topic of future research.

As stated earlier, for initial UAV design, the effects of the propeller are commonly neglected, as is evident by all the papers reviewed in section 1.2, of which only (Kontogiannis & Ekaterinaris, 2013) and (Panagiotou, et al., 2016) include the effects of the propeller on the flow field. Both papers use the momentum source disk method of modelling the effects of the propeller, which simply models a pressure change over an area in the flow field defined as the disk (or propeller) (Panagiotou, et al., 2016). The required pressure jump can be simply modelled by equation (6.1) below. This method is common practice in the earlier design stages and before a formal propeller design is fully realised.

$$\frac{T_{req}}{A_{prop}} = \Delta p_{prop} \tag{6.1}$$

Where T_{req} is the required thrust, A_{prop} is the area of the propeller and Δp_{prop} is the pressure jump over the propeller.

There is literature however, which focuses solely on the effect of the propeller on the flow field of UAVs, such as (Cho, 2014), (Fu, et al., 2012) and (Chen, et al., 2015). In these papers, the design of the UAV itself has already been completed, including detailed design of the propeller, and the propeller is discretely modelled in the CFD solution using a rotating reference frame to include the rotational movement of the propeller. A detailed design of the propeller, and its possible effect on the UAV aerodynamics is out of the scope of this research, and as such the momentum source disk method will be used. The results of the study showed the propeller increasing the drag by 3.2%, with no other adverse effects. This agrees with the results of (Chen, et al., 2015).

6.4.1 Propeller Simulation Setup

Propellers can frequently involve rotational flow, and as in this design, the propeller lies on the centre line of the UAV geometry. If rotational flow on the centre of the geometry is to be considered, the symmetric assumption is no longer valid, and the full UAV must be modelled

and included in the fluid domain (ANSYS INC, 2018). Therefore, a new grid had to be generated without the symmetric assumption. All the same bodies of influence and far-field parameters were used as per the grid generated in 6.2.1, besides the fact that the sizes of the cells had to be increased (thus a slight loss in quality of the solution) because of the larger surface area of the UAV and larger domain volume due to the symmetric assumption no longer being used.

A momentum source disk was also added to the geometry in the form of a planar surface. The momentum source disk was placed in the assumed position of the propeller, along with an assumed size for the propeller. A propeller outer diameter of 1m was assumed, along with a hub diameter of 0.26m. This resulted in a required pressure jump through the momentum source disk of 150 Pa, using the required thrust of approximately 110N, as determined for cruise from the initial analysis in section 6.2 above. Besides the momentum source disk and change in grid due to the symmetric constraint no longer being used, the remainder of the parameters as given in Table 6-5, Table 6-6 and

Table 6-7 above were used. Apart from the reference area from Table 6-5 being doubled, again, because of the full UAV being modelled, and not half using the symmetric assumption. The effect of the propeller was only analysed at assumed cruising conditions, and only one angle of attack of 2°.

6.4.2 Propeller Simulation Results

In terms of the general aerodynamic coefficients, the propeller had little effect, with the lift remaining the same, and the drag increasing by 3.2% with the propeller on under cruising conditions. This result almost exactly matches the results of (Chen, et al., 2015) at cruise conditions, which analyses a similar geometry in much more detail, using a discrete propeller design and a rotating reference frame, and resulted in an increase in drag of 3.4% under cruise conditions. A more detailed analysis of the drag showed that the entire rear fuselage section produced slightly more drag with the propeller on, with the main effect being evident in the pressure drag. This makes sense due to the propeller accelerating the flow velocity towards the rear of the aircraft. In terms of the effectiveness of the stability surfaces (the V-tail and vertical tail), little change was noticed, with the lift force being generated by the V-tail being reduced by 1.48% from 24.411N to 24.05N. The resulting velocity contour plot with the propeller included can be seen in Figure 6-25 below, showing the increase in velocity due to the propeller at the rear section of the fuselage. Figure 6-26 and Figure 6-27 show areas velocity (also known as velocity ISO Clips) between 0 and 32 m/s between the propeller on, and propeller off. A smaller area of the ISO Clip is easily seen in Figure 6-26, particularly as the clips approach the momentum source disk, which shows the increasing flow velocity with the propeller on in comparison to propeller off.

Even though the propeller showed little effect on the stability surfaces of the UAV, care should be taken in the more detailed design stages to ensure the propeller does not interfere with the control surfaces, and when control surfaces are designed in detail, they should be designed with the effects of the propeller in mind. This includes the fact that a pusher propeller configuration adds to the stability of an aircraft, the control surfaces will have to be sized to overcome this addition in stability as well.

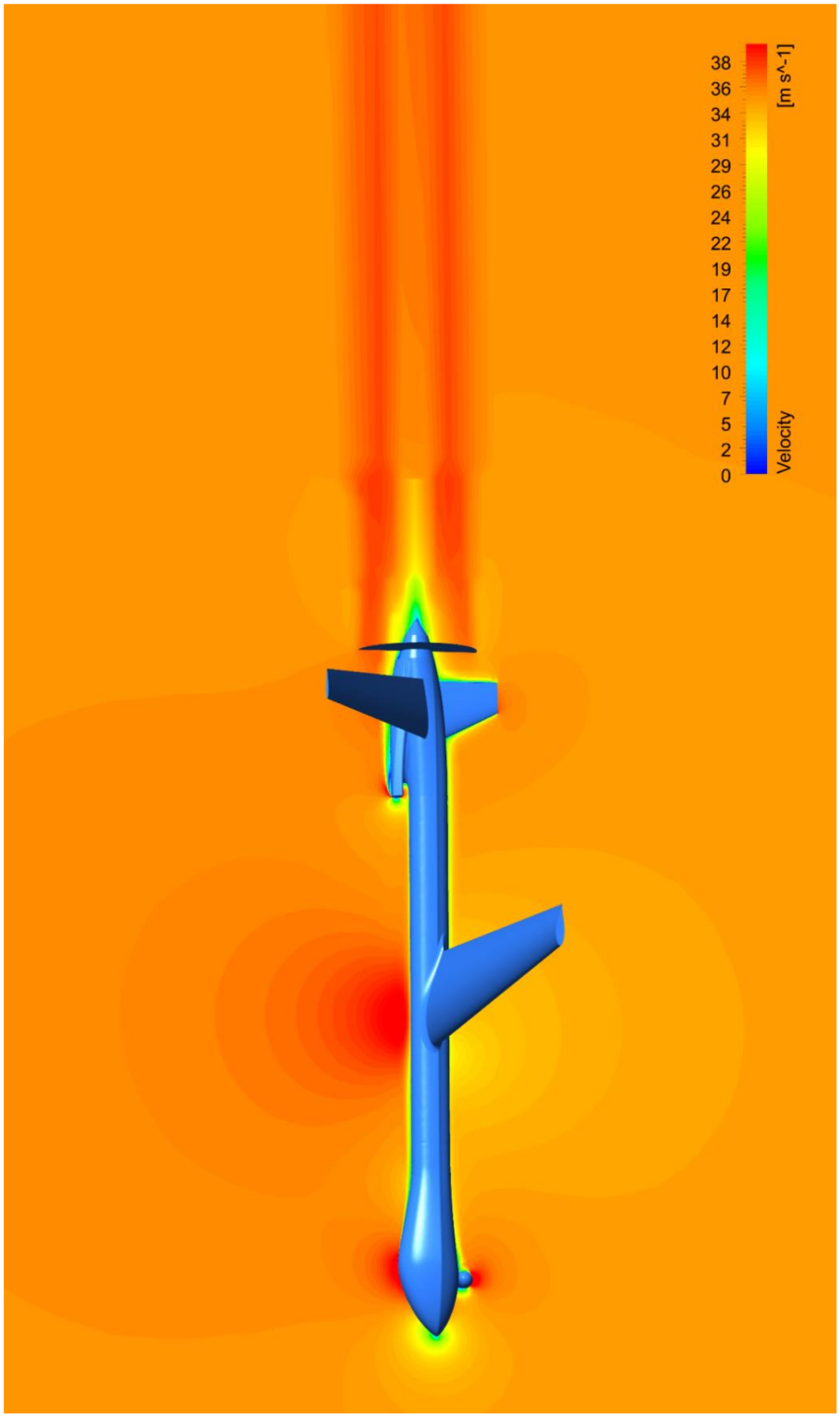

Figure 6-25: Velocity Contour Plot along Centre Line of UAV with Propeller Under Cruise Conditions

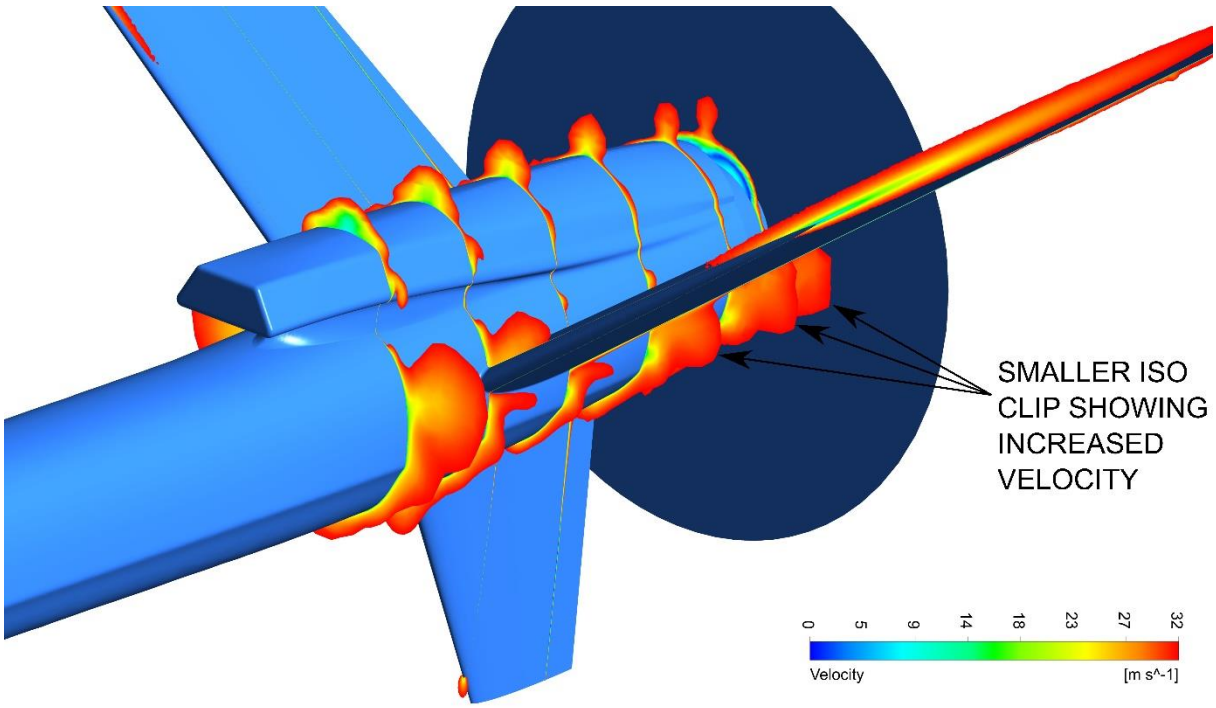

Figure 6-26: ISO Clips of Velocity at Discrete Locations Along Fuselage with Propeller on

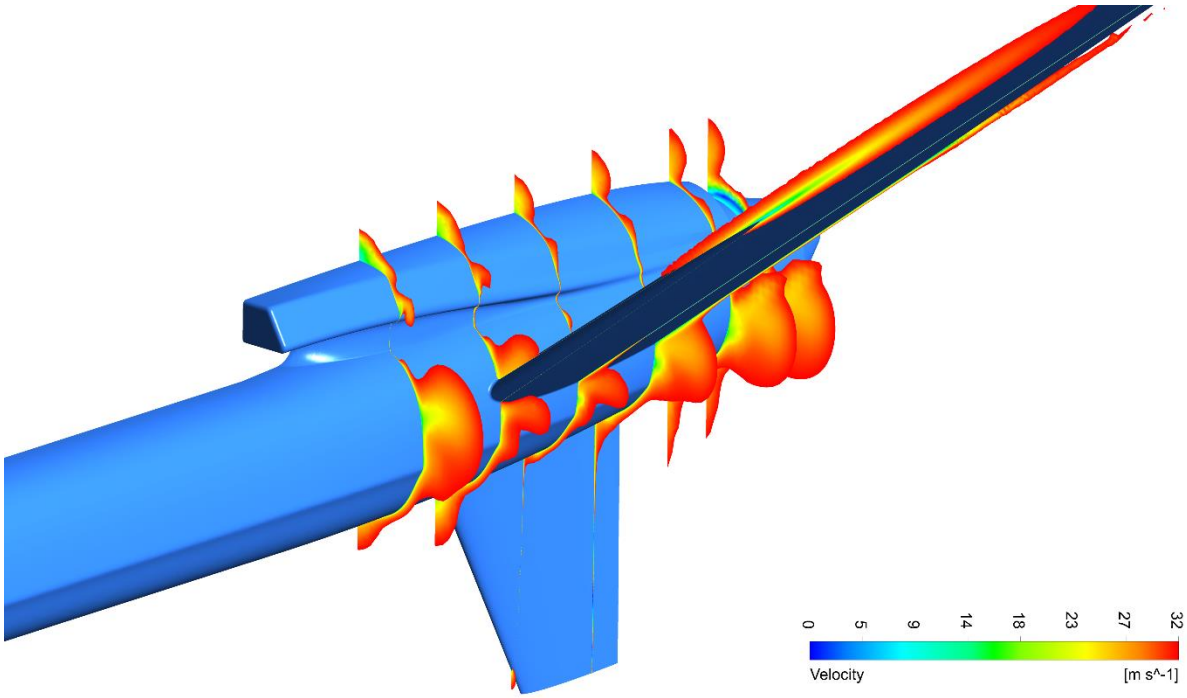

Figure 6-27 ISO Clips of Velocity at Discrete Locations Along Fuselage with Propeller off

CHAPTER 7: Improvement and Optimisation

7.1 Identification of Areas for Improvement

The first step with regards to the optimisation of the aerodynamic design involves that of the identification of areas to be improved. Of course, in order to increase the range and endurance of the UAV, the goals of this optimisation are to increase the C_L/C_D parameter for range, and $C_L^{3/2}/C_D$ parameter for endurance.

During the analysis of the initial UAV design as seen in section 6.2, the Transitional SST turbulence model was used. However, a small study was done to evaluate the difference between turbulence models. This study involved repeating the analysis of the initial design at 2° AOA using the Spalart-Allmaras turbulence model instead of the Transitional SST. The differences in the results between these models were more substantial than originally anticipated and provided valuable insight into the possible areas of improvement in the design. In comparing the results, it was noticed that the lift and pressure drag results between the turbulence models were within 1.5% of each other. The viscous drag on the other hand was approximately 42% higher when using the Spalart-Allmaras model, as opposed to the Transitional SST model. This is due to the Spalart-Allmaras model assuming a fully turbulent boundary layer across the entire UAV wall geometry, and not taking laminar zones into account, as the Transition SST model does. This difference between the models makes a large difference in the results of the viscous drag calculation at the Reynolds numbers typically seen by the UAV (Chen, et al., 2020) (Swart, 2020). The differences between the results of the two turbulence models for the drag results are shown quantitatively in Figure 7-1, where the similarity between the pressure drag, and large difference between viscous drag can be seen. Figure 7-2 below also shows the difference between the skin friction (viscous) drag results. It is immediately noticeable where the Spalart-Allmaras model shows a large area of high values for skin friction coefficient on the wing leading edge, whereas by comparison, the Transition SST model calculates this area as laminar, which results in comparatively lower skin friction coefficient values. The same difference can be seen in the horizontal tail. Figure 7-2 shows another difference in the results between the turbulence models in the wing root fillet area. The flow separation is clearly visible in the Transitional SST model results but is not present in the Spalart-Allmaras results. It is well known that increased levels of turbulence can delay flow separation (Anderson, 2011), thus, it is believed that the Spalart-Allmaras model is overpredicting the levels of turbulence at the Reynolds numbers present in this analysis, and is therefore delaying, or completely preventing, separation in the wing root fillet. The separation in the wing root fillet area is increasing the drag of the UAV, and an attempt should be made to eliminate this for the optimised design.

In terms of design improvement, what this shows is that the drag can be greatly reduced by extending the laminar zone over the wing (and tail, if applicable). An aerofoil series known as Natural Laminar Flow (NLF) aerofoils have been in use for decades to reduce the drag on gliders and sailplanes (Gopalarathnam & Selig, 2001). Incorporating one of these aerofoils into the wing design, and extending the laminar flow over the wing, could greatly reduce the drag.

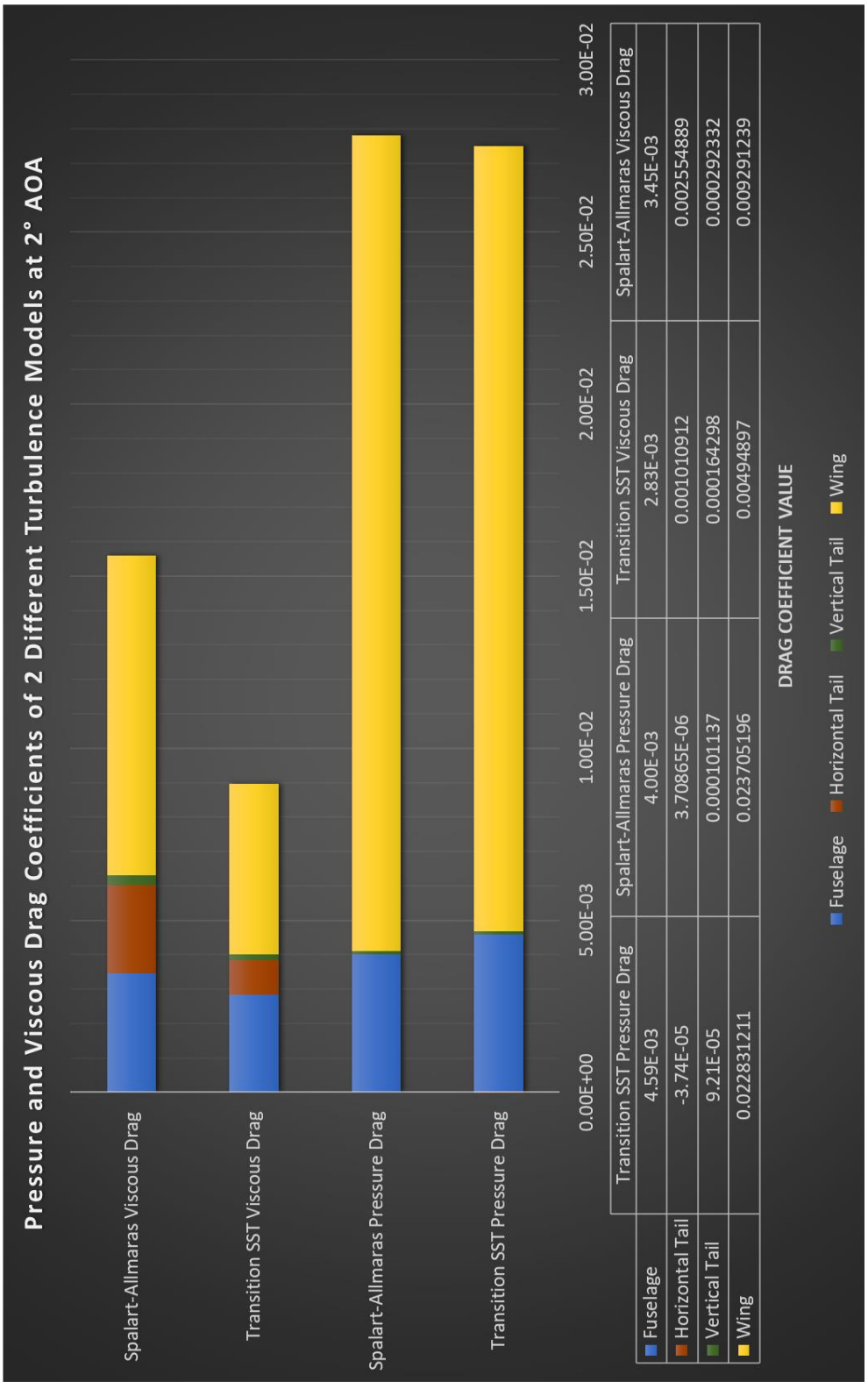

	Transition SST Pressure Drag	Spalart-Allmaras Pressure Drag	Transition SST Viscous Drag	Spalart-Allmaras Viscous Drag
Fuselage	4.59E-03	4.00E-03	2.83E-03	3.45E-03
Horizontal Tail	-3.74E-05	3.70865E-06	0.001010912	0.002554889
Vertical Tail	9.21E-05	0.000101137	0.000164298	0.000292332
Wing	0.022831211	0.023705196	0.00494897	0.009291239

Figure 7-1: Pressure and Viscous Drag Coefficient Comparison of Transitional SST and Spalart-Allmaras Models at 2° AOA of Initial UAV Design

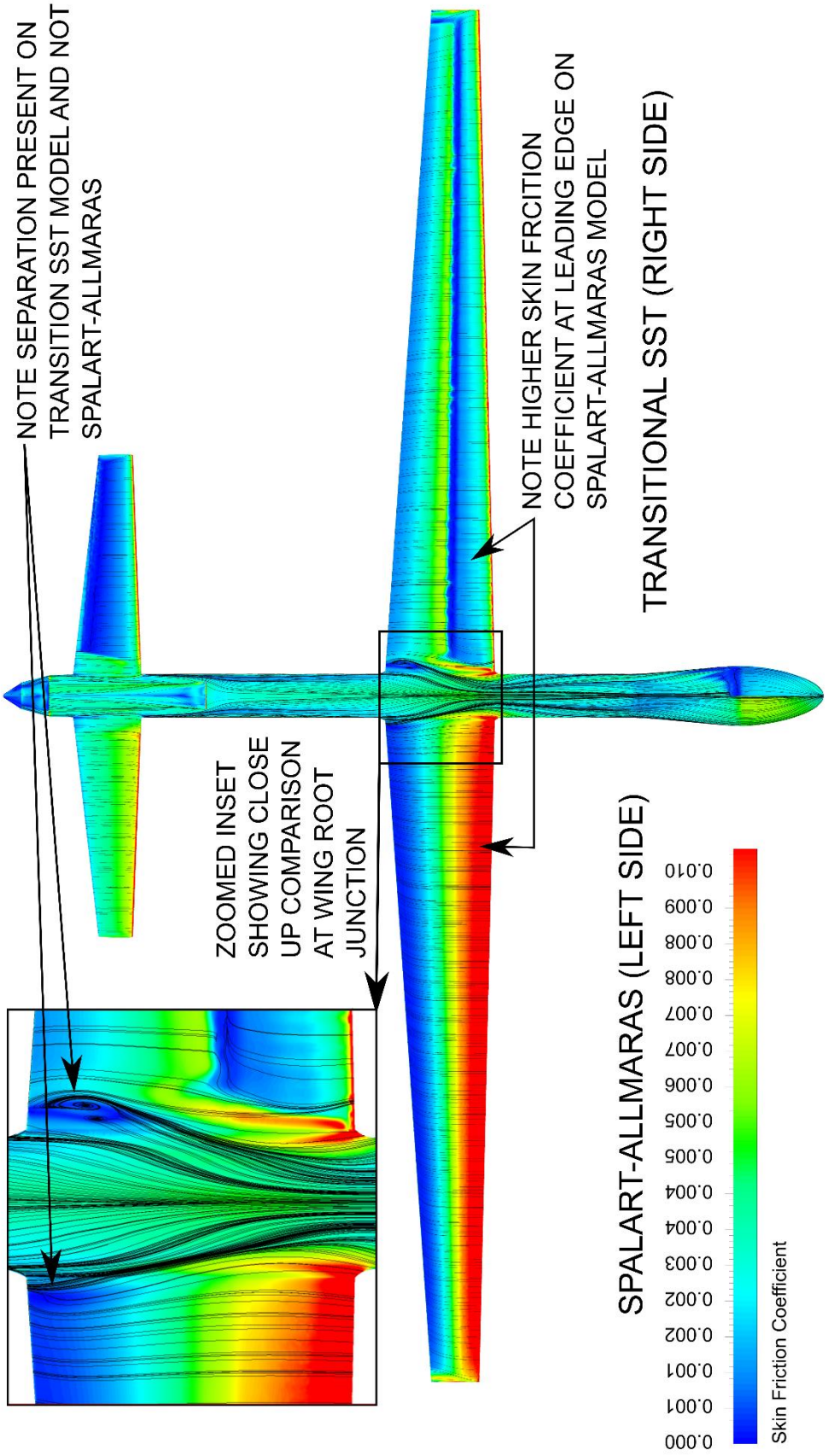

Figure 7-2: Side by Side Top View of the Skin Friction Coefficient and Surface Streamlines of Spalart-Allmaras (Left) and Transition SST (Right) Turbulence Models at 2° AOA

The CFD study of the initial design also showed large vortices forming off the wingtips, as was shown in Figure 6-23. These vortices are known to decrease aerodynamic efficiency (Anderson, 2011), and a method of negating this reduction is to incorporate a winglet on the tip of the wing, as shown in the studies performed by (Kontogiannis & Ekaterinaris, 2013) and (Gautham & Bibin, 2016). The increase in the overall aerodynamic efficiency of the wing improves cruise performance by improving lift efficiency and reducing drag (Weierman, 2010), (Maughmer, n.d.). Since the improvement of computational and design methods for aerodynamics, several UAVs and sailplanes have incorporated wing tip devices such as winglets in order to make use of these benefits (Maughmer, n.d.) (Weierman, 2010). (NASA Dryden Flight Research Center, n.d.) states that winglets can improve the range of aircraft by up to 7%, depending on aircraft size and configuration, therefore, the decision was made to increase aerodynamic performance by adding a winglet. The information from the references already mentioned above were used in order to design the winglet, along with a trial-and-error approach by the author, using wing only CFD analysis to compare the results of different winglet configurations.

7.2 Improved Design using Outcomes from Initial CFD Study

After several further design iterations in both xflr5, as well as wing only CFD analysis (excluding the fuselage), an improved UAV design incorporating the performance improvements listed above was realised. The updated design features a NLF1015 aerofoil profile for the wing, instead of the previously used NACA 63(4)-421 profile. The planform of the wing remained the same. Where the NLF aerofoil profile lacks the thickness of the NACA, reducing the available volume in the wing and the opportunity for extra structural rigidity through the wing, the aerodynamic benefit more than makes up for this. A winglet design was also incorporated into the new design, which improved the aerodynamic efficiency of the wing and increased the lift coefficient of the wing at cruise conditions. The rear of the aircraft, including both the horizontal, and the vertical tail designs remained the same, as they performed their function as desired, and not much room was seen for improvement. It should also be noted that, with the improved design, fuel, landing gear, and certain engine systems had to be redistributed which resulted in a shift in the COG. The location of the wing shifted back approximately 450mm on the improved design to account for this shift in the COG, and to retain static stability. The updated UAV design can be seen in Figure 7-3 below.

Table 7-1: Lift and Drag Results of Improved UAV Design

AOA [°]	Lift Coefficient	Drag Coefficient	C_L/C_D	$C_L^{3/2} / C_D$
2	1.166	0.040427	28.842	31.14414

Table 7-1 above shows the results of the CFD analysis at 2° AOA of the improved UAV design. A performance increase over the values reported from the initial design in Table 6-8 of 15.2% can be seen for the lift, where the drag increased in the improved design by 9.87%. This increase in drag is most likely lift induced drag due to the higher lift coefficient at 2° AOA. Even with this increase in drag, the C_L/C_D and $C_L^{3/2}/C_D$ parameters improved by 5.9% and 13.37% over the initial design respectively.

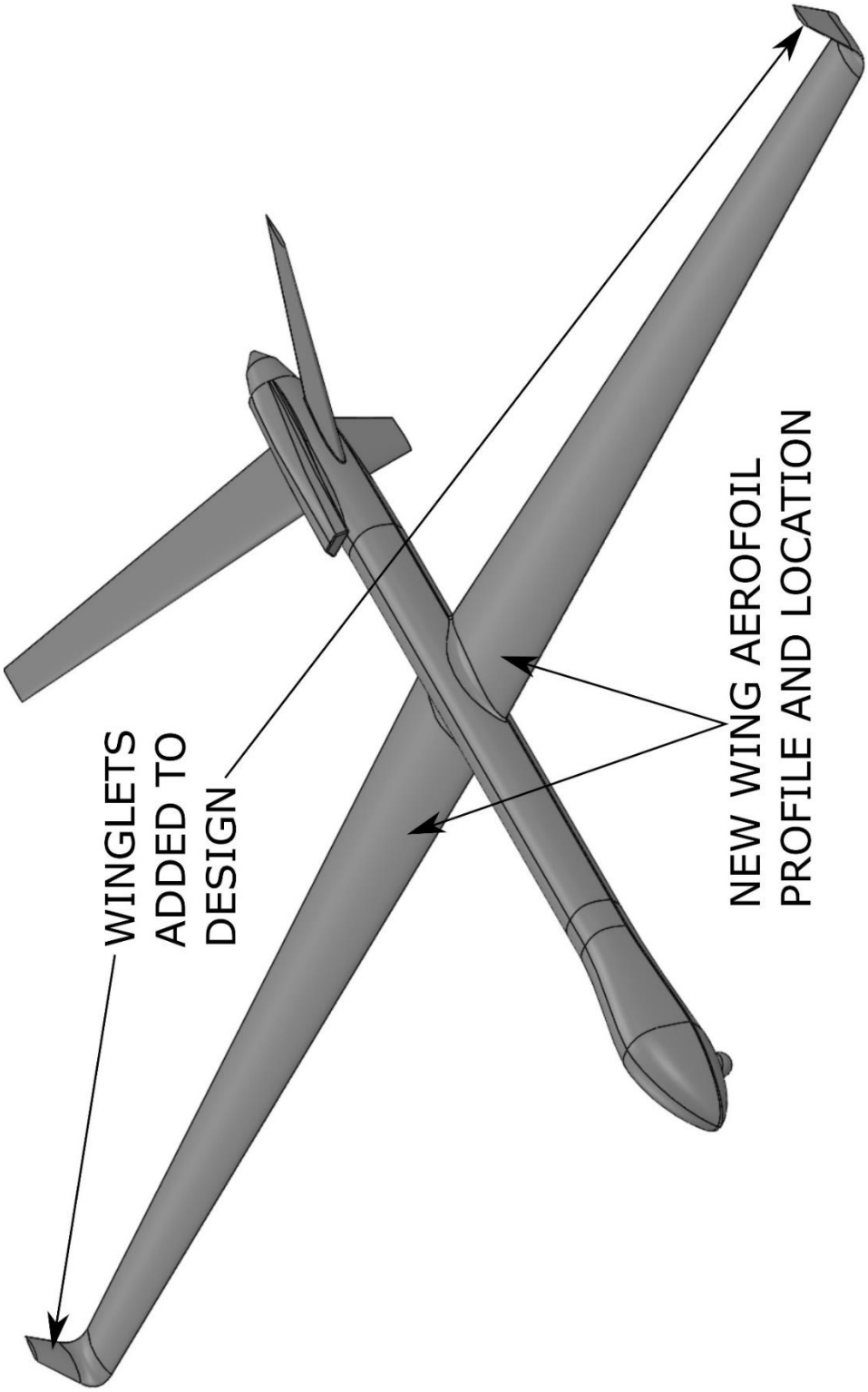

Figure 7-3: Isometric View of Improved UAV Design

Images of the results of the analysis, and comparisons to the results of the initial UAV design are also given in Figure 7-4, Figure 7-5 and Figure 7-6 below. In Figure 7-4, the extension of the laminar zone in the improved design can be clearly seen by the skin friction coefficient, showing lower values to the initial design over a much larger area of the wing. The transition from laminar to turbulent flow occurs at approximately 30-40% of the chord at the wing root in the initial design, and at approximately 60-70% in the improved design. This extension of the laminar zone reduced the viscous drag of the wing in the improved design. The wing root sections can be seen more clearly in Figure 7-5, which is merely Figure 7-4 zoomed in to the wing root fillet zone. What Figure 7-5 is trying to emphasize is the wing root fillet separation, present on both the initial and improved designs. Of course, the new wing aerofoil profile resulted in a different wing root fillet, and even with the increase in performance of the new aerofoil profile, Figure 7-5 shows the wing root fillet separation has worsened. This area should be looked at in more detail for future iterations and aerodynamic updates and is the possible topic of future work. This worsening of the separation is also clearly present in Figure 7-6, where the vortex strength at the wing root can also be seen to be stronger.

Figure 7-6 below also shows a comparison of the wing tip vortices by using ISO clipped surfaces on several discrete planes of the vorticity magnitude, between the initial UAV design and the improved UAV design. What is important to remember in this figure is that the wing of the improved design was shifted backwards by 450mm. Even with this shift, and the surfaces being taken at the same locations from the nose between the two designs, the magnitude of the wing tip vortex of the improved UAV design is observed to be weaker than that of the initial UAV design, thus improving the aerodynamic efficiency of the wing.

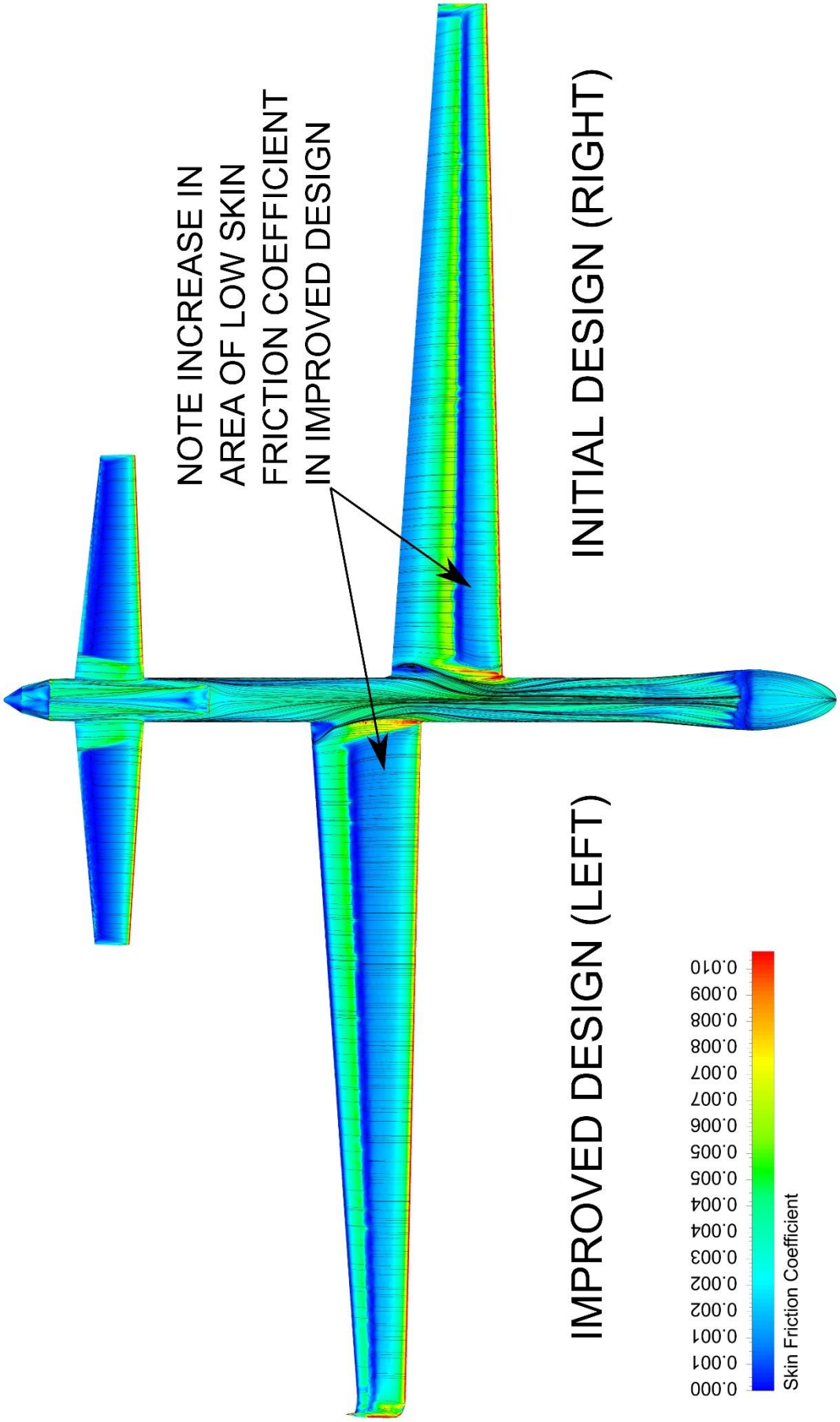

Figure 7-4: Side by Side Top View of the Skin Friction Coefficient and Surface Streamlines of Initial (Right) and Improved (Left) UAV Designs at 2° AOA

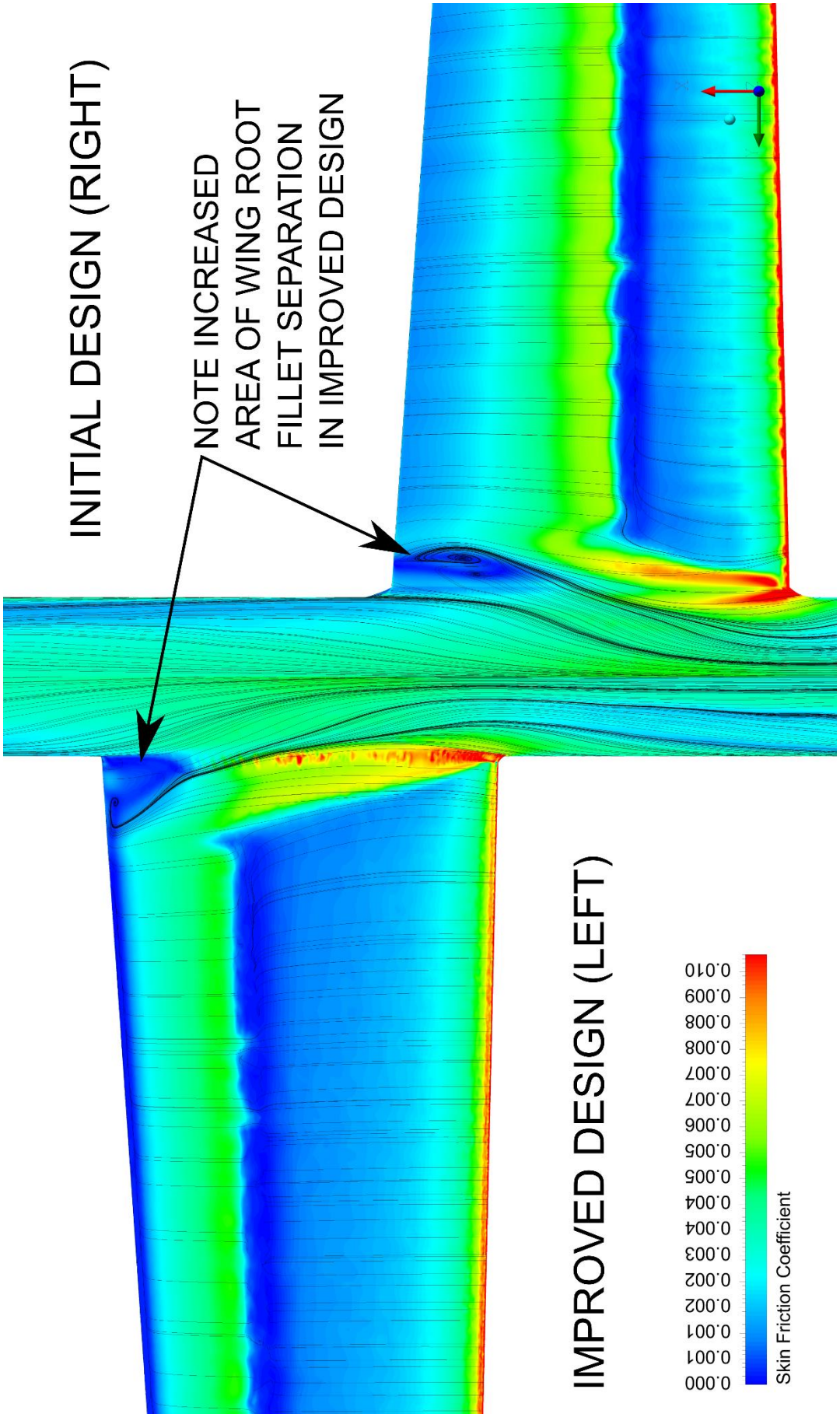

Figure 7-5: Side by Side Zoomed into Wing Root Fillets Top View of the Skin Friction Coefficient and Surface Streamlines of Initial (Right) and Improved (Left) UAV Designs at 2° AOA

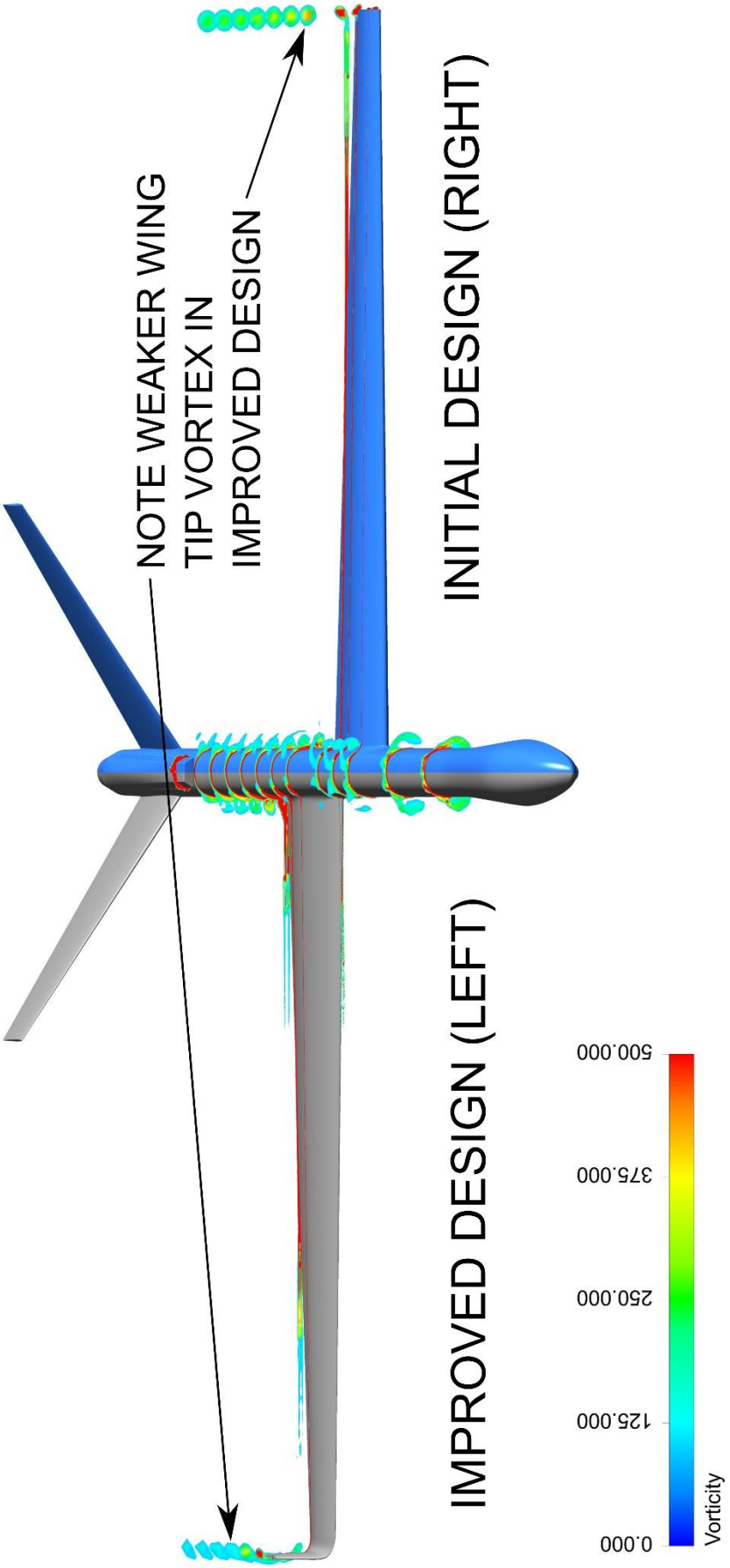

Figure 7-6: Side by Side ISO Clipping of Vorticity Magnitude on Discrete Planes of Initial (Right) and Improved (Left) UAV Designs at 2° AOA

7.3 Adjoint Optimisation

7.3.1 Adjoint Optimisation Introduction

There are many possible methods of optimisation existing in literature, with the most popular being gradient based optimisation, which can handle many design variables at once (Tzanakis, 2014). Finite difference, and the adjoint method are both methods capable of performing numerical gradient optimisation in conjunction with fluid flow simulations (Tzanakis, 2014). For complex problems, the adjoint solver has the distinct advantage of only a single computation for the calculation of sensitivities of a function in relation to several design variables (Tzanakis, 2014). This goes in contrast to the finite difference method, which requires an iterative process, performing a calculation of the desired objective of each design variable change (Tzanakis, 2014). This makes adjoint optimisation a powerful tool, capable of quickly optimising complex shapes with many variables. This is evident by the use of adjoint optimisations use in several papers for aerodynamics and CFD optimisation, including, but not limited to (Chen, et al., 2020), (Swart, 2020), (Giles & Pierce, 2000), (Reuther, et al., 1999), (Reuther, et al., 1999) and (Tzanakis, 2014). It is worth noting here that one drawback of gradient based optimisation with the adjoint method, is that it is only capable of obtaining the local minimum or maximum (which may coincide with the global minimum or maximum, or may not), and it is not capable of finding solutions where discontinuities exist (Giles & Pierce, 2000).

Two methods of adjoint optimisation exist in order to solve for the local minimum or maximum, namely, the continuous method and the discrete method, both methods are available in ANSYS Fluent (ANSYS INC, 2018). The continuous method explicitly formulates the adjoint partial differential equation set, and mathematically derives the adjoint boundary conditions. The discrete method however calculates the adjoint sensitivity using discretised equations. The difference between these two methods is shown graphically in Figure 7-7 below, as adapted from (Tzanakis, 2014).

According to (ANSYS INC, 2018), the continuous method has the advantage over the discrete method in that it is decoupled from the original flow solver. Where this may seem like a large benefit, with most practical problems involving complex geometries and turbulence models with wall functions, it can produce inconsistencies depending on the modelling, discretisation and solution approaches used. Thus, (ANSYS INC, 2018) strongly recommends the use of the discrete adjoint solver, and this will be the solver used for the purposes of this study.

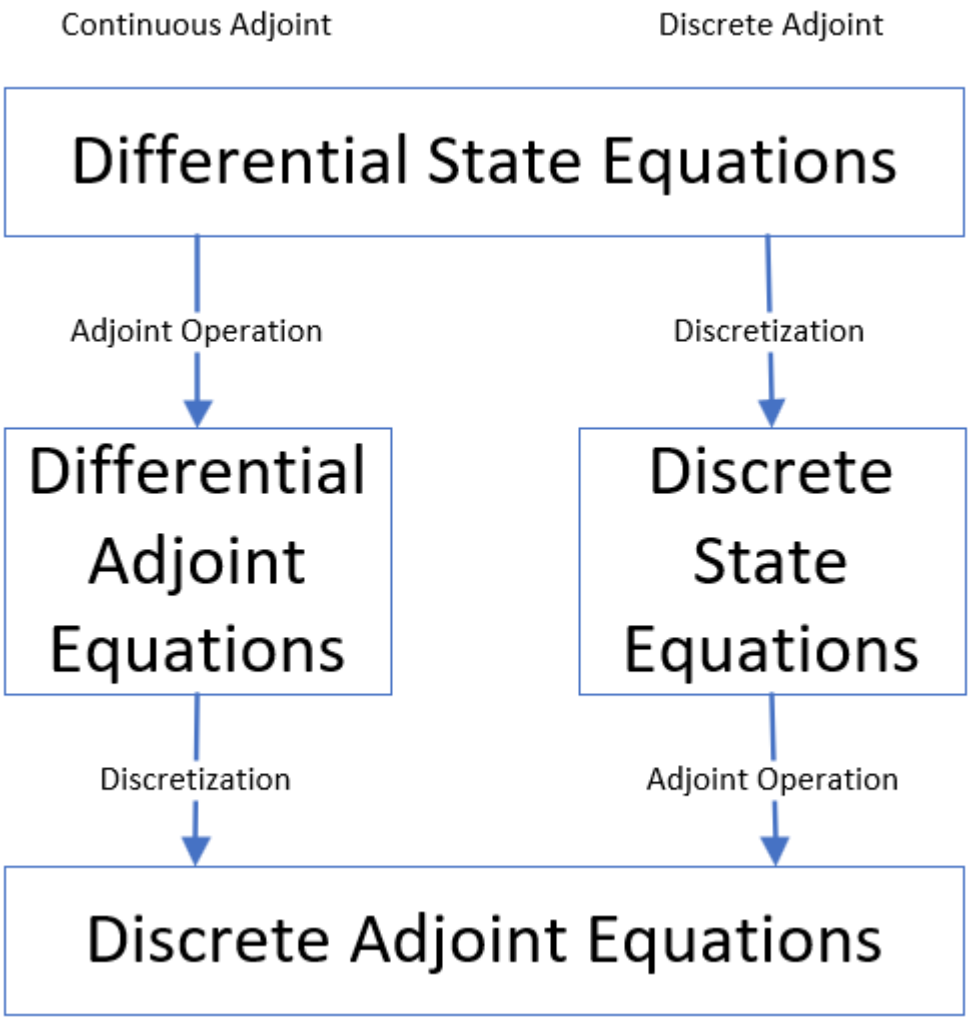

Figure 7-7: Graphical Representation of Difference Between Continuous and Discrete Adjoint Methods

7.3.2 Adjoint Optimiser Theory

The discrete adjoint solver in ANSYS Fluent provides extra information over and above a normal solver by providing data that allows the user to view and analyse the sensitivity of various parameters to the performance of a given solution (ANSYS INC, 2018). In other words, the Adjoint Solver provides information as to what changes in boundary conditions will provide a particular effect on the solution. This is a powerful tool which, for an analysis involving complex geometry, such as which is currently being undertaken, can be used to improve the performance by increasing lift or decreasing drag.

The topic of an Adjoint Solver optimisation can be a paper in its own right and as such, the theory will only be briefly covered, before proceeding with the adjoint optimisation of the current study.

The ANSYS Fluent discrete adjoint solver makes use of the discretised equations already existing in the flow solver (ANSYS INC, 2018). This type of adjoint solver computes the derivative of the parameter of interest, such as drag, with respect to the user-specified

parameters, while eliminating any changes that may arise in the flow variables themselves. The goal of the adjoint solution is to determine the sensitivity of the parameter with respect to the user specified variables and boundary conditions. This is accomplished by using the equations below, as shown by (ANSYS INC, 2018).

At convergence, the flow variables are required to satisfy equation (7.1) below.

$$\boldsymbol{\mathcal{R}}_i^{\mu}\left(\underline{q}^0, \underline{q}^1, \dots, \underline{q}^{M-1}; \underline{c}\right) = 0, \mu = 0, \dots, M-1, i = 0, \dots, L-1 \tag{7.1}$$

Where $\underline{c}$ denotes the vector of a value that the user sets that may affect the solution and $\underline{q}^v$ is the vector of the variable in the v^{th} cell, M is the number of cells in the problem and there are L conditions on each cell.

The scalar of interest, $\boldsymbol{\mathcal{J}}$, that is dependant of the flow state and possibly directly on the control variables, can be denoted by equation (7.2) below.

$$\boldsymbol{\mathcal{J}}\left(\underline{q}^0, \underline{q}^1, \dots, \underline{q}^{M-1}; \underline{c}\right) \tag{7.2}$$

The purpose of the discrete adjoint solver is to determine the sensitivity of the observation with respect to a control variable specified by the user. If the solution is varied by δc_j, then the linearization of the governing equation (equation (7.1) above) shows that the variation in the flow δq_j^v must satisfy equation (7.3) below.

$$\frac{\partial R_i^u}{\partial q_j^v}\delta q_j^v = -\frac{\partial R_i^u}{\partial c_j}\bigg|_q \delta c_j, \mu = 0, \dots, M-1, i = 0, \dots, L-1 \tag{7.3}$$

Equation (7.3) above implies summation over j and v, while $\Big|_q$ shows that the flow solution is held constant while the derivative is taken.

If the control variables and the flow state change, then the observation will change according to equation (7.4) below.

$$\delta\boldsymbol{\mathcal{J}} = \frac{\partial \boldsymbol{\mathcal{J}}}{\partial q_j^v}\delta q_j^v + \frac{\partial \boldsymbol{\mathcal{J}}}{\partial c_j}\bigg|_q \delta c_j \tag{7.4}$$

An explicit relationship between the changes in the control variables, and how they affect the observation of interest is accomplished by taking the weighted linear combination of the linearized governing equation, namely, equation (7.3) in a particular manner. Namely, a set of adjoint variables $\underline{\tilde{q}^{\mu}}$ are introduced into the equation, with a one-to-one correspondence with the governing equations, which results in the relations shown in equation (7.5) below.

$$\left[\tilde{q}_i^{\mu}\frac{\partial R_i^u}{\partial q_j^v}\right]\delta q_j^v = -\tilde{q}_i^{\mu}\frac{\partial R_i^u}{\partial c_j}\bigg|_q \delta c_j \tag{7.5}$$

In equation (7.5) above, the term in the brackets on the left is then matched to the coefficient for the variation of the flow in equation (7.4), which then defines the values for the adjoint variables as equation (7.6) below.

$$\frac{\partial R_i^u}{\partial q_j^v}\tilde{q}_i^{\mu} = \frac{\partial \boldsymbol{\mathcal{J}}}{\partial q_j^v} \tag{7.6}$$

Equations (7.1) to (7.6) above give a brief description of the discrete adjoint solver equations. The solution of these equations is the main goal of the adjoint solver.

Worthy of note are the facts that the discrete adjoint equations depend on the original state of flow (namely, the initial solution from which the adjoint solution is computed), as well as the specific physics that are employed in the solution. The adjoint solver in ANSYS Fluent, only supports the laminar, or fully turbulent $k-\omega$ and $k-\varepsilon$ turbulence models (ANSYS INC, 2018).

The adjoint solution above merely shows the sensitivity of a variable to changes in the boundary conditions of a solution. This sensitivity can be useful to determine where a small shift in a boundary, e.g. an external wall of a UAV, can have the largest effect. ANSYS Fluent offers tools to automatically morph the mesh in these sensitive zones in order to provide a goal defined by the user, such as a targeted increase in lift, or reduction in drag. Firstly, the sensitivity of the cost is determined in respect to the shape by equation (7.7) below.

$$\delta\boldsymbol{\mathcal{J}} = \frac{\partial \boldsymbol{\mathcal{J}}}{\partial x_j^n}\delta x_j^n \tag{7.7}$$

Where x_j^n is the j^{th} coordinate of the n^{th} node in the mesh. And where x_j^n denotes the subset of the control variable c_j in a system that corresponds to mesh node positions. The adjustment is then given by equation (7.8) below. Which will provide the maximum adjustment $\boldsymbol{\mathcal{J}}$ for a given L^2 normal of ∂x_j^n, and where λ shows an arbitrary scaling factor. The selection of the sign of λ is used to increase or decrease $\boldsymbol{\mathcal{J}}$.

$$\delta x_j^n = \lambda\frac{\partial \boldsymbol{\mathcal{J}}}{\partial x_j^n} \tag{7.8}$$

The change is then estimated in first order as equation (7.9) below.

$$\delta\boldsymbol{\mathcal{J}} = \lambda\frac{\partial \boldsymbol{\mathcal{J}}}{\partial x_j^n}\frac{\partial \boldsymbol{\mathcal{J}}}{\partial x_j^n} \tag{7.9}$$

Fluent then offers two approaches to the mesh morphing and smoothing, which both give different results, namely, the Polynomials-Based Approach, and the Direct Interpolation Method (ANSYS INC, 2018). The Direct Interpolation Method offers a few advantages over the Polynomials-Based approach, including faster convergence, better handling of design conditions and a simpler setup. The Direct Interpolation Method also has limitations, including the possibility of the morphed mesh not being of the same quality as that produced by the Polynomials-Based Approach, but the faster convergence and better handling of design conditions was deemed a better choice for the mesh morphing and smoothing, and as such, was selected as the mesh morpher for this study. The Direct Interpolation Method displaced the mesh as a weighted average of all the boundary node displacements as per equation (7.10) below. Equation (7.10) is presented as the two-dimensional version of the equation for simplicity and can be extended into 3 dimensions if required.

$$\Delta x_v^i = \frac{\sum_{j=0}^{N_b} w_j(r_{ij}) \Delta x_b^j}{\sum_{j=0}^{N_b} w_j(r_{ij})} \tag{7.10}$$

Where x_v^i and x_b^j are the interior and boundary node displacements respectively, r_{ij} is the distance between the i^{th} and j^{th} nodes and w_j is the weighting function.

7.3.3 Solution Setup for Adjoint Optimisation

Due to the inherent complexity of solving an adjoint solution, as well as the computational resource requirements, and the limitations of the wall boundary conditions available to solve an adjoint solution, several compromises had to be made for the purposes of this study.

Firstly, the simulations carried out on both the initial, as well as the improved UAV designs, used the Transition SST turbulence model, which is not available to the adjoint solver (ANSYS INC, 2018). A decision had to be made to use either the fully laminar flow model, or a fully turbulent model. After consideration of the complexities involved, the flow conditions, and the areas chosen to be optimised, the laminar model was chosen. The reasons for choosing the laminar flow solver are mainly since the most beneficial areas for optimisation are that of the winglet and the payload bay of the fuselage, which both receive clean air from the pressure far field boundary condition and which comprise mostly of laminar regions of flow according to the Reynolds numbers for the various lengths. The laminar flow assumption also allowed the mesh to be coarsened while maintaining accuracy, as the laminar flow model does not have such stringent mesh requirements in the boundary layer as that of a fully turbulent model and allowed a resolved solution to be obtained with a coarser grid, this allowed the adjoint solution to be computed as accurately as possible with the limited computational resources available. One disadvantage of this approach is that once an optimised geometry was obtained, the geometry had to be exported, re-meshed, and re-analysed using the Transitional SST model

to confirm the results. This resulted in a time increase between each optimisation iteration and reduced the time efficiency of the discrete adjoint optimisation.

The decision was made not to employ adjoint optimisation over the main sections of the wing, or the engine bay section of the fuselage. The optimisation of the wing is avoided, as the validity of the optimisation cannot be confirmed when using an NLF aerofoil, and assuming either fully turbulent, or fully laminar flow. The engine bay is not optimised at the moment as the internal flow of the engine air inlet needs to be confirmed before any valuable information can be obtained from an adjoint solution. The cooling, and air flow within the engine bay will be the driving factor for the shape here, rather than drag reduction on its own. Once a fully designed and optimised propeller is incorporated, this can also influence the flow around the engine cooling bay. Thus, the main areas identified for optimisation are that of the payload bay at the front of the aircraft, the winglet root fillet profile, and if possible, it will be seen if the laminar flow assumption, and optimiser, can eliminate the wing root separation present that is seen in Figure 7-2.

The focus of the optimisation will be to reduce the drag, and not to increase the lift. The reasons for this are given below in bullet form.

- As previously stated, it is unknown whether the fully laminar assumption is valid for the optimisation case, and due to the time and resource requirements of remeshing and setting up another Transitional SST simulation after each optimisation iteration, it was decided not to optimise the wing (the main lifting surface). This could possibly be the work of future research.
- Where an increase in lift would theoretically allow for an overall improvement in the range and endurance performance of the UAV. With the current configuration, any increase in lift will also result in a reduction in cruise speed, the selected aerofoil performance starts to degrade at Reynolds numbers below 500 000 (Airfoiltools, 2021), thus, this decrease in cruising speed will most likely be detrimental in ways unforeseen by the discrete adjoint solver.

Other software packages are capable of handling adjoint optimisation with a transitional turbulence model (Halila, et al., 2020). This would be more efficient and valid for the optimisation of a main lifting surface such as a wing at the current Reynolds numbers, this could be the topic of future work.

Other than the coarser mesh, and the laminar boundary condition being applied at the walls, all other solution parameters remained the same as those stated in section 6.2.2.

7.3.4 Adjoint Solution Results and Mesh Morphing

The adjoint solutions provides the solution sensitivities to change with regards to a goal, in this case, the goal is reduction in drag. With this in mind, and without much that can be changed

in the solution other than the shape of the UAV itself, Figure 7-8 shows the shape sensitivity to the drag variable. The areas with the higher sensitivity will give larger change in the drag, with the smallest change in the shape. The areas identified as the most sensitive areas included that of the payload bay, the winglet root radius, and the wing root fillet.

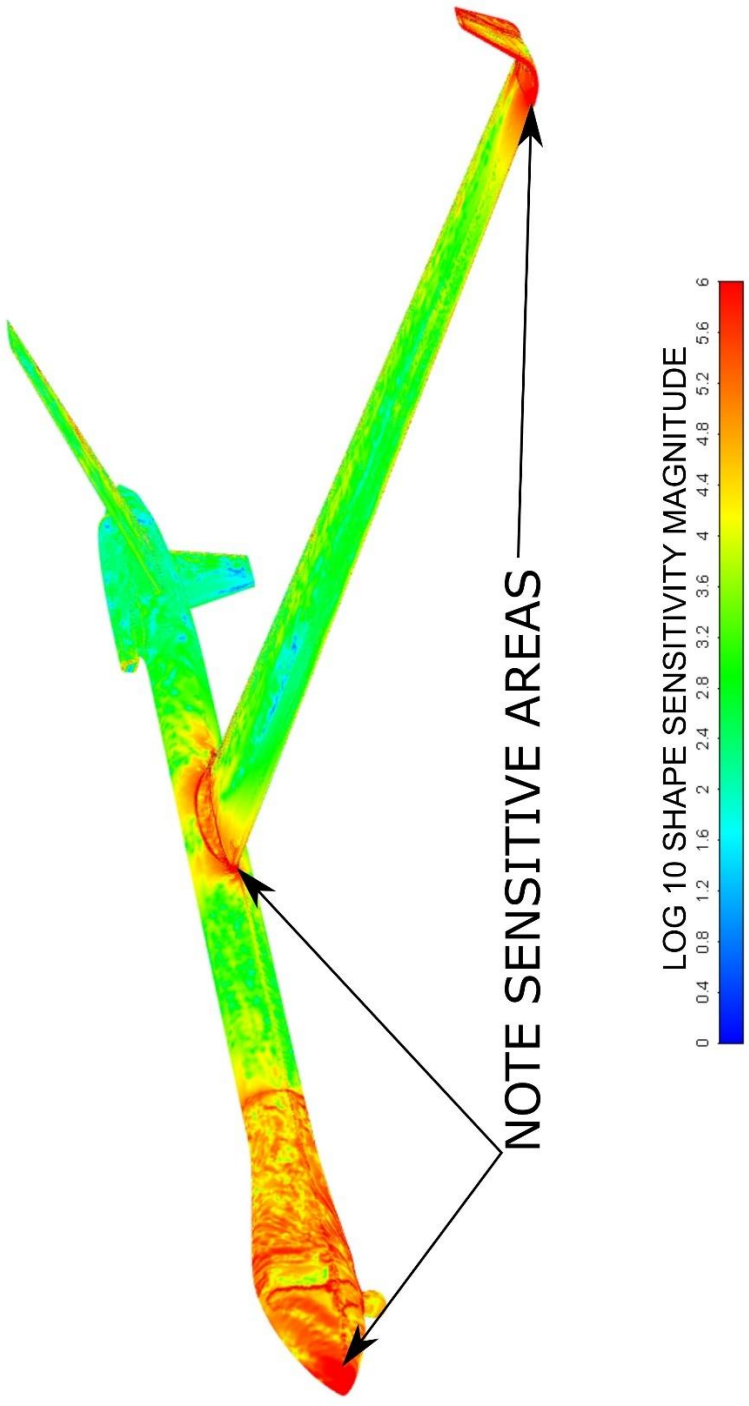

Figure 7-8: Adjoint Solution as reported by ANSYS Fluent showing Shape Sensitivity Magnitude (Log10) to the Drag

This adjoint solution was then used in combination with the ANSYS Design Tool in order to morph the geometry of the UAV, with the goal of reducing the drag. As stated earlier, only the payload bay, winglet root fillet, and wing root area were attempted for the mesh morphing.

Figure 7-9 to Figure 7-19 below show the calculated optimal boundary displacement in order to achieve the required goal of a reduction in drag. The arrows show the magnitude and direction of the displacement. The displacements in these figures are unitless, and the actual displacement value will depend on the desired (user input) change in the flow observable, in this case, the drag. A red colour arrow indicates the geometry shifting outwards (into the flow domain), and a blue colour arrow indicates the geometry shifting inwards (into the UAV geometry).

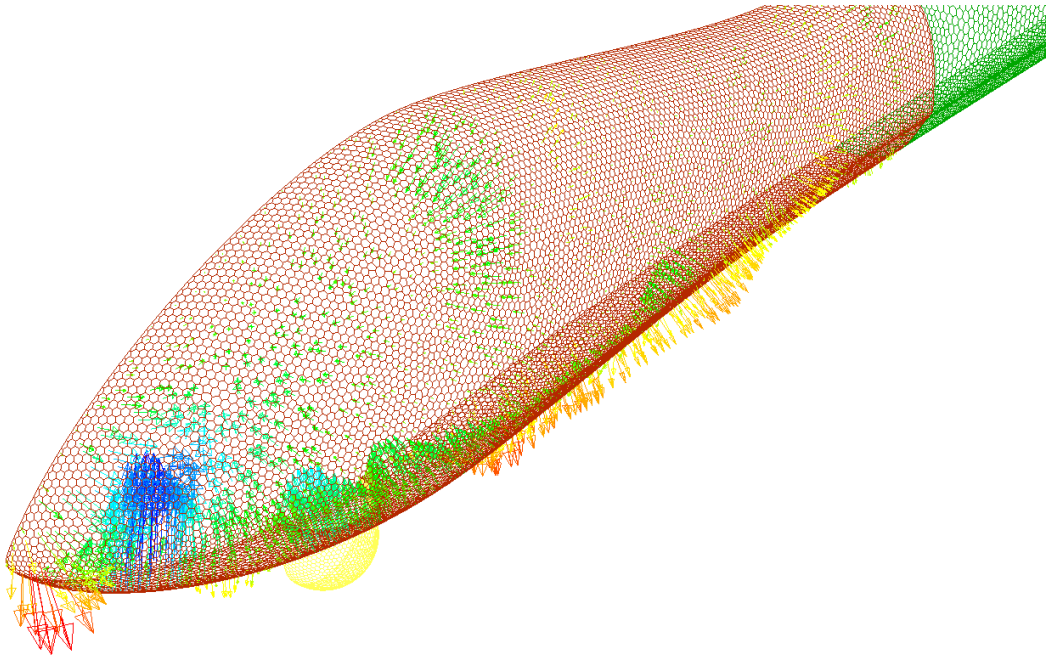

Figure 7-9: Payload Bay, Optimal Normal Boundary Displacement, View 1

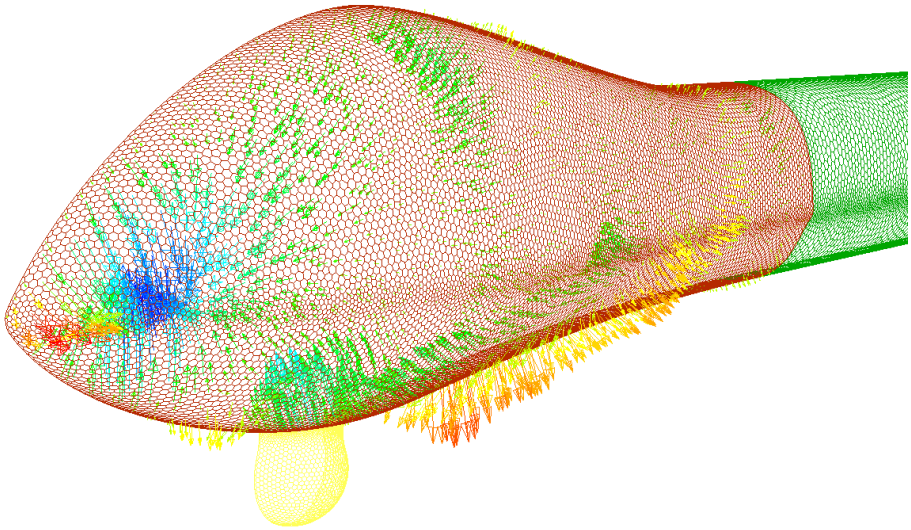

Figure 7-10: Payload Bay, Optimal Normal Boundary Displacement, View 2

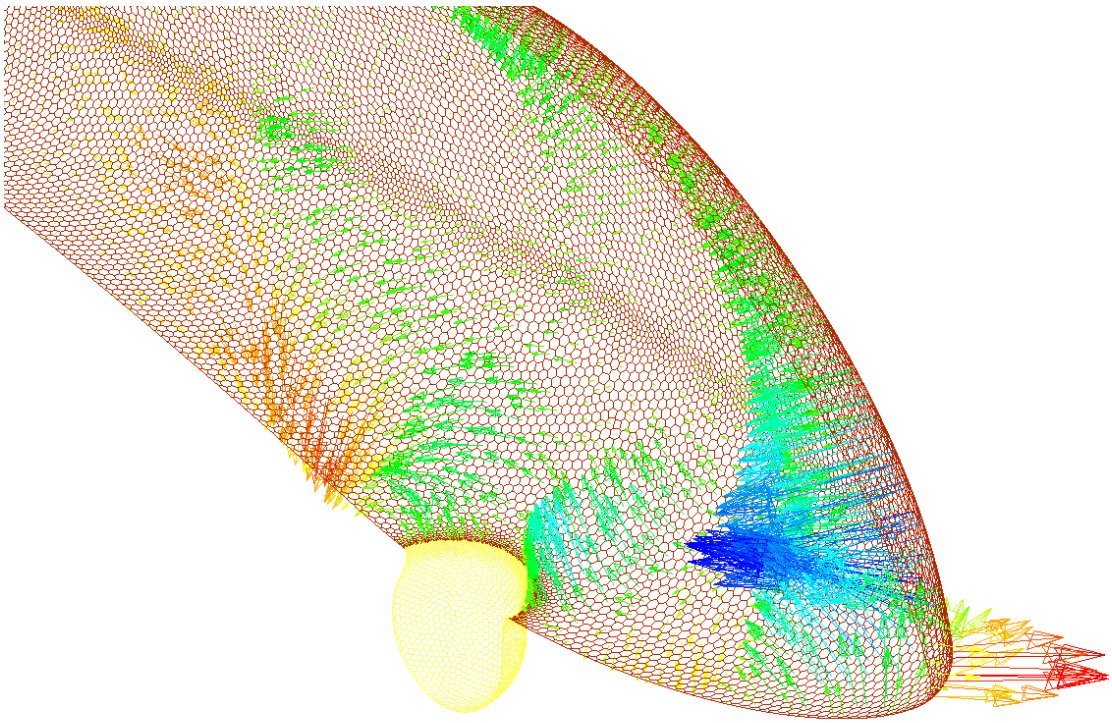

Figure 7-11: Payload Bay, Optimal Normal Boundary Displacement, View 3

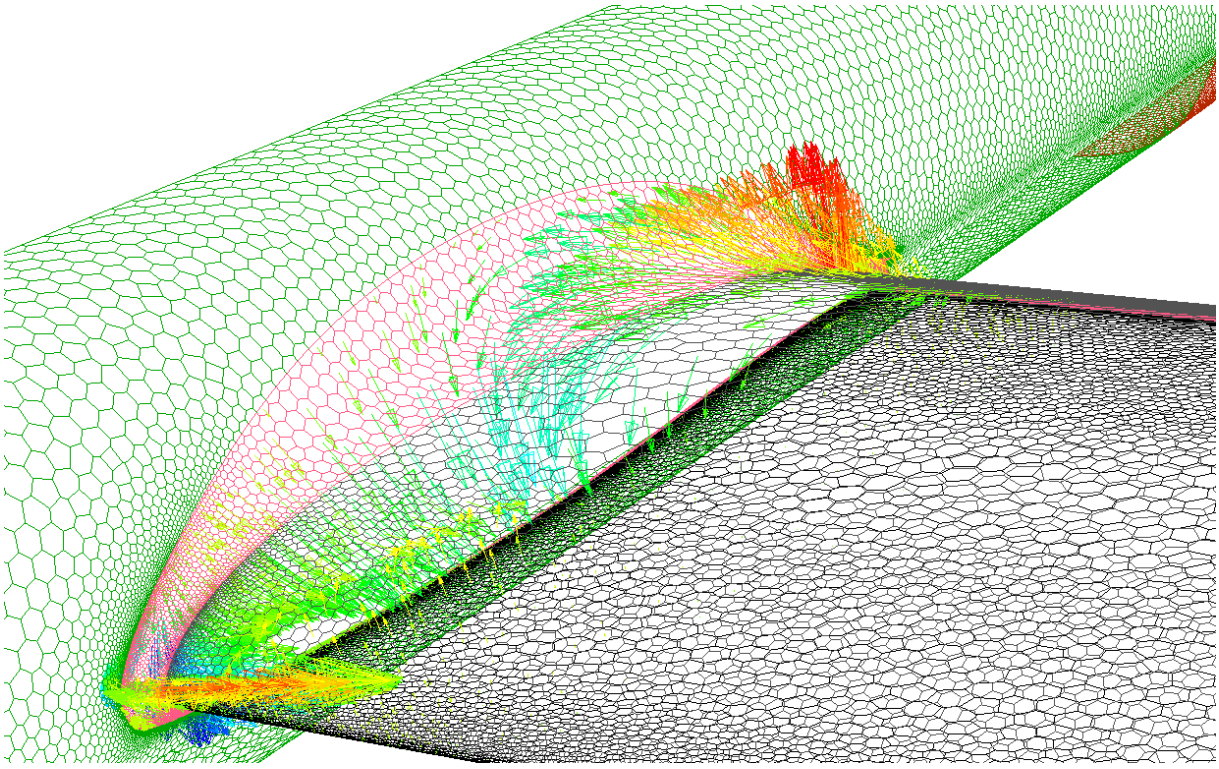

Figure 7-12: Wing Root Fillet, Optimal Normal Boundary Displacement, View 1

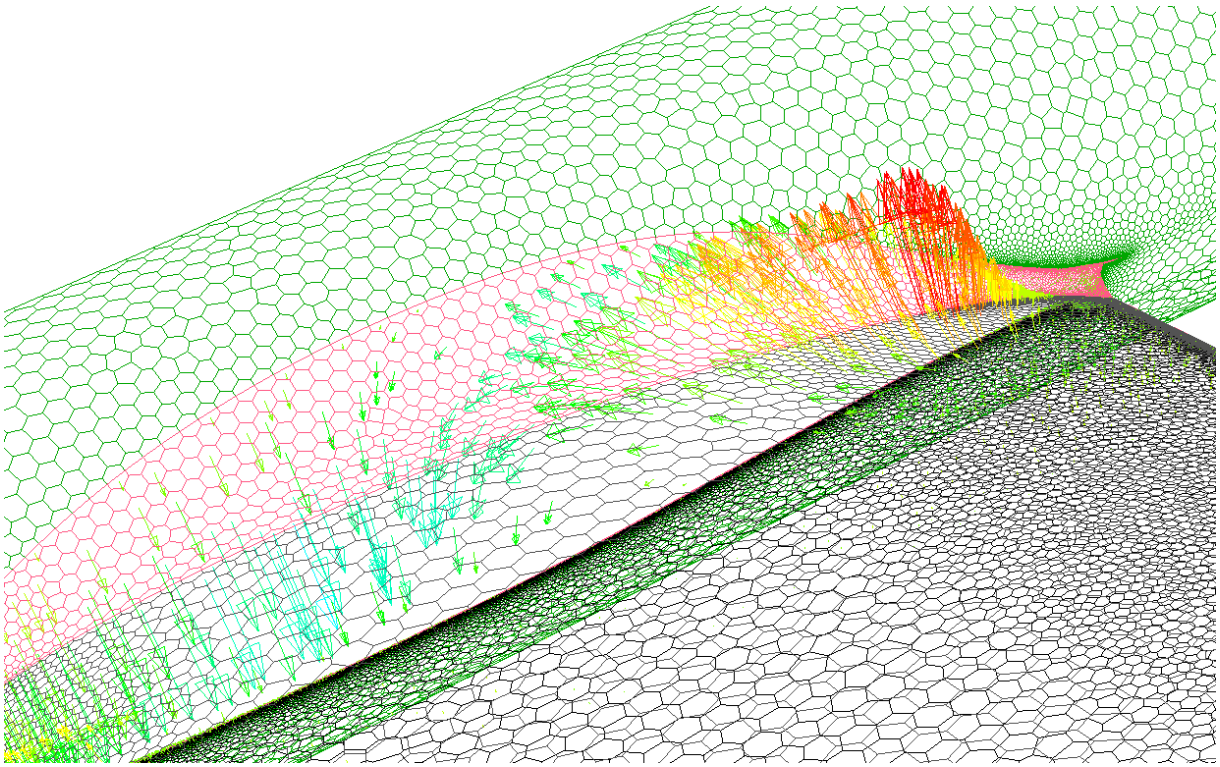

Figure 7-13: Wing Root Fillet, Optimal Normal Boundary Displacement, View 2

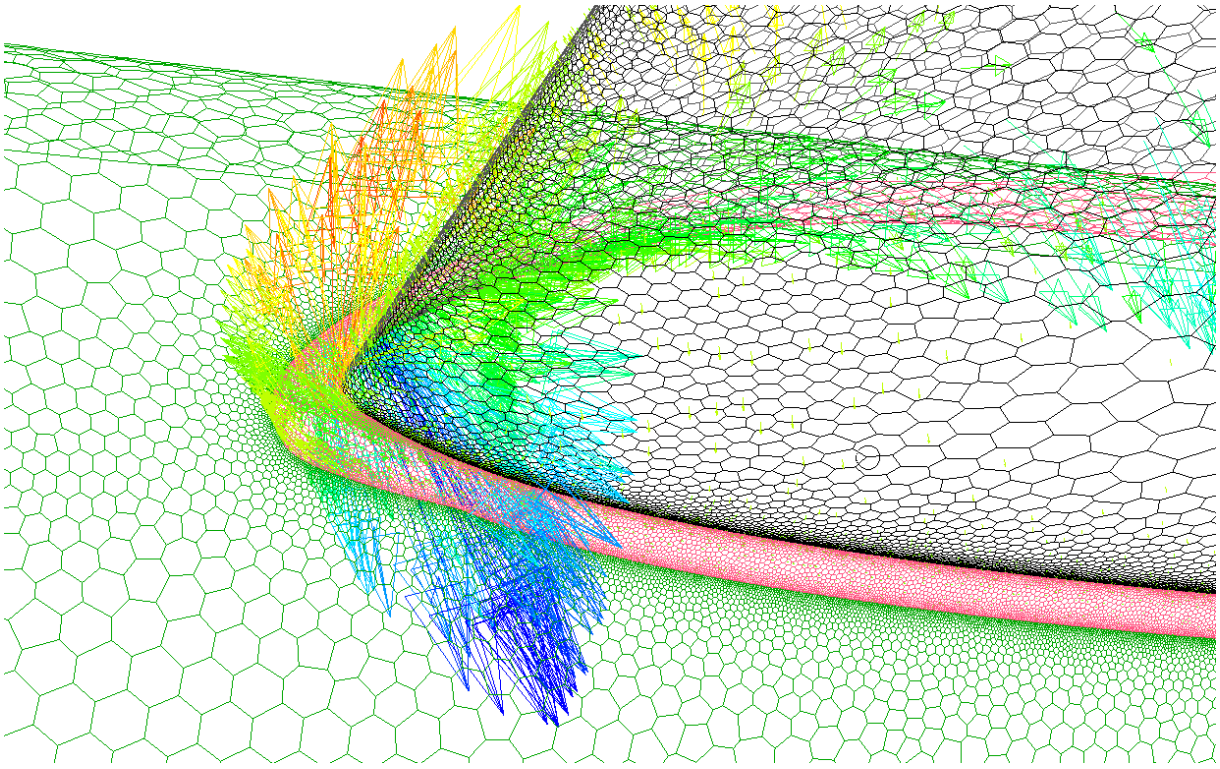

Figure 7-14: Wing Root Fillet, Optimal Normal Boundary Displacement, View 3

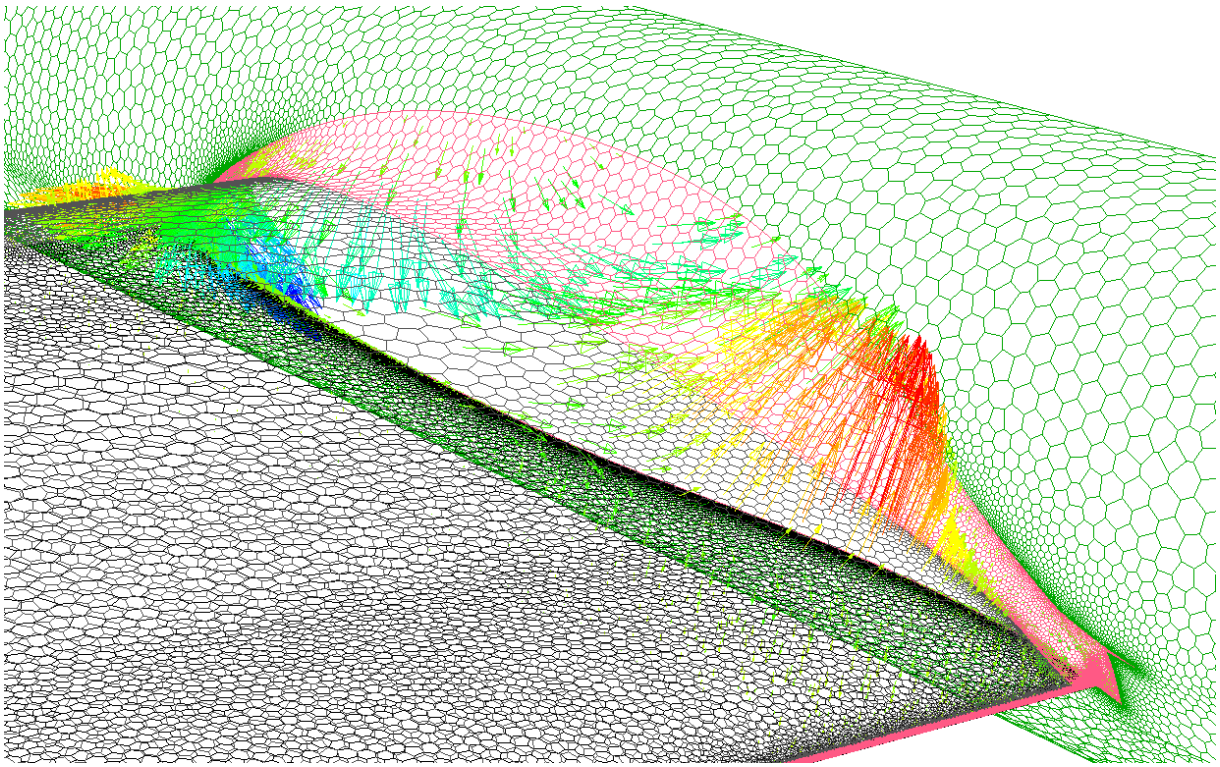

Figure 7-15: Wing Root Fillet, Optimal Normal Boundary Displacement, View 4

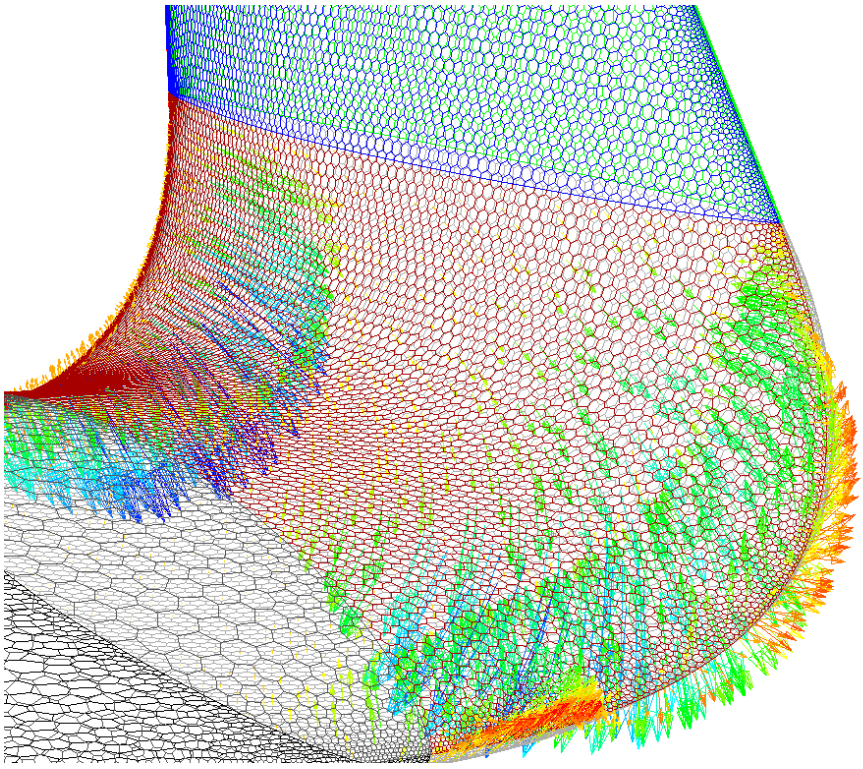

Figure 7-16: Winglet Root Fillet, Optimal Normal Boundary Displacement, View 1

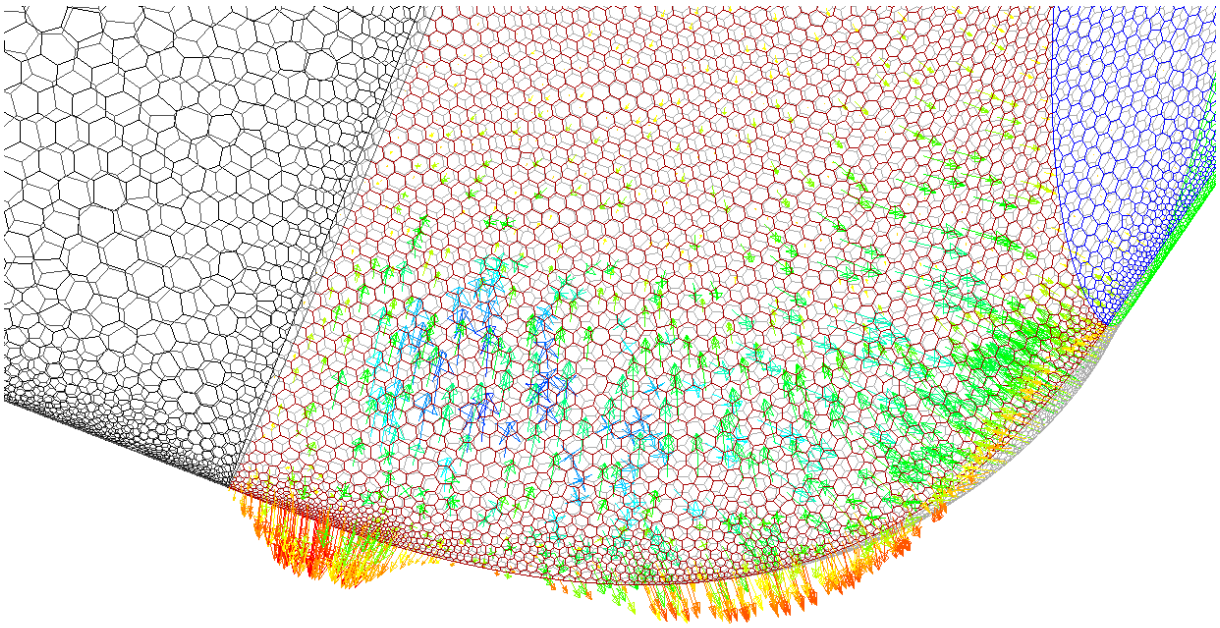

Figure 7-17: Winglet Root Fillet, Optimal Normal Boundary Displacement, View 2

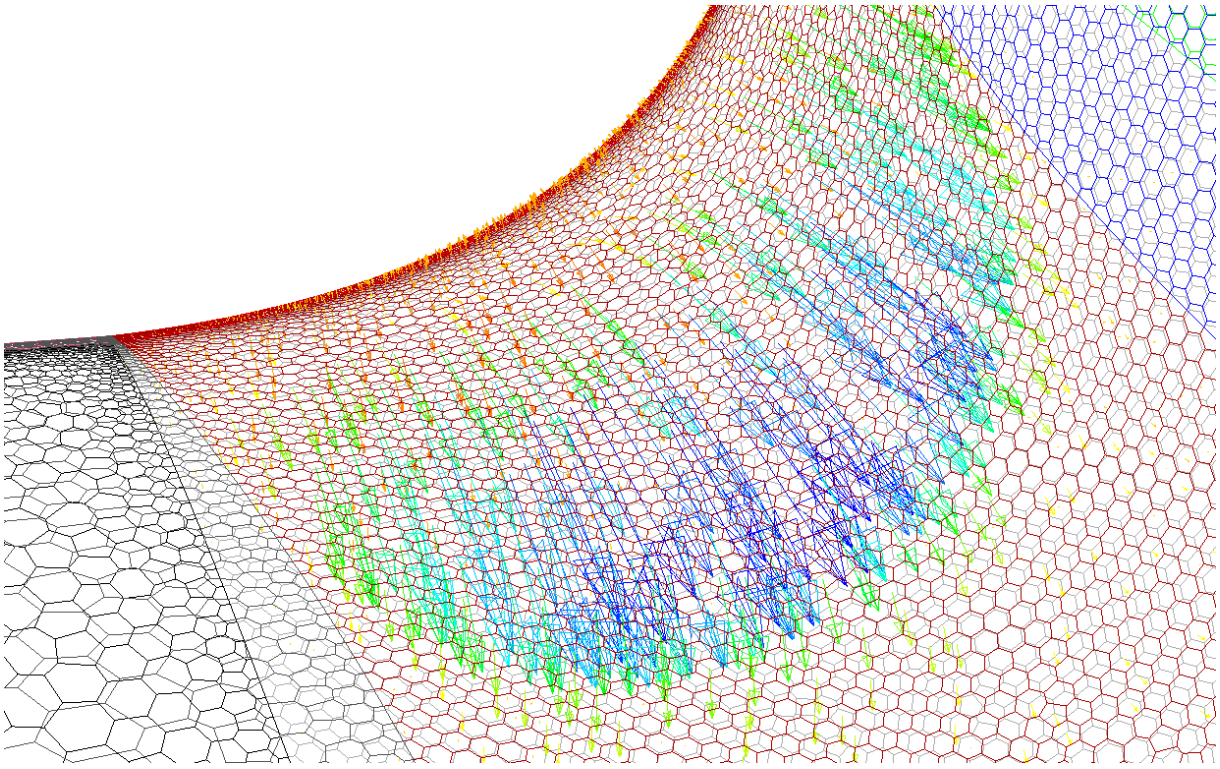

Figure 7-18: Winglet Root Fillet, Optimal Normal Boundary Displacement, View 3

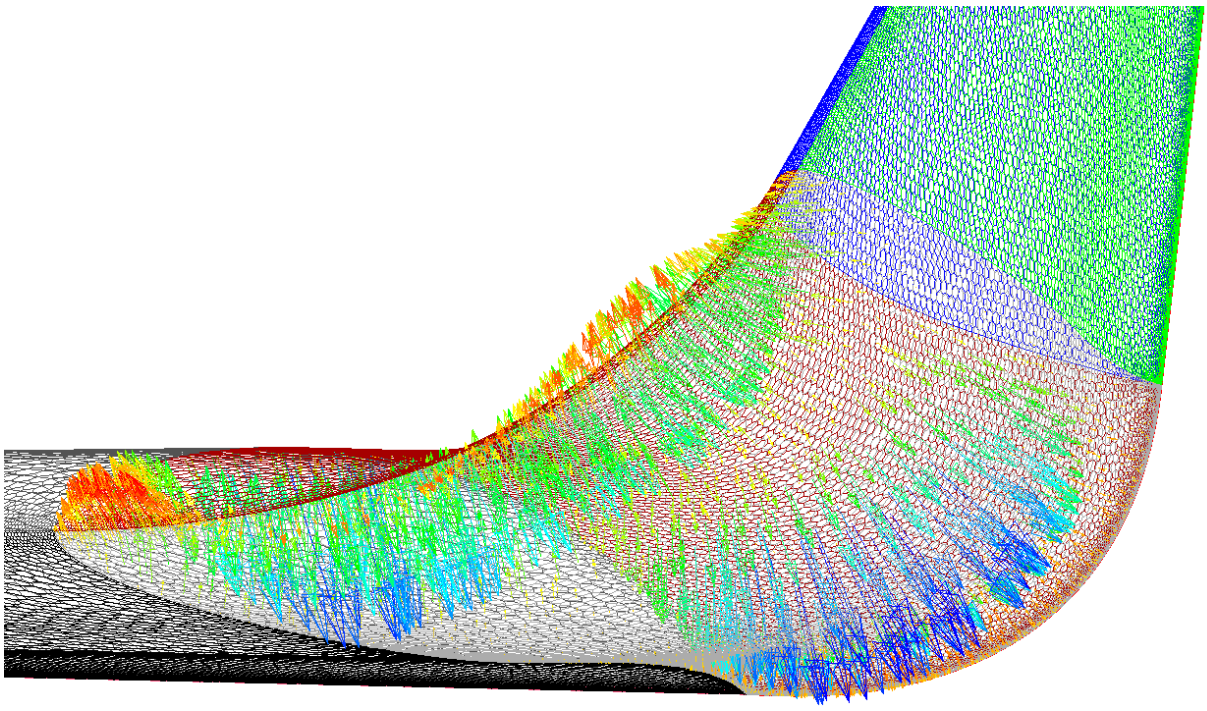

Figure 7-19: Winglet Root Fillet, Optimal Normal Boundary Displacement, View 4

Of course, the mesh morpher does not always give a desired displacement, or it may give a displacement where the benefit received from the displacement is outweighed by other requirements. The results of the geometry morphing should be viewed and interpreted with great care. As an example, Figure 7-20 and Figure 7-21 below show the wing root at the leading edge after the geometry was morphed. The mesh was morphed in a nonsensical manner, resulting in a concavity in the wing root. This is highly undesirable from a structural viewpoint, as the wing root is an area of high stress on an aircraft body, as it must handle the entire bending moment from the lift generated by the wing. As a result, this area was, in subsequent iterations, set to be ignored by the mesh morpher, and only the last 75% of the wing chord at the wing root fillet was set to be morphed by the mesh.

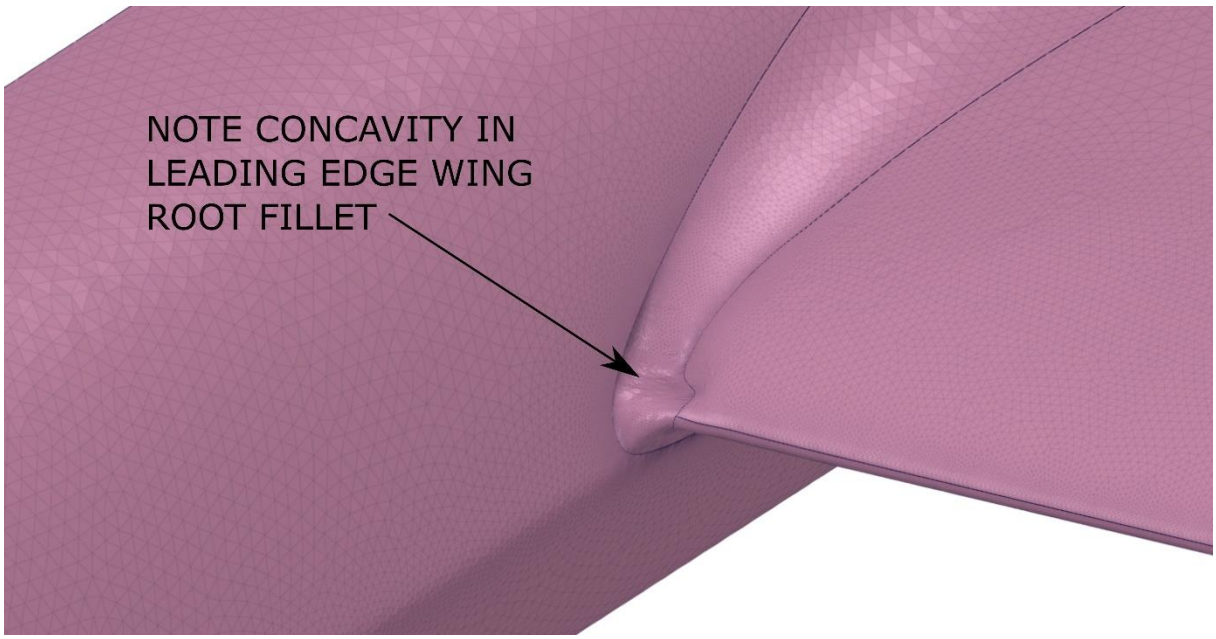

Figure 7-20: Outside View of Wing Root Leading Edge after Geometry Morphing

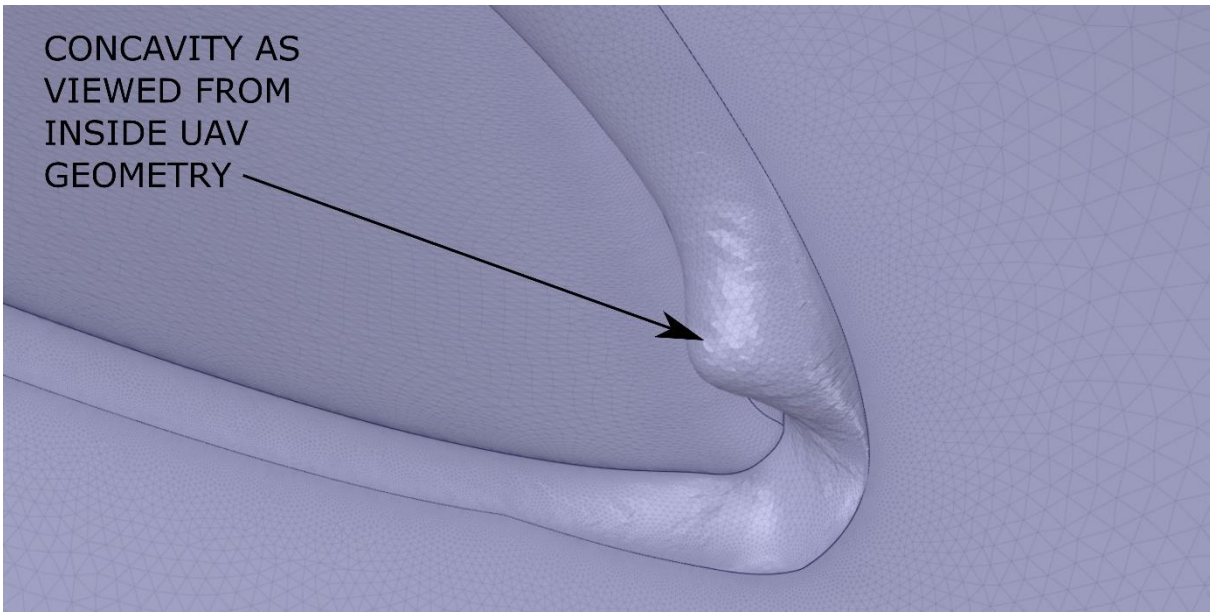

Figure 7-21: Inside View of Wing Root Leading Edge after Geometry Morphing

Figure 7-22 below also shows the payload bay area post mesh morphing, it can be seen that the front of the nose of the bay was lengthened and slightly narrowed near the front (as is indicated by the calculated optimal displacements in Figure 7-9, Figure 7-10 and Figure 7-11 above). A slight displacement of the mesh can also be seen behind the gimbal area. The displaced meshes of the wing and winglet root fillets will not be shown, as they had relatively small displacements and the difference will not be noticeable unless directly compared to the old geometry.

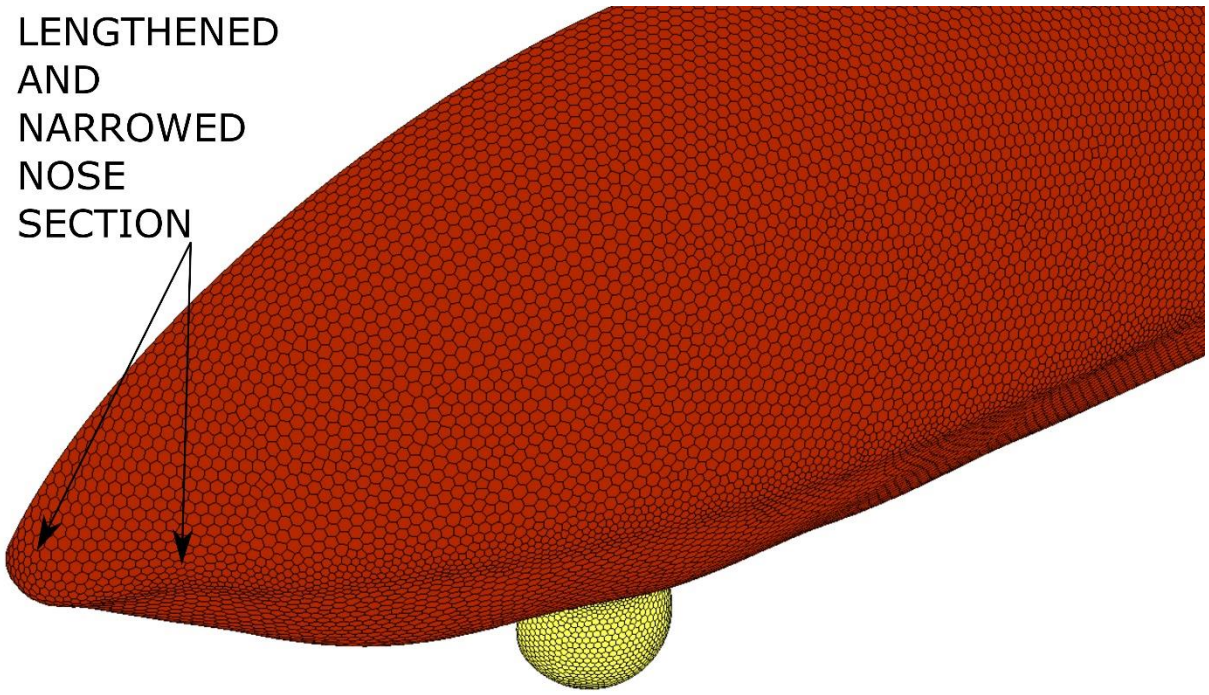

Figure 7-22: Payload Bay Boundary Mesh After Geometry Morphing

7.3.5 Adjoint Optimised Design Results

After the geometry was morphed using the ANSYS Design Tool, the morphed geometry had to be analysed again using the Transition SST turbulence model. This could not be accomplished using the same mesh that was used for the adjoint solution, thus, the morphed boundary of the UAV was exported as a Standard Triangle Language (STL) file and imported into Fluent Meshing in order to generate a mesh similar to that of the one used for the previous analysis that met the requirements of the Transitional SST turbulence model. Where the same face sizing as the previous analysis could not be used, due to the imported file being an STL, the same far-field, and body of influences were used in order to generate the new mesh, which resulted in a mesh comparable in size field and cell count to that of the mesh used for the previous analysis.

Once again, the same solution setup as that used in section 6.2.2 was used. The results of the morphed geometry are included in Table 7-2 below. For convenience and direct comparison, the results of the previous design iteration (the improved design) from Table 7-1 are included here as well.

Table 7-2: Adjoint Optimised Results Compared to Improved Results

Design Configuration	AOA [°]	Lift Coefficient	Drag Coefficient	C_L/C_D	$C_L^{3/2} / C_D$
Improved Design	2	1.166	0.040427	28.842	31.14414
Adjoint Optimised		1.1413	0.040326	28.302	30.235

The adjoint optimised geometry resulted in a decrease of both lift and drag when compared to the previous improved design. The drag was reduced by approximately 0.25%, while the lift was reduced 2.16%. When calculating the C_L/C_D and $C_L^{3/2}/C_D$, the result of using the adjoint optimiser, with the parameters and assumptions made, is a decrease in performance. Of particular concern is the decrease in the endurance parameter ($C_L^{3/2}/C_D$) of 3%. When looking at Figure 7-23 below, which shows a comparison of the lift coefficient due to pressure of the improved design, and the adjoint optimised design, it becomes evident that most of the loss of lift comes from the wing, which was not modified at all during the adjoint process. This shows the sensitivity of the wing's lift to other areas of the geometry, such as the wing root and winglet root shapes. Figure 7-24 also shows the difference in drag coefficient of the areas affected by the adjoint optimisation. This result was obtained by taking the drag coefficient of discrete areas of the adjoint optimised UAV design and subtracting the coefficients of the same discrete areas of the previous iteration (the improved design). A drag reduction was accomplished in all the areas selected for the adjoint optimisation. However, once again, the change in shape of the payload bay, wing root and winglet root resulted in a drag increase on the wing, which offsets much of the drag reduction given by the adjoint optimisation process. A few images of the differences between the adjoint optimised aerodynamic design and the improved design are included below from Figure 7-25 to Figure 7-28. The subtle, yet noticeable differences between the two configurations are apparent, particularly in the wing root fillet area, and payload bay area around the camera gimbal as seen in Figure 7-26 and Figure 7-28 respectively.

Unfortunately, the discussion above means that the adjoint optimisation process was unsuccessful. Even with a minor decrease in drag, which was the original goal, the accompanying loss of lift resulted in an overall decrease of performance in the UAV. Both the lift and drag of the UAV depend on its aerodynamic shape, and the adjoint solver does not currently have the option of fixing a variable such as lift of an area not being optimised or morphed, while simultaneously reducing the drag of another area, and both the variables will be affected by the morphed geometry. Unfortunately, in this case, the resulting loss of lift, along with the reduction in drag, does not justify using the adjoint optimised shape. This is not to say the fault lies with the adjoint optimiser itself. The overall loss of performance could be due to several reasons, including, but not limited to, the laminar flow assumption and the fact that the wing was not selected for the optimisation process as discussed in section 7.3.3.

It is the opinion of the author that more iterations can be performed, and better results can be achieved if an adjoint optimiser could be incorporated with the Transitional SST turbulence model. The fact that the laminar assumption had to be made, and that the morphed geometry had to be exported, re-meshed and re-analysed between iterations made the adjoint optimisation process time consuming, inefficient and tedious in this case. There is software

packages capable of adjoint optimisation using a transitional turbulence model, such as that studied in (Swart, 2020). This should be the topic of a future study. Beyond the laminar flow assumption made for this study, the resulting arrow shape and concavity of the payload bay is questionable at best and could possibly have a structural effect in the more detailed design phases as well. If future adjoint optimisation is to take place in further study, a smoother, more continuous shape should be aimed for, and a finer surface mesh is recommended in the areas where the geometry is morphed in order to attempt to achieve this shape.

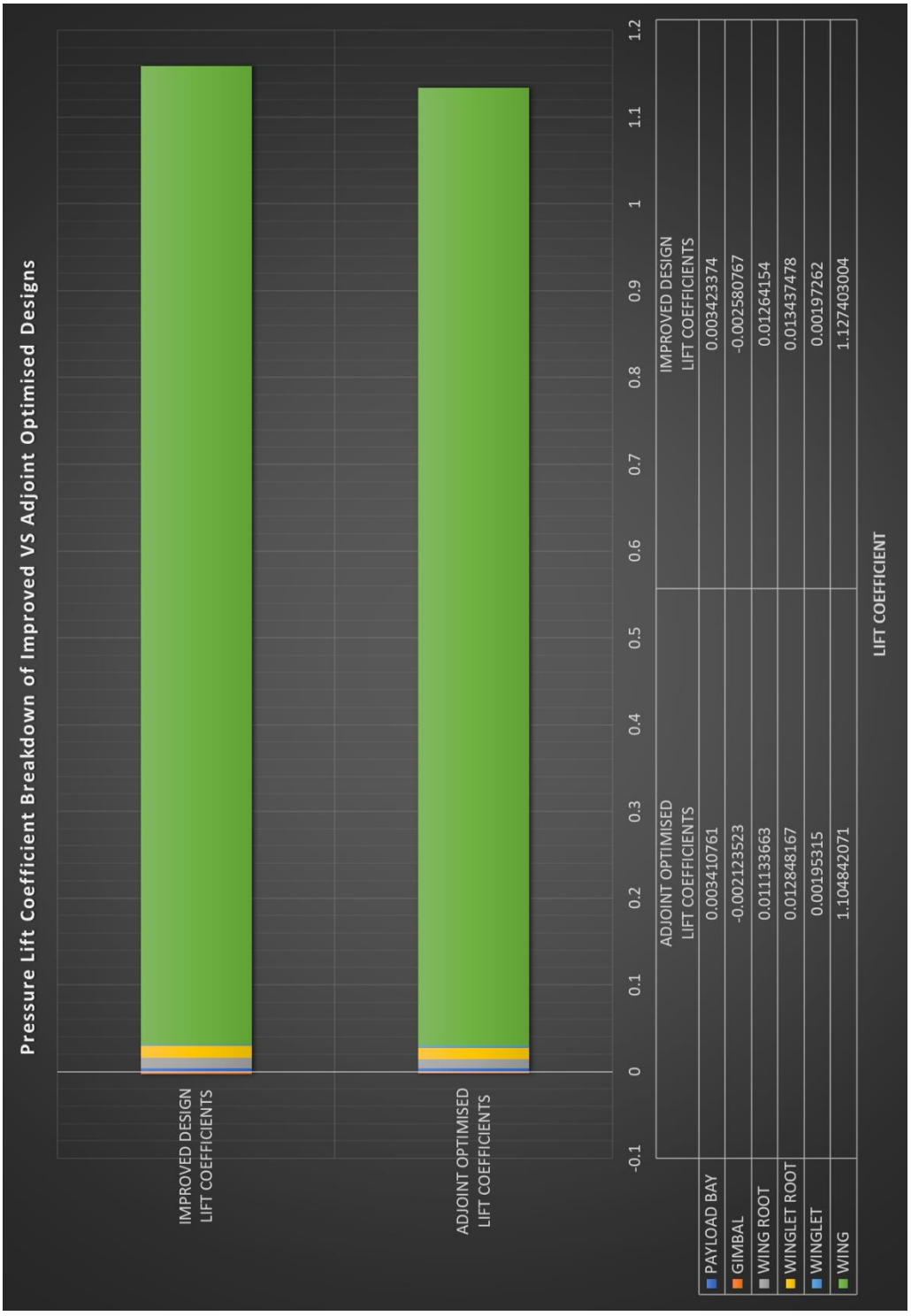

Figure 7-23: Pressure Lift Coefficient Breakdown Comparison of Improved Design VS Adjoint Optimised Design

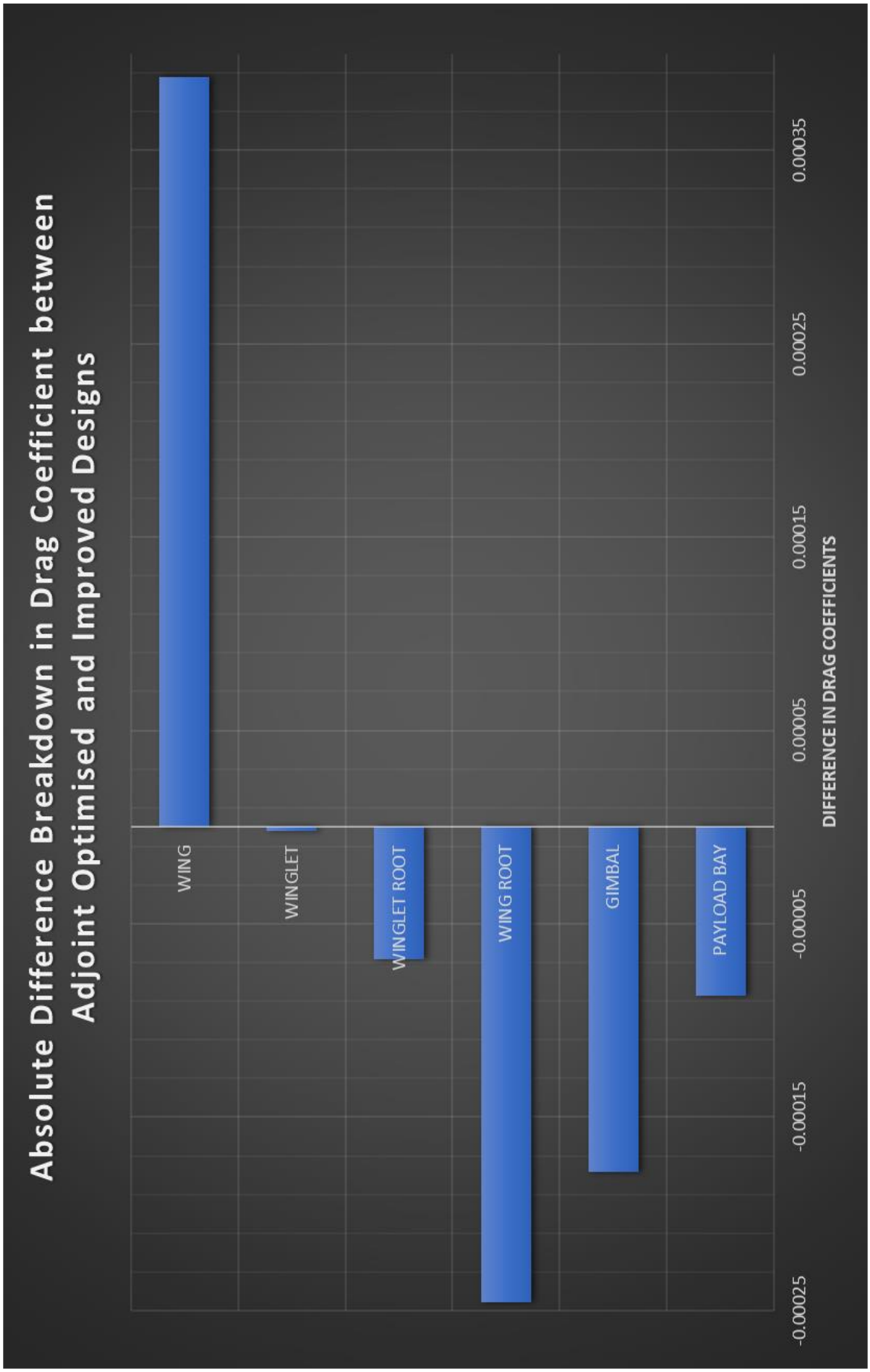

Figure 7-24: Absolute Differences between Drag Coefficients of Adjoint Optimised and Improved Designs

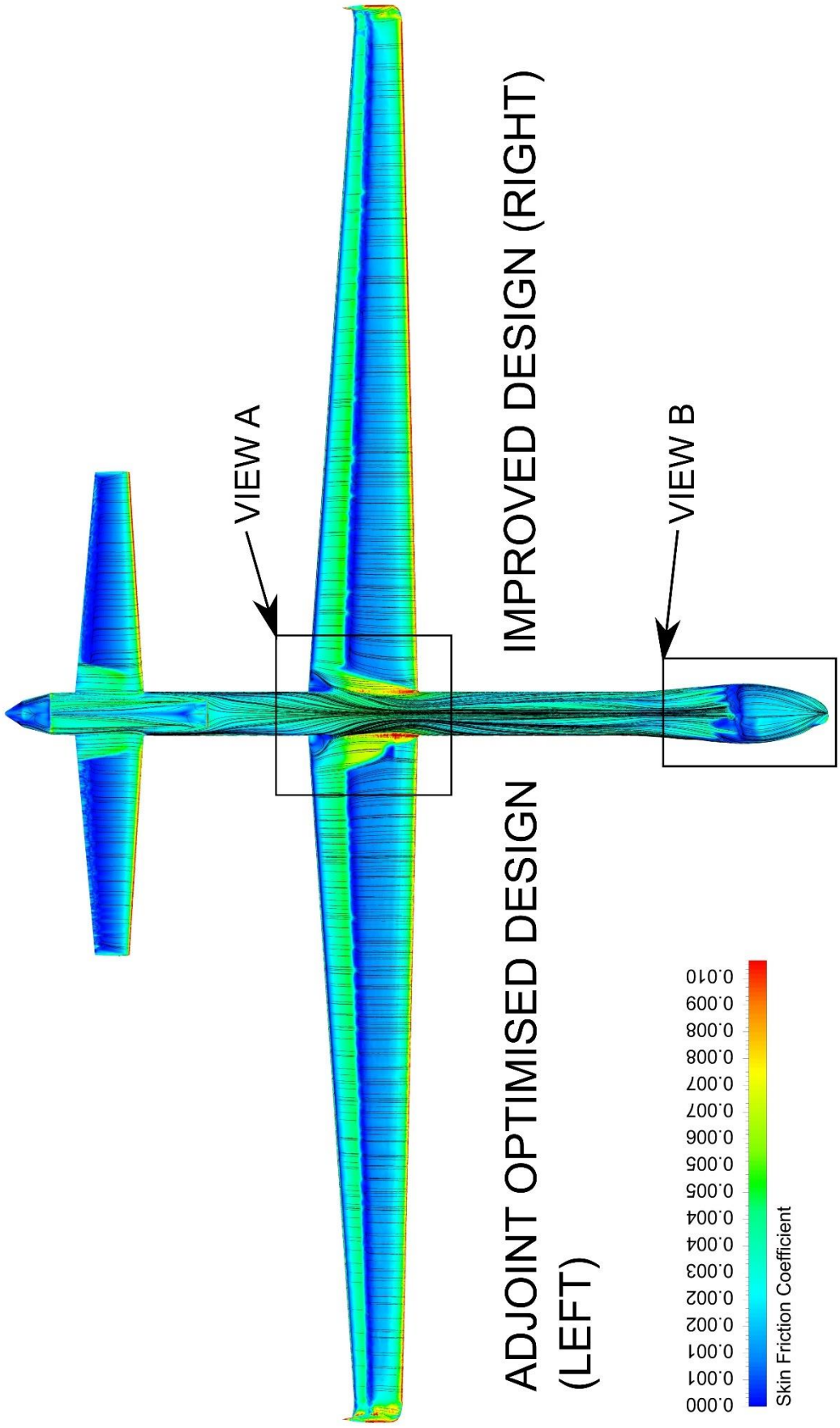

Figure 7-25: Side By Side Top View of the Skin Friction Coefficient and Surface Streamlines of Improved (Right) and Adjoint Optimised (Left) UAV Designs at 2° AOA

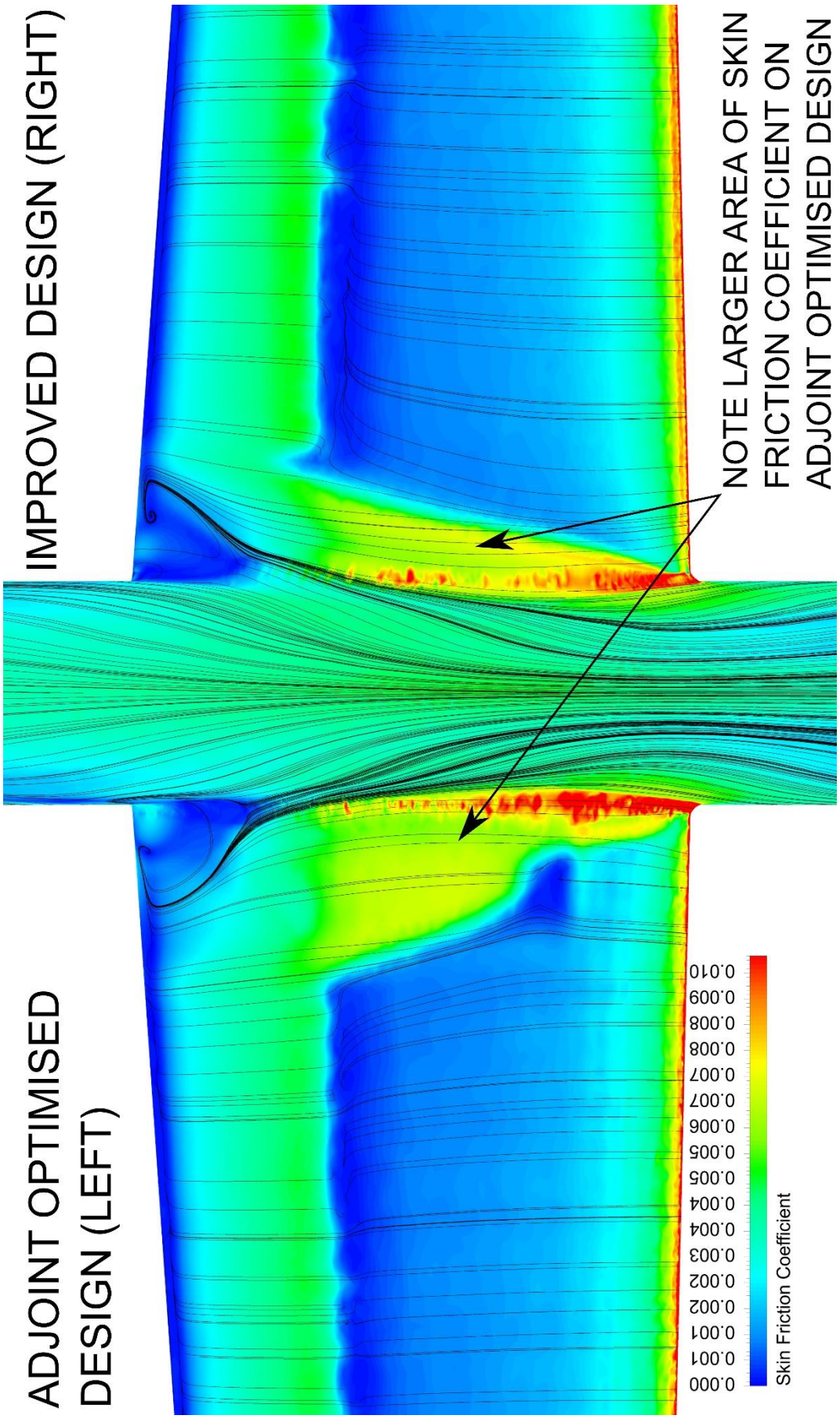

Figure 7-26: VIEW A of Figure 7-25 above

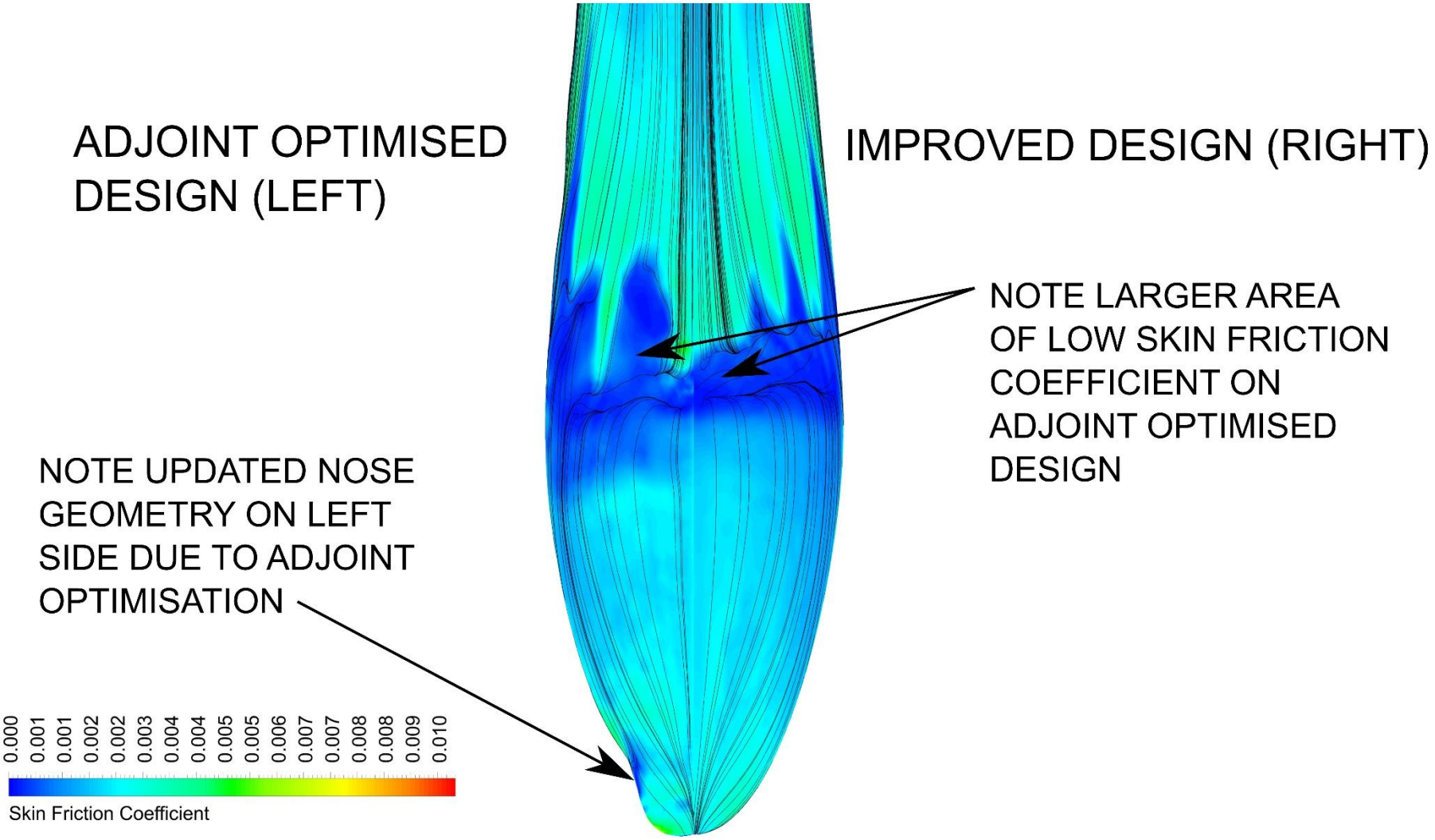

Figure 7-27: VIEW B of Figure 7-25 above

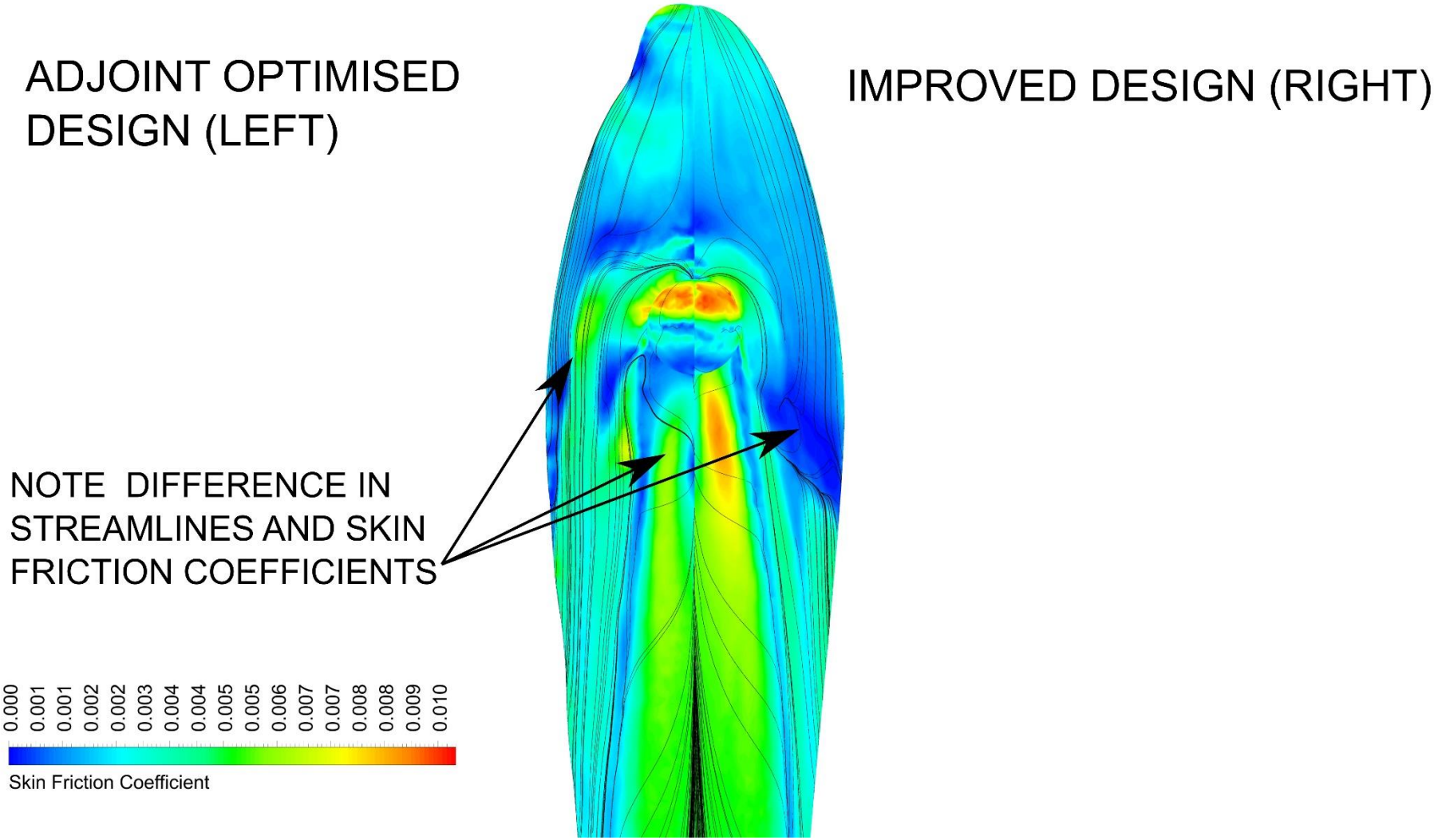

Figure 7-28: Underside of VIEW B from Figure 7-25 above

CHAPTER 8: Final Design Predicted Performance

Since the adjoint optimisation process failed at improving the overall aerodynamic performance, it is recommended that future work and study be based off the design iteration previous to the adjoint process, namely, the improved design. Thus, the improved design will be selected as the final design for the purposes of this study. This is not to say that the aerodynamic design cannot be improved or optimised further in later stages of development using the findings and recommendations of this study, but the improved design is a more aerodynamically efficient starting point for future work than the adjoint optimised design. The calculated performance of the final aerodynamic design is given in Table 8-1 below, the calculations of which are provided in APPENDIX C.2.

Table 8-1: Final UAV Design Calculated Performance

Property	Value	Units	Improvement over Initial Design [%]	Requirement Met
Endurance	26.3	Hours	13.31	Yes
Range	2765	km	6.26	Yes
Runway Take-Off Length	550	m	0	Yes
Stall Speed	27.67	m/s	0	No
Cruising Speed	37.4-33	m/s	N/A	Yes
Service Ceiling Rate of Climb	2.84	m/s	3.17	Yes
Absolute Ceiling Rate of Climb	1.84	m/s	5.44	Yes

It is worth noting that where new information was not available, and where possible, the constants used for this calculation, and the ones performed for the initial UAV design, have remained the same to keep the comparison as fair as possible. A column has been added to Table 8-1 which shows the percentage difference between the initial UAV design and the final selected design. Improvements of 13% and 6% can be seen for endurance and range respectively over the initial UAV design. Table 8-1 shows that the requirement for stall speed has still not been met, this is due to the available information used for the stall speed requirement remaining the same between the initial and final UAV designs, and the same assumptions as that mentioned in section 6.2.3 being made. Namely, this requirement should easily be met when further aerodynamic design and development is carried out and control surfaces and high-lift devices such as flaps are incorporated into the design. Control surfaces and high-lift devices are not within the scope of the present study.

Besides the stall speed, Table 8-1 shows that the final UAV aerodynamic design meets all the requirements defined in section 2.4, and shows improvements across the board for all the required criteria.

CHAPTER 9: Conclusion

The aerodynamic design and optimisation of a surveillance UAV was undertaken, with the purpose of the UAV being to assist the South African authorities in combating illegal fishing, currently happening off the coast of South Africa within its EEZ and costing South Africa billions of Rands per year.

The requirements for the UAV were defined, with its mission of maritime surveillance in mind. A combination of these requirements, existing UAV designs of similar mission types, and aerodynamic calculations were used to estimate the UAV MTOW, required engine power, UAV overall size, and required wing area. Once this starting point was defined, aerodynamic calculations using xflr5 were carried out in order to design the aerodynamic surfaces in more detail, and to determine a good starting point for the CFD simulations to be carried out.

Once an xflr5 aerodynamic configuration was designed that met or exceeded the requirements, the UAV was modelled in Solidworks, a 3D CAD package capable of the complex surface modelling required for an aerodynamic shape. The 3D model incorporated the aerodynamic design as determined by xflr5, as well as a fuselage, which housed design envelopes and masses of various systems required by a UAV, including electronic communication equipment, landing gear, engine, engine subsystems and fuel. The COG of the various systems was also considered during the initial design and modelling phase in order to design a UAV that is statically stable in the longitudinal direction.

Once the 3D model of the initial design was complete the design was analysed using the commercial CFD software package, ANSYS Fluent. Before the analysis of the actual UAV geometry was carried out, a validation case was done in order to confirm the accuracy of the CFD method used in the analysis. This validation case used a well-documented case of a high lift geometry aircraft configuration, incorporating slats and flaps. Both wind tunnel data, as well as CFD data from several reputable sources as referenced in section 6.1 was available to compare to the performed validation case. The results of the validation case agreed well with the lift, drag and moment data available from the wind tunnel experiment performed by NASA. As such, it was deemed that the method used during the validation case, if used for the current UAV design (a simpler geometry), would yield accurate results. The outcomes obtained during the validation case were also discussed and carried over into the initial UAV design analysis.

The analysis of the initial UAV design incorporated a Poly-Hexcore grid, a powerful grid type, capable of quickly, easily and accurately meshing complex geometry involving compound curvature, such as that of an aerodynamic body. The Transitional SST turbulence model was used, which considers the transition from laminar to turbulent flow. This turbulence model was used because the laminar flow region of the UAV design can have a significant impact on the results, particularly with regards to the predicted drag, as shown by other studies such as

(Swart, 2020) and (Chen, et al., 2020). The initial UAV design was analysed at its cruising altitude conditions and lowest cruising speed, at various angles of attack in order to determine the overall performance. The initial UAV design, using the results of the CFD and general aerodynamic calculations was found to meet the all the requirements defined, besides that of the stall speed. It is believed that incorporating a high-lift device, such as a flap, would result in the stall speed requirement also being met. A high-lift device needs to be designed in conjunction with control surfaces and is the topic of future research.

A grid independency study was also carried out in order to quantify the sensitivity of the lift and drag results against the number of cells used in the analysis. Convergence was dealt with in the typical way used by other research as seen in section 6.3. The outcomes of the grid independency study showed that a cell count of approximately 34 million cells would be required. Thus, the 34 million cell grid was selected as the grid for the final simulations, as it offered the best compromise between computational expense, and accuracy. It was particularly important that this fine grid be used close to the stall AOA, as this accuracy is required to accurately capture separation as shown by the validation case.

An initial study was done on the UAV design to determine the effect a propeller might have on the results, including any detrimental effects on the rear stability surfaces. A momentum source disk model was used to mathematically model the effects of the propeller, and no detrimental effects on the rear control surfaces were found, besides an increase in drag of approximately 3.2% under cruise conditions. This matched the results of more detailed analysis performed on similar geometry that was found in literature, namely, (Chen, et al., 2015).

The results of the CFD studies mentioned above, along with engineering and aerodynamic knowledge, were all used in conjunction to determine possible areas of aerodynamic design improvement. During this improvement, an analysis was carried out on the initial geometry using the Spalart-Allmaras turbulence model, instead of the Transitional SST. This analysis found that the fully turbulent assumption used in the Spalart-Allmaras model, at the Reynolds numbers and geometry areas present in the current study, can overpredict the viscous drag by as much as 42%. This difference in the viscous drag between a fully turbulent and a transitional turbulence model gave key insight into methods of aerodynamic improvement and drag reduction. The area identified as having the best potential for improvement was the wing design. This key to this potential existed in the location of the transition from laminar to turbulent flow over the surface of the wing. The viscous drag produced by turbulent flow is well known to be larger than that produced by laminar flow (Anderson, 2011). One can deduct from this that increasing the extent of laminar flow over a given area, would decrease overall drag. A Natural Laminar Flow aerofoil, which is specifically designed to increase the area of laminar flow over the top of the wing, was therefore incorporated into the improved design. Beyond this aerofoil update, a winglet design was also added in order to reduce the effect of the observed

wing tip vortices. These changes to the UAV geometry also resulted in various systems, such as the fuel and landing gear, having to be redistributed, which resulted in the COG of the UAV moving aft, and the updated wing design having to move aft to maintain flight stability. After updated CFD simulations were performed, following the same method as the initial design, it was discovered that this improved design increased the C_L/C_D and $C_L^{3/2}/C_D$ parameters by 5.9% and 13.37% respectively. These parameters are of utmost importance for the present study, as they determine the range and endurance of the aircraft.

After the improvements mentioned above were made to the design, the ANSYS Fluent discrete adjoint optimiser was used to determine the surfaces of the UAV most sensitive to the drag of the aircraft. Unfortunately, the adjoint optimiser is not available with the Transitional SST turbulence model, as was used for the rest of the CFD analysis, and thus, a laminar flow assumption had to be made for the adjoint analysis. Using the adjoint solver data, the geometry of the payload bay, winglet root fillet, and wing root fillet, were all morphed automatically by the ANSYS Design tool with the goal of minimising drag. This newly morphed geometry was then reimported into ANSYS meshing as an STL file, re-meshed, and analysed using the Transitional SST turbulence model once again to confirm the validity of the laminar flow assumption that was used for the adjoint optimisation. This updated analysis confirmed that the adjoint optimisation process, with the assumptions made, reduced the drag coefficient by 0.25%, however, this also resulted in a reduction in lift of 2.16%. Along with this, the adjoint optimiser produced areas of concavity in the geometry, which are questionable in terms of validity and accuracy, and may have a detrimental effect pertaining to the structural requirements of the UAV. This resulted in the adjoint optimisation process reducing the overall performance of the design, and the adjoint optimised shape was not selected for the final design. It is however believed that if an adjoint solver is employed with the Transitional SST turbulence model, along with a finer surface mesh, more valid and improved results can be obtained.

The improved design, and not the adjoint optimised design was then selected as the final aerodynamic design for possible future study and development, which not only met, but exceeded the main requirements of the endurance and range parameters.

CHAPTER 10: Recommendations

An efficient UAV aerodynamic design was realised, exceeding the defined requirements. There is still much work to do before an actual UAV design is complete. There are many further areas of possible research on this design, and where much of the research can focus on structural or electrical aspects in order to further the design, recommendations here will only be made for further aerodynamic research.

Further aerodynamic design needs to be done with regards to this UAV, including that of control surface and high-lift device design. A high-lift device was proven to be needed in order to meet the stall speed requirement of the UAV, which was not satisfied in the present study. Furthermore, CFD analysis can be carried out on the final design across a variety of speed ranges and angles of attack, and not just cruise, to determine an entire performance envelope.

The engine cooling system was not a topic of this study; however, an estimation of the shape and size of the cooling duct was required for the analysis as this will have a detrimental effect to the drag. This estimation of the engine cooling duct will serve as a starting point for future work in the design of the engine cooling system, which will be needed for the final UAV. Internal cooling flow was not included in the performed analysis and design and optimisation of the S-duct or similar required for engine cooling needs to be performed.

Adjoint optimisation solvers that can incorporate transitional turbulence models do exist (even if not in ANSYS Fluent), and it is believed that if further research is conducted into the optimisation of this design with these solvers, an improvement in aerodynamic performance can be realised.

A wing root fillet area of flow separation exists under cruise conditions in this current design, which leads to increased drag, and potential flow buffeting during flight. Research and optimisation can be performed to eliminate this wing root fillet separation and improve aircraft drag.

CHAPTER 11: References

Abbot, I. H. & Von Doenhoff, A. E., 1959. *Theory of Wing Sections - Including a Summary of Airfoil Data.* 1st ed. New York: Dover Publications Inc..

AeroVironment, n.d. *Raven.* [Online] Available at: https://www.avinc.com/uas/view/raven [Accessed 5 June 2019].

Airfoil Tools, 2019. *NACA 63(4)-421.* [Online] Available at: http://airfoiltools.com/airfoil/details?airfoil=naca634421-il [Accessed 15 February 2019].

Airfoil Tools, 2020. *Airfoil Tools.* [Online] Available at: http://airfoiltools.com/ [Accessed 17 January 2020].

Airfoiltools, 2021. *NASA NLF1015.* [Online] Available at: http://airfoiltools.com/airfoil/details?airfoil=nlf1015-il [Accessed 11 March 2021].

Ali, A., 2018. *CFD Workflow Guide: How to set up a Fluid Dynamics Analysis.* [Online] Available at: https://www.simscale.com/blog/2016/09/cfd-workflow-quick-guide/ [Accessed 27 May 2019].

Alti, n.d. *Transition.* [Online] Available at: https://www.altiuas.com/transition/ [Accessed 5 June 2019].

American Institute of Aeronautics and Astronautics, 2010. *1st AIAA CFD High Lift Prediction Workshop (HiLiftPW-1).* [Online] Available at: https://hiliftpw.larc.nasa.gov/index-workshop1.html [Accessed 1st September 2019].

American Institute of Aeronautics and Astronautics, 2020. *1st AIAA Transition Modeling and Prediction Workshop CRM-NLF Grid Generation Guidelines.* [Online] Available at: transitionmodeling.larc.nasa.gov/wp-content/uploads/sites/109/2020/02/CRM-NLF_GridGuidelines.pdf [Accessed 18 June 2020].

Anderson, J. D., 1989. *Introduction to Flight.* 3rd ed. New York: McGraw-Hill.

Anderson, J. D., 2011. *Fundamentals of Aerodynamics.* 5th ed. New York: McGraw-Hill.

ANSYS INC, 2018. *ANSYS Fluent Theory Guide,* Canonsburg: ANSYS INC.

ANSYS INC, 2018. *ANSYS Fluent User's Guide,* Canonsburg: ANSYS INC.

AUVSI News, 2013. *Are UAS more cost effective than manned flights.* [Online] Available at: https://www.auvsi.org/are-uas-more-cost-effective-manned-flights [Accessed 27 January 2020].

Azabi, Y., Savvaris, A. & Kipouros, T., 2017. *Initial Investigation of Aerodynamic Shape Design Optimisation for the Aegis UAV.* Bucharest, s.n.

Bernard Micro Systems, n.d. *UAV Design Guidelines.* [Online] Available at: https://barnardmicrosystems.com/UAV/uav_design/guidelines.html [Accessed 15 January 2019].

Bravo-Mosquera, P. D., Botero-Bolivar, L., Acevedo-Giraldo, D. & Ceron-Munoz, H. D., 2017. Aerodynamic design analysis of a UAV for superficial research of volcanic environments. *Aerospace Science and Technology,* Volume 70, pp. 600-614.

Carvalho, J. N. D., 2016. *Optimizing UAV Aerodynamics with Computational Fluid Dynamics,* Lisbon: Tecnico Lisboa.

CFD Support, n.d. *General CFD Workflow.* [Online] Available at: https://www.cfdsupport.com/OpenFOAM-Training-by-CFD-Support/node14.html [Accessed 27 May 2019].

Chaffin, M., 2010. *Grid System Overview,* Chicago: American Institute of Aeronautics and Astronautics.

Chen, G. et al., 2015. Numerical Simulation Study on Propeller Slipstream Interference of High Altitude Long Endurance Unmanned Air Vehicle. *The Institute of aerodynamics theories and application of China Academy of Aerodynamic Aerospace,* Issue 99, pp. 361-367.

Chen, L., Guo, Z., Deng, X. & Hou, Z., 2020. Aerodynamic performance and transition prediction of low-speed fixed-wing unmanned aerial vehicles in full configuration based on improved γ−Reθ model. *Aersoapce Science and Technology,* 107(106281).

Cho, J.-H., 2014. Experimental and numerical investigation of the power-on effect for a propeller-driven UAV. *Aerospace Science and Technology,* Issue 36, pp. 55-63.

Cogan, D. J., 2016. *The aerodynamic Design and Development of an Urban Concept Vehicle Through CFD Analysis,* Cape Town: Cape Peninsula University of Technology.

defenceWeb, 2018. *DAFF working on illegal, unregulated and unreported fishing as part of Phakisa.* [Online] Available at: http://www.defenceweb.co.za/index.php?option=com_content&view=article&id=50940 [Accessed 16 June 2018].

Depperois, A., 2019. *Theoretical limitations and shortcomings of xflr5.* [Online] Available at: http://www.xflr5.tech/docs/Part%20IV:%20Limitations.pdf [Accessed 16th December 2019].

Digernes, T. & Endal, A., 1980. *Fishing Vessel Speed and Fuel Economy,* Trondheim: Institute of Fishery Technology Research.

ENCA, 2014. *Illegal fishing a major threat so SA's marine life.* [Online] Available at: https://www.enca.com/illegal-fishing-major-threat-sas-marine-life [Accessed 16 June 2018].

Erwin, S., 2017. *U.S. Military gets taste of new satellite technology for unmanned aircraft.* [Online]
Available at: https://spacenews.com/u-s-military-gets-taste-of-new-satellite-technology-for-unmanned-aircraft/
[Accessed 5 June 2019].

Fredericks, I., 2018. *Send-off for second CPUT nano-satellite.* [Online] Available at: https://www.cput.ac.za/newsroom/news/article/3539/send-off-for-second-cput-nano-satellite
[Accessed 16 June 2018].

Fu, W., Li, J. & Wang, H., 2012. Numerical Simulation of Propeller Slipstream Effect on A Propeller-Driven Unmanned Aerial Vehicle. *International Conference on Advances in Computational Modeling and Simulation,* Issue 31, pp. 150-155.

Gautham, N. & Bibin, J., 2016. Effect of winglets induced tip vortex structure on the performance of subsonic wings. *Aerospace Science and Technology,* Volume 58, pp. 328-340.

GetSAT, 2019. *MicroSAT LW,* Mclean: GetSAT.

Giles, M. B. & Pierce, N. A., 2000. An Introduction to the Adjoint Approach to Design. *Flow, Turbulence and Combustion,* Issue 65, pp. 393-415.

Glazewski, J., 2013. *Illegal fishing in Southern African Waters and Beyond: Prevention and law enforcement,* Cape Town: University of Cape Town.

Gopalarathnam, A. & Selig, M. S., 2001. Low-Speed Natural-Laminar-Flow Airfoils: Case Study in Inverse Airfoil Design. *Journal of Aircraft,* 38(1), pp. 57-63.

Halila, G. L., Martins, J. R. & Fidkowski, K. J., 2020. Adjoint-based aerodynamic shape optimization including transition to turbulence effects. *Aerospace Science and Technology,* Issue 107.

IBM ISV & Developer Relations, 2012. *IBM Information Technology Guide for ANSYS Fluent Customers,* New York: IBM Global Services.

IMSAR, 2017. *OneSAR,* Springville: IMSAR.

Jane's By IHS Markit, 2017. *Persistence over water: Operators look to UAS for extended coverage,* s.l.: Jane's By IHS Markit.

Kings, S., 2016. *SA all at sea over illegal fishing,* Johannesburg: Mail & Guardian.

Kontogiannis, S. G. & Ekaterinaris, J. A., 2013. Design, performance evaluation and optimization of a UAV. *Aerospace Science and Technology.*

Lee, K., 2004. *Development of unmanned aerial vehicle (UAV) for wildlife surveillance,* Florida: University of Florida.

Manwell, J. F., McGowan, J. G. & Rogers, A. L., 2010. *Wind Energy Explained: Theory, design and application.* Chichester: Wiley.

Maughmer, M. D., n.d. *The Design of Winglets for Low-Speed Aircraft,* Pennysylvania: The Pennysylvania State University.

NASA Dryden Flight Research Center, n.d. *Technology Facts: Winglets,* Edwards: NASA Dryden Flight Research Center.

Neuhart, D. H. & McGinley, C. B., 2004. *Free-Stream Turbulence Intensity in the Langley 14-by 22-Foot Subsonic Tunnel,* Hampton: NASA Langley Research Center.

Northrop Grumman, 2016. *MQ-4C Triton,* San Diego: Northrop Grumman.

Northrop Grumman, n.d. *Triton.* [Online] Available at: http://www.northropgrumman.com/MediaResources/Pages/Photo.aspx?pid%3DBA-10002_006%26rel%3D%2F%26name%3DPhotos
[Accessed 5 June 2019].

Northwest UAV, 2019. *Northwest UAV Catalog,* McMinnville: Northwest UAV.

Northwest UAV, 2020. *Northwest UAV 2020,* McMinville: Northwest UAV.

Octopus ISR Systems, n.d. *Epsilon 140 Dual Sensor Payload,* Marupe: Octopus ISR Systems.

Operation Phakisa, 2014. *Unlocking the Economic Potential of South Africa's Oceans,* Pretoria: Republic of South Africa.

Panagiotou, P., Fotiadis-Karras, S. & Yakinthos, K., 2018. Conceptual design of a Blended Wing Body MALE UAV. *Aerospace Science and Technology,* Volume 73, pp. 23-47.

Panagiotou, P., Kaparos, P., Salpingidou, C. & Yakinthos, K., 2016. Aerodynamic design of a MALE UAV. *Aerospace Science and Technology,* Volume 50, pp. 127-138.

Pitcher, M., 2018. *Ship tracking systems* [Interview] (17 June 2018).

Reuther, J. J. et al., 1999. Constrained Multipoint Aerodynamic Shape Optimization Using an Adjoint Formulation and Parallel Computers, Part 1. *Journal of Aircraft,* 36(1), pp. 51-60.

Reuther, J. J. et al., 1999. Constrained Multipoint Aerodynamic Shape Optimization Using an Adjoint Formulation and Parallel Computers, Part 2. *Journal of Aircraft,* 36(1), pp. 61-74.

Rocha, M. A. & Solaque, L. E., 2013. *Concept design for an unmanned aerial vehicle that will perform exploration missions in Colombia,* Compiegne: International Federation of Automatic Control.

Rotron Power Ltd., 2020. *Rotron RT600LTR-EXE.* [Online] Available at: http://www.rotronuav.com/engines/rt-600exe [Accessed 10 April 2019].

Rumsey, C., 2010. *1st AIAA CFD High Lift Predicition Workshop Summary,* Chicago: American Institute of Aeronautics and Astronautics.

Sadraey, M. H., 2013. *Aircraft Design: A Systems Engineering Approach.* 1st ed. West Sussex: John Wiley & Sons Ltd.

Schraader, L., 2013. *The impact of illegal fishing on South Africa's economy,* Potchefstroom: North-West University.

South African Civil Aviation Authority, 2017. *Our Strategic Intent.* [Online] Available at: http://www.caa.co.za/Pages/About%20Us/Our-Strategic-Intent.aspx [Accessed 10 June 2018].

South African Government, 2018. *Operation Phakisa.* [Online] Available at: http://www.operationphakisa.gov.za/Pages/Home.aspx [Accessed 8 June 2018].

Stofberg, J. F., 2019. *Commercialising Intellectual Property Emanating from Universities in the Wester Cape, South Africa,* Cape Town: Stellenbosch University.

Swart, P. D., 2020. *Sailplane fuselage aerodynamic optimization using CFD,* Potchefstroom: North-West University.

Torode, H., n.d. *Efficient Light Aircraft Deisng - Options from Gliding,* s.l.: BGA Technical Committee.

Tu, J., Yeoh, G.-H. & Liu, C., 2018. *Computational Fluid Dynamics: A Practical Approach.* Cambridge: Butterworth-Heinemann.

Tzanakis, A., 2014. *Duct Optimization using CFD software "ANSYS Fluent Adjoint Solver",* Goteborg: Chalmers University of Technology.

U.S. AIR FORCE, 2015. *MQ-9 Reaper.* [Online] Available at: https://www.af.mil/About-Us/Fact-Sheets/Display/Article/104470/mq-9-reaper/ [Accessed 5 June 2019].

UAV Factory, n.d. *Epsilon 140 Payload.* [Online] Available at: http://octopus.uavfactory.com/uav-payloads-equipment/epsilon-140 [Accessed 6 June 2019].

Versteeg, H. K. & Malalasekera, W., 2007. *An introduction to Computational Fluid Dynamics: The Finite Volume Method.* 2nd ed. Harlow: Pearson Education Limited.

Weibel, R. E., 2005. *Safety Considerations for Operation of Different Classes of Unmanned Aerial Vehicles in the National Airspace System,* Cambridge: Massachusetts Intstitute of Technology.

Weierman, J. R., 2010. *WINGLET DESIGN AND OPTIMIZATION FOR UAVS,* Stillwater: Oklahoma State University.

Wikipedia, n.d. *Denel Dynamics Bateleur.* [Online] Available at: https://en.wikipedia.org/wiki/Denel_Dynamics_Bateleur [Accessed 5 June 2019].

Wikipedia, n.d. *General Atomics MQ-9 Reaper.* [Online] Available at: https://en.wikipedia.org/wiki/General_Atomics_MQ-9_Reaper#/media/File:MQ-9_Reaper_taxis.jpg [Accessed 5 June 2019].

xflr5, 2019. *xflr5.* [Online] Available at: http://www.xflr5.tech/xflr5.htm [Accessed 16th December 2019].

APPENDIX A. Python Scripts Used for Various Calculations

APPENDIX A.1. Code for initial size and mass estimates of UAV

```
import math

W_payload = 50          # Payload weight [kg]
range = 2500             # Range requirement [km]
v_endurance = 125        # Endurance velocity [km/h]
D_value = 7200           # D parameter for fuel weight [km]

MTOW = 0.183 * (W_payload * range) ** 0.653

wing_span = 1.041 * MTOW ** 0.382

length = wing_span / 1.775

endurance_time = range / v_endurance

W_fuel = MTOW * (1 - math.exp(-range / D_value))

P_eng_max = 0.169 * MTOW ** 0.927

W_engine = P_eng_max / 2.3

W_airframe = MTOW - W_payload - W_fuel - W_engine

print('Maximum Take-Off Weight = {0:.2f} [kg]'.format(MTOW))
print('Wingspan = {0:.2f} [m]'.format(wing_span))
print('Length = {0:.2f} [m]'.format(length))
print('Endurance Time = {0:.2f} [hr]'.format(endurance_time))
print('Mass of fuel = {0:.2f} [kg]'.format(W_fuel))
print('Maximum Engine Power = {0:.2f} [kW]'.format(P_eng_max))
print('Mass of Engine = {0:.2f} [kg]'.format(W_engine))
print('Mass of Airframe (Empty + electronics) = {0:.2f} [kg]'.format(W_airfram
e))
```

APPENDIX A.2. Code for more detailed size and mass estimates of UAV

```
import math

from aerocalc import std_atm as ISA
from aerocalc import unit_conversion

import matplotlib.pyplot as plt

import numpy as np

W_S = np.arange(200, 1000, 5)     # Wing Loading Range to look at [N/m^2]

MTOW = 400.0                      # Maximum Take-Off Weight (Assumed) [kg]
V_stall = 25.0                    # Stall Speed Requirement at MTOW [m/s]
C_Lmax = 1.5                      # Maximum coefficient of lift (assumed)
S_TO = 1000.00                    # Runway roll distance requirement [m]
C_DG = 0.02                       # Coefficient of Drag on Ground
n_p = 0.5                         # Propeller efficiency on take-off
g = 9.81                          # Gravity constant
mu = 0.05                         # Friction Coefficient of Runway Surface
ROC_cs = 2.0                      # Rate of climb at cruise ceiling requirement
[m/s]
ROC_sc = 0.8                      # Rate of climb at service ceiling requirement
 [m/s]
n_pclimb = 0.7                    # Propeller efficiency during climb
e = 0.8                           # Aerodynamic Efficiency of wing
AR = 18.0                         # Aspect ratio of wing
C_LTO = 2.0                       # Take off coefficient of lift
LDmax = 25.0                      # Lift to drag ratio maximum
h_ac = 8000.0                     # Absolute ceiling requirement [m]
h_sc = 6000.0                     # Service ceiling requirement [m]
h_cs = 3500.0                     # Cruise ceiling requirement [m]

C_DOaircraft = 0.02               # Zero-Lift drag coefficient
C_DHLD = 0.005                    # High-Lift device drag coefficient
C_DLG = 0.009                     # Landing gear drag coefficient

C_Lg = C_Lmax / (1.2 ** 2.0)
V_TO = 1.2 * V_stall
K = 1.0 / (math.pi * e * AR)
C_DTO = C_DOaircraft + C_DHLD + C_DLG + K * (C_LTO ** 2.0)
print(K)

def sigma(h):
    h = unit_conversion.len_conv(h, from_units='m', to_units='ft')
    if 0 <= h <= 35999:
        dencorrection = (1 - 6.873 * 10 ** (-6.0) * h) ** 4.266
    elif 36000 <= h <= 65000:
```

```
        dencorrection = 0.2967 * math.exp(1.7355 - 4.8075 * 10 ** (-5) * h)
    else:
        dencorrection = 'Height is out of range of function, check height!'
    return dencorrection


sigma_sc = sigma(h_sc)
sigma_cs = sigma(h_cs)
sigma_ac = sigma(h_ac)
print(sigma_ac)


rho_sc = ISA.alt2density(h_sc, density_units='kg/m**3', alt_units='m')
rho_cs = ISA.alt2density(h_cs, density_units='kg/m**3', alt_units='m')
rho_ac = ISA.alt2density(h_ac, density_units='kg/m**3', alt_units='m')
print(rho_cs)

W_SVs = 0.5 * 1.225 * (V_stall ** 2.0) * C_LTO
W_SVsmat = np.array([W_SVs, W_SVs])
W_PSVsmat = np.array([0, 1])

W_PSTO = np.zeros(np.size(W_S))
W_PROC = np.zeros(np.size(W_S))
W_Psc = np.zeros(np.size(W_S))
W_Pcs = np.zeros(np.size(W_S))
W_Pac = np.zeros(np.size(W_S))

for i in range(0, np.size(W_S)):

    W_PSTO[i] = ((1.0 - math.exp(0.6 * 1.225 * g * C_DG * S_TO * (1.0 / W_S[i]
))) / (mu - (mu + (C_DG / C_Lg)) *
                                (math.exp(0.6 * 1.225 * g * C_DG * S_TO * (1.0
 / W_S[i])))))) * (n_p / V_TO)

    W_PROC[i] = 1.0 / ((ROC_cs / n_p) + math.sqrt(2.0 / (rho_cs * math.sqrt(3.
0 * C_DOaircraft / K))
                                            * W_S[i]) * (1.155 / (LDmax * n_p))
)

    W_Psc[i] = sigma_sc / ((ROC_sc / n_p) + math.sqrt(2.0 / (rho_sc * math.sqr
t(3.0 * C_DOaircraft / K)) * W_S[i]) *
                           (1.155 / (LDmax * n_p)))

    W_Pcs[i] = sigma_cs / ((ROC_cs / n_p) + math.sqrt(2.0 / (rho_cs * math.sqr
t(3.0 * C_DOaircraft / K))
                              * W_S[i]) * (1.155 / (LDmax * n_p)))

    W_Pac[i] = sigma_ac / (math.sqrt(2.0 / (rho_ac * math.sqrt(3.0 * C_DOaircr
aft / K)) * W_S[i]) * (1.155 / (LDmax * n_p)))
```

```
max_x_index = np.argmin(np.abs(W_S - W_SVs))

min_y_matrix = np.array([W_PSTO[max_x_index], W_PROC[max_x_index], W_Psc[max_x
_index],
                         W_Pcs[max_x_index], W_Pac[max_x_index]])

print('Wing Loading with 5% Safety Margin = {0:.2f} [$N/m^2$]'.format(W_SVs /
1.05))
print('Wing Loading with 5% Safety Margin = {0:.2f} [$kg/m^2$]'.format(W_SVs/
(1.05 * 9.81)))
print('Power Loading with 5% Safety Margin = {0:.2f} [N/W]'.format(np.min(min_
y_matrix) / 1.05))
print('Required Wing Area with assumed MTOW = {0:.5f} [$m^2$]'.format((MTOW *
9.81) / (W_SVs / 1.05)))
print('Required Engine Power with assumed MTOW = {0:.2f} [kW]'.format((MTOW *
9.81) / (np.min(min_y_matrix) / 1.05)/1000))

# <editor-fold desc="Plotting the Data">

# Plot the data
plt.plot(W_SVsmat, W_PSVsmat, 'r', linewidth=1, label='Stall Speed')
plt.plot(W_S, W_PROC, 'b', linewidth=1, label='Rate of Climb')
plt.plot(W_S, W_PSTO, 'g', linewidth=1, label='Take-Off Run')
plt.plot(W_S, W_Psc, 'c', linewidth=1, label='Service Ceiling')
plt.plot(W_S, W_Pcs, 'm', linewidth=1, label='Cruise Ceiling')
plt.plot(W_S, W_Pac, 'k', linewidth=1, label='Absolute Ceiling')
plt.scatter(W_SVs / 1.05, np.min(min_y_matrix) / 1.05, marker='o', s=80, color
='blue',
            label='Selected Loadings Point\n with 5% Safety Margin')
plt.annotate('REQUIREMENTS NOT MET IN RED ZONE', (0.7, 0.96), xycoords='axes f
raction')

# Set axis limits, labels, legends etc
plt.ylim(0, max(max(W_PSTO), max(W_PROC), max(W_Psc), max(W_Pcs), max(W_Pac)))
plt.xlim(min(W_S), W_SVs * 1.05)
plt.yticks(np.arange(0, max(max(W_PSTO), max(W_PROC), max(W_Psc), max(W_Pcs),
max(W_Pac)), 0.005))
plt.xticks(np.arange(min(W_S), W_SVs*1.05, 5), rotation='vertical')
plt.title('Wing VS Power Loading Requirements', fontsize=15)
plt.xlabel('Wing Loading (W/S) [$N/m^2$]', fontsize=12)
plt.ylabel('Power Loading (W/P) [N/W]', fontsize=12)
plt.grid(True)
plt.legend()


# Fill between block for plot
plt.fill_between(W_S, W_PROC, 1, facecolor='red', alpha=0.2)
```

```
plt.fill_between(W_S, W_PSTO, 1, facecolor='red', alpha=0.2)
plt.fill_between(W_S, W_Psc, 1, facecolor='red', alpha=0.2)
plt.fill_between(W_S, W_Pcs, 1, facecolor='red', alpha=0.2)
plt.fill_between(W_S, W_Pac, 1, facecolor='red', alpha=0.2)
plt.fill_betweenx(W_PSVsmat, W_SVsmat, 900, facecolor='red', alpha=0.2)

# Show plot as maximized
mng = plt.get_current_fig_manager()
mng.window.showMaximized()
plt.show()
# </editor-fold>
```

APPENDIX A.3. Code for CFD Simulation Inputs using Cruise Condition

```
from aerocalc import std_atm as ISA
from aerocalc import unit_conversion
from aerocalc import airspeed
import math

altitude = 3500.0       #  Altitude [m]
speed = 35.0            # Speed [m/s]
area = 5.5              # Wing Area [m**2]
mass = 280.00           # UAV Mass

density = ISA.alt2density(altitude, alt_units="m",density_units="kg/m**3")

temp = ISA.alt2temp(altitude, alt_units="m", temp_units="K")

pressure = ISA.alt2press(altitude, alt_units="m", press_units="pa")

# mach = airspeed.cas_alt2mach(speed, altitude, speed_units="m/s", alt_units="
m")

mach2 = airspeed.tas2mach(speed, temp, altitude,
temp_units="K", alt_units="m", speed_units="m/s")

Clreq = (mass * 9.81 * 2) / (density * speed**2.0 * area)

print('Density = {0:0.3f} kg/m**3'.format(density))
print('Temperature = {0:0.2f} K'.format(temp))
print('Pressure = {0:0.2f} Pa'.format(pressure))
# print('Mach = {0:0.3f}'.format(mach))
print('Mach = {0:0.3f}'.format(mach2))
print('Required Cl = {0:0.3f}'.format(Clreq))
```

APPENDIX B. INITIAL UAV DESIGN INFORMATION

APPENDIX B.1. WING AEROFOIL COMPARISON

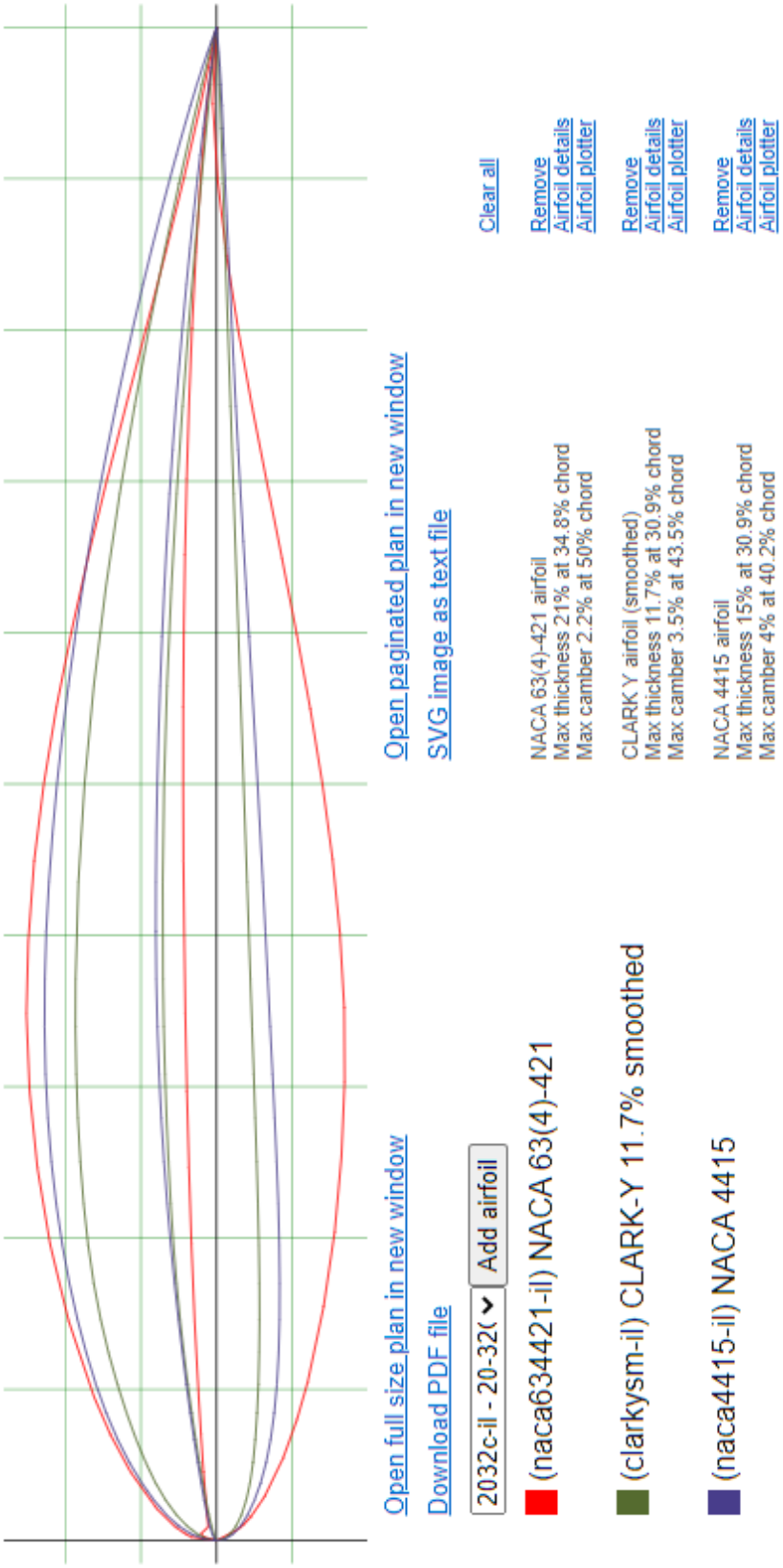

Polars for (naca634421-il,clarkysm-il,naca4415-il)

Plot	Airfoil	Reynolds #	Ncrit	Max Cl/Cd	Description	Source	
☐	naca634421-il	50,000	9	3.8 at α=12.75°	Mach=0 Ncrit=9	Xfoil prediction	Details
☐	naca634421-il	50,000	5	9.4 at α=14.25°	Mach=0 Ncrit=5	Xfoil prediction	Details
☐	naca634421-il	100,000	9	24.4 at α=13.25°	Mach=0 Ncrit=9	Xfoil prediction	Details
☐	naca634421-il	100,000	5	35 at α=8.25°	Mach=0 Ncrit=5	Xfoil prediction	Details
☐	naca634421-il	200,000	9	61.4 at α=9.75°	Mach=0 Ncrit=9	Xfoil prediction	Details
☐	naca634421-il	200,000	5	63 at α=8°	Mach=0 Ncrit=5	Xfoil prediction	Details
☑	naca634421-il	500,000	9	95.3 at α=8°	Mach=0 Ncrit=9	Xfoil prediction	Details
☐	naca634421-il	500,000	5	90.8 at α=7.5°	Mach=0 Ncrit=5	Xfoil prediction	Details
☑	naca634421-il	1,000,000	9	119.1 at α=7.25°	Mach=0 Ncrit=9	Xfoil prediction	Details
☐	naca634421-il	1,000,000	5	109.7 at α=6.5°	Mach=0 Ncrit=5	Xfoil prediction	Details
☐	clarkysm-il	50,000	9	30 at α=10°	Mach=0 Ncrit=9	Xfoil prediction	Details
☐	clarkysm-il	50,000	5	35.3 at α=7.75°	Mach=0 Ncrit=5	Xfoil prediction	Details
☐	clarkysm-il	100,000	9	52.5 at α=7°	Mach=0 Ncrit=9	Xfoil prediction	Details
☐	clarkysm-il	100,000	5	53.5 at α=5.75°	Mach=0 Ncrit=5	Xfoil prediction	Details
☐	clarkysm-il	200,000	9	74.4 at α=4.5°	Mach=0 Ncrit=9	Xfoil prediction	Details
☐	clarkysm-il	200,000	5	70.1 at α=4.75°	Mach=0 Ncrit=5	Xfoil prediction	Details
☑	clarkysm-il	500,000	9	101.6 at α=3.5°	Mach=0 Ncrit=9	Xfoil prediction	Details
☐	clarkysm-il	500,000	5	90.2 at α=4°	Mach=0 Ncrit=5	Xfoil prediction	Details
☑	clarkysm-il	1,000,000	9	119.6 at α=3°	Mach=0 Ncrit=9	Xfoil prediction	Details
☐	clarkysm-il	1,000,000	5	106.2 at α=5.75°	Mach=0 Ncrit=5	Xfoil prediction	Details
☐	naca4415-il	50,000	9	7.4 at α=9°	Mach=0 Ncrit=9	Xfoil prediction	Details
☐	naca4415-il	50,000	5	27.4 at α=8.25°	Mach=0 Ncrit=5	Xfoil prediction	Details
☐	naca4415-il	100,000	9	48.4 at α=9°	Mach=0 Ncrit=9	Xfoil prediction	Details
☐	naca4415-il	100,000	5	50.7 at α=6.25°	Mach=0 Ncrit=5	Xfoil prediction	Details
☐	naca4415-il	200,000	9	71.1 at α=6.5°	Mach=0 Ncrit=9	Xfoil prediction	Details
☐	naca4415-il	200,000	5	68.2 at α=5.75°	Mach=0 Ncrit=5	Xfoil prediction	Details
☑	naca4415-il	500,000	9	97 at α=5.75°	Mach=0 Ncrit=9	Xfoil prediction	Details
☐	naca4415-il	500,000	5	90.4 at α=5.5°	Mach=0 Ncrit=5	Xfoil prediction	Details
☑	naca4415-il	1,000,000	9	119.4 at α=5.5°	Mach=0 Ncrit=9	Xfoil prediction	Details
☐	naca4415-il	1,000,000	5	109.1 at α=4.75°	Mach=0 Ncrit=5	Xfoil prediction	Details

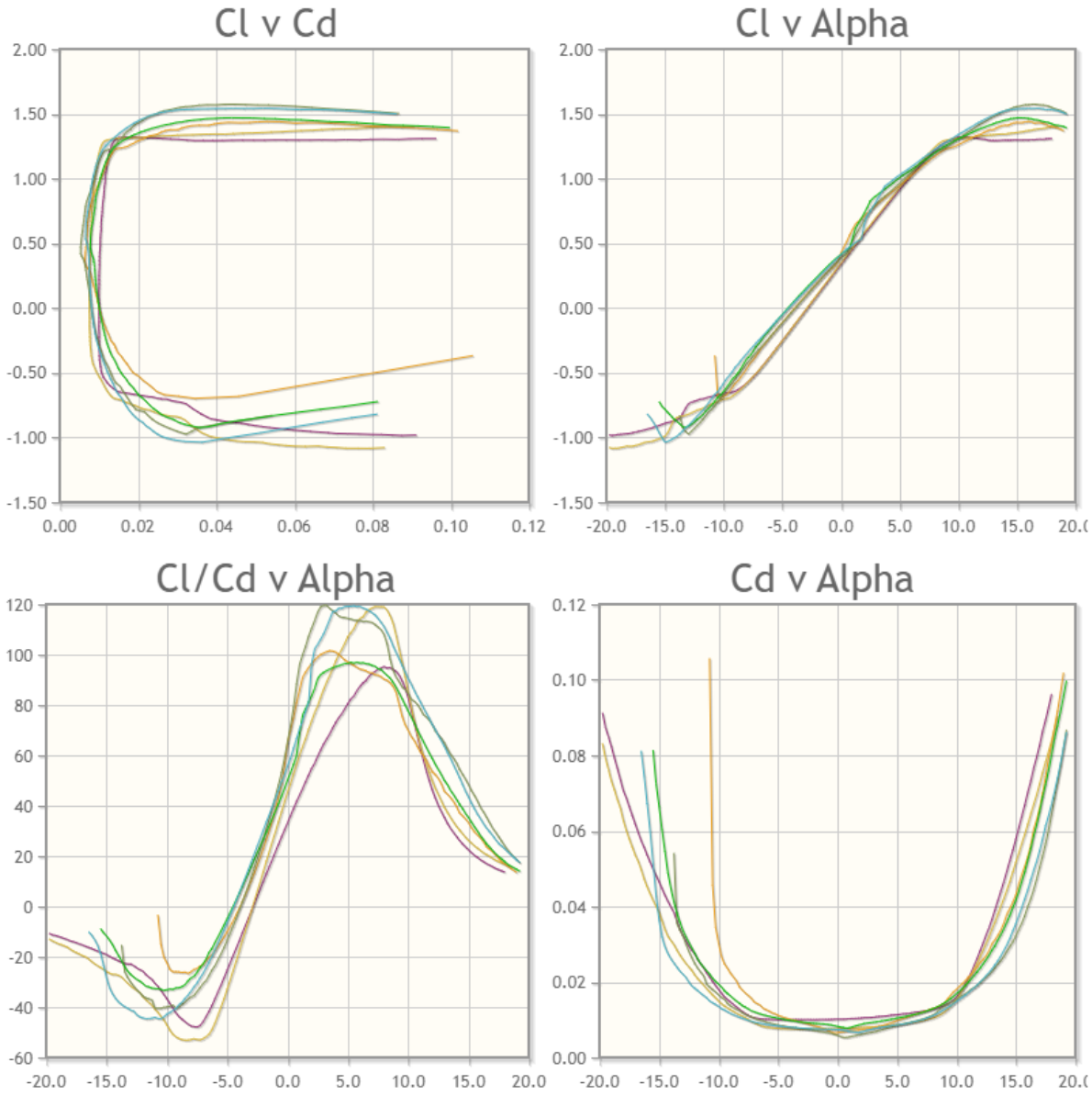
Cl v Cd
2.00
1.50
1.00
0.50
0.00
-0.50
-1.00
-1.50
0.00
0.02
0.04
0.06
0.08
0.10
0.12
Cl v Alpha
2.00
1.50
1.00
0.50
0.00
-0.50
-1.00
-1.50
-20.0
-15.0
-10.0
-5.0
0.0
5.0
10.0
15.0
Cl/Cd v Alpha
120
100
80
60
40
20
0
-20
-40
-60
-20.0
-15.0
-10.0
-5.0
0.0
5.0
10.0
15.0
20.0
Cd v Alpha
0.12
0.10
0.08
0.06
0.04
0.02
0.00
-20.0
-15.0
-10.0
-5.0
0.0
5.0
10.0
15.0

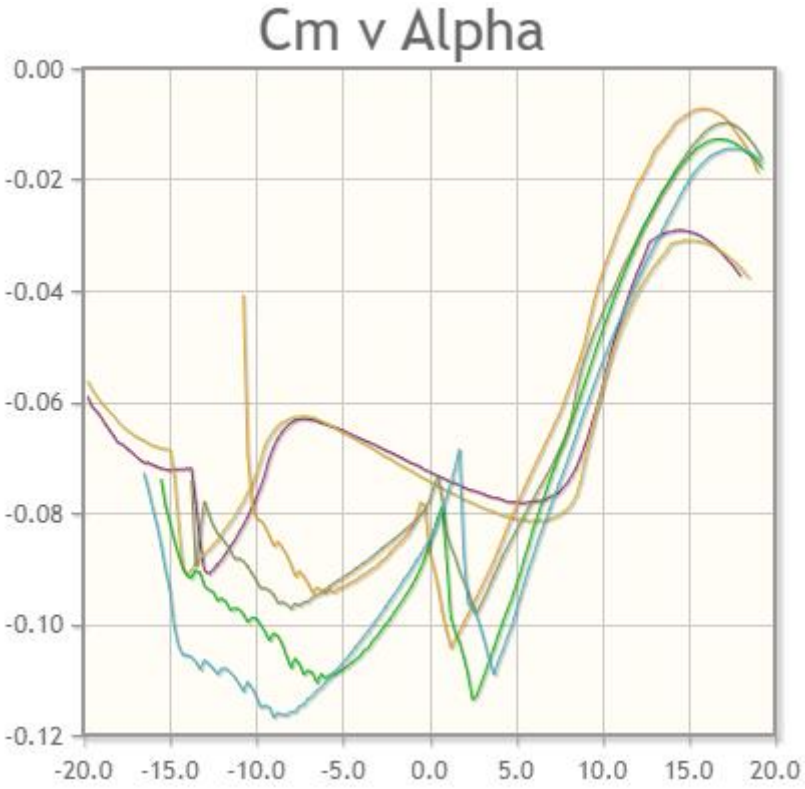
Cm v Alpha
0.00
-0.02
-0.04
-0.06
-0.08
-0.10
-0.12
-20.0
-15.0
-10.0
-5.0
0.0
5.0
10.0
15.0
20.0

APPENDIX C. CALCULATIONS FOR REQUIRED OPERATIONAL ENVELOPE

APPENDIX C.1. CALCULATIONS FOR REQUIREMENTS OF INITIAL UAV DESIGN

ITEMS IN THIS COLOUR ARE REQUIRED INPUTS

ITEMS IN THIS COLOUR ARE THE MAIN REQUIRED CALCULATIONS

COMMENTS HAVE NO BACKGROUND COLOUR

$LDMAX := 27$	MAXIMUM LIFT OVER DRAG RATIO AS DETERMINED FROM CFD
$\eta_p := 75\ \%$	PROPELLER ASSUMED EFFCIENCY
$C := 600 \frac{g}{kW\ hr} = 0.0002 \frac{g}{J}$	ASSUMED CRUISING FUEL CONSUMPTION
$V_f := 120\ L$	FUEL VOLUME IN LITRES
$\rho_f := 740 \frac{kg}{m^3}$	TYPICAL ENGINE FUEL DENSITY
$MTOW := 400\ kg$	MAXIMUM AIRCRAFT TAKEOFF WEIGHT
$C_{Lmax} := 1.5$	MAXIMUM COEFFICIENT OF LIFT AS DETERMINED FROM CFD
$S := 5.578\ m^2$	WING REFERENCE AREA
$\rho := 0.863 \frac{kg}{m^3}$	AIR DENSITY (TO BE CHECKED AT VARIOUS HEIGHT DENSITIES)
$\rho_{sea} := 1.225 \frac{kg}{m^3}$	AIR DENSITY AT SEA LEVEL
$\rho_{service} := 0.66 \frac{kg}{m^3}$	AIR DENSITY AT SERVICE CEILING
$\rho_{absolute} := 0.525 \frac{kg}{m^3}$	AIR DENSITY AT ABSOLUTE CEILING
$P_{max} := 40\ kW$	ENGINE POWER AVAILABLE AT SEA LEVEL
$C_{D0} := 0.03$	DRAG COEFFICIENT AT 0 AOA AS DETERMINED BY CFD
$e_w := 0.85$	ASSUMED WING EFFICIENCY FACTOR
$b := 10\ m$	WING SPAN
$C_{LCRUISE} := 0.98876$	APPROXIMATE CL AT CRUISE DETERMINED FROM CFD
$C_{DCRUISE} := 0.036436$	APPROXIMATE CD AT CRUISE DETERMINED FROM CFD

CALCULATIONS BELOW

$m_f := V_f \cdot \rho_f = 88.8\ kg$ CALCULATED MASS OF FUEL

$W := MTOW\ g_e = 3922.66\ N$ CALCULATED AIRCRAFT MAXIMUM WEIGHT

$\left(\frac{W}{S}\right) = 703.2377\ \frac{N}{m^2}$ CALCULATED WING LOADING

$\frac{W}{P_{max}} = 0.0981\ \frac{N}{watt}$ CALCULATED POWER LOADING

$AR := \frac{b^2}{S} = 17.9276$ CALCULATED ASPECT RATIO

$K := \frac{1}{\pi \cdot e_w \cdot AR} = 0.0209$ CALCULATED INDUCED DRAG COEFFICIENT

$V_{cmax} := \sqrt{\frac{2 \cdot MTOW\ g_e}{C_{LCRUISE} \cdot S \cdot \rho}} = 40.599\ \frac{m}{s}$ Maximum cruise velocity

$V_{cmin} := \sqrt{\frac{2 \cdot (MTOW - m_f)\ g_e}{C_{LCRUISE} \cdot S \cdot \rho}} = 35.81\ \frac{m}{s}$ Miniumum cruise velocity

$V_S := \sqrt{\frac{2 \cdot \left(\frac{W}{S}\right)}{C_{Lmax} \cdot \rho_{sea}}} = 27.67\ \frac{m}{s}$ CALCULATED STALL SPEED

$R := \frac{LDMAX \cdot \eta_P}{1.2 \cdot C\ g_e} \cdot \ln\left(\frac{1}{1 - \frac{m_f}{MTOW}}\right) = 2592\ km$ CALCULATED RANGE

$T_{TO} := \frac{0.5 \cdot P_{max}}{V_S} = 722.9\ N$ CALCULATED AVERAGE TAKE-OFF THRUST

$S_{TO} := \frac{1.21 \cdot \left(\frac{W}{S}\right)}{g_e \cdot \rho \cdot C_{Lmax} \cdot \left(\frac{T_{TO}}{W}\right)} \cdot 1.5 = 545.58\ m$ CALCULATED TAKE-OFF GROUND RUN

$E := \frac{\eta_P}{C\ g_e} \cdot \sqrt{2 \cdot \rho \cdot S} \cdot \frac{C_{LCRUISE}^{\frac{3}{2}}}{C_{DCRUISE}} \cdot \left(\left((MTOW - m_f)\ g_e\right)^{-0.5} - \left(MTOW\ g_e\right)^{-0.5}\right) = 22.8\ hr$ CALCULATED ENDURANCE

$ROC_{service} := \eta_P \cdot \left(\frac{P_{max} \cdot \frac{\rho_{service}}{\rho_{sea}}}{W} - \sqrt{\frac{2}{\rho_{service} \cdot \sqrt{\frac{3 \cdot C_{D0}}{K}}} \cdot \frac{W}{S}} \cdot \frac{1.155}{LDMAX \cdot \eta_P}\right) = 2.7498\ \frac{m}{s}$ CALCULATED RATE OF CLIMB AT SERVICE CEILING

$ROC_{absolute} := \eta_P \cdot \left(\frac{P_{max} \cdot \frac{\rho_{absolute}}{\rho_{sea}}}{W} - \sqrt{\frac{2}{\rho_{absolute} \cdot \sqrt{\frac{3 \cdot C_{D0}}{K}}} \cdot \frac{W}{S}} \cdot \frac{1.155}{LDMAX \cdot \eta_P}\right) = 1.7408\ \frac{m}{s}$ CALCULATED RATE OF CLIMB AT ABSOLUTE CEILING

APPENDIX C.2. CALCULATIONS FOR REQUIREMENTS OF FINAL UAV DESIGN

ITEMS IN THIS COLOUR ARE REQUIRED INPUTS

ITEMS IN THIS COLOUR ARE THE MAIN REQUIRED CALCULATIONS

COMMENTS HAVE NO BACKGROUND COLOUR

$LDMAX := 28.8$	MAXIMUM LIFT OVER DRAG RATIO AS DETERMINED FROM CFD
$\eta_p := 75\ \%$	PROPELLER ASSUMED EFFCIENCY
$C := 600 \frac{g}{kW\ hr} = 0.0002 \frac{g}{J}$	ASSUMED CRUISING FUEL CONSUMPTION
$V_f := 120\ L$	FUEL VOLUME IN LITRES
$\rho_f := 740 \frac{kg}{m^3}$	TYPICAL ENGINE FUEL DENSITY
$MTOW := 400\ kg$	MAXIMUM AIRCRAFT TAKEOFF WEIGHT
$C_{Lmax} := 1.5$	MAXIMUM COEFFICIENT OF LIFT AS DETERMINED FROM CFD
$S := 5.578\ m^2$	WING REFERENCE AREA
$\rho := 0.863 \frac{kg}{m^3}$	AIR DENSITY (TO BE CHECKED AT VARIOUS HEIGHT DENSITIES)
$\rho_{sea} := 1.225 \frac{kg}{m^3}$	AIR DENSITY AT SEA LEVEL
$\rho_{service} := 0.66 \frac{kg}{m^3}$	AIR DENSITY AT SERVICE CEILING
$\rho_{absolute} := 0.525 \frac{kg}{m^3}$	AIR DENSITY AT ABSOLUTE CEILING
$P_{max} := 40\ kW$	ENGINE POWER AVAILABLE AT SEA LEVEL
$C_{D0} := 0.03$	DRAG COEFFICIENT AT 0 AOA AS DETERMINED BY CFD
$e_w := 0.85$	ASSUMED WING EFFICIENCY FACTOR
$b := 10\ m$	WING SPAN
$C_{LCRUISE} := 1.166$	APPROXIMATE CL AT CRUISE DETERMINED FROM CFD
$C_{DCRUISE} := 0.040427$	APPROXIMATE CD AT CRUISE DETERMINED FROM CFD

CALCULATIONS BELOW

$m_f := V_f \cdot \rho_f = 88.8\ kg$ CALCULATED MASS OF FUEL

$W := MTOW\ g_e = 3922.66\ N$ CALCULATED AIRCRAFT MAXIMUM WEIGHT

$\left(\frac{W}{S}\right) = 703.2377\ \frac{N}{m^2}$ CALCULATED WING LOADING

$\frac{W}{P_{max}} = 0.0981\ \frac{N}{watt}$ CALCULATED POWER LOADING

$AR := \frac{b^2}{S} = 17.9276$ CALCULATED ASPECT RATIO

$K := \frac{1}{\pi \cdot e_w \cdot AR} = 0.0209$ CALCULATED INDUCED DRAG COEFFICIENT

$V_{cmax} := \sqrt{\frac{2 \cdot MTOW\ g_e}{C_{LCRUISE} \cdot S \cdot \rho}} = 37.3862\ \frac{m}{s}$ Maximum cruise velocity

$V_{cmin} := \sqrt{\frac{2 \cdot (MTOW - m_f)\ g_e}{C_{LCRUISE} \cdot S \cdot \rho}} = 32.98\ \frac{m}{s}$ Miniumum cruise velocity

$V_S := \sqrt{\frac{2 \cdot \left(\frac{W}{S}\right)}{C_{Lmax} \cdot \rho_{sea}}} = 27.67\ \frac{m}{s}$ CALCULATED STALL SPEED

$R := \frac{LDMAX \cdot \eta_P}{1.2 \cdot C\ g_e} \cdot \ln\left(\frac{1}{1 - \frac{m_f}{MTOW}}\right) = 2765\ km$ CALCULATED RANGE

$T_{TO} := \frac{0.5 \cdot P_{max}}{V_S} = 722.9\ N$ CALCULATED AVERAGE TAKE-OFF THRUST

$S_{TO} := \frac{1.21 \cdot \left(\frac{W}{S}\right)}{g_e \cdot \rho \cdot C_{Lmax} \cdot \left(\frac{T_{TO}}{W}\right)} \cdot 1.5 = 545.58\ m$ CALCULATED TAKE-OFF GROUND RUN

$E := \frac{\eta_P}{C\ g_e} \cdot \sqrt{2 \cdot \rho \cdot S} \cdot \frac{C_{LCRUISE}^{\frac{3}{2}}}{C_{DCRUISE}} \cdot \left(\left((MTOW - m_f)\ g_e\right)^{-0.5} - \left(MTOW\ g_e\right)^{-0.5}\right) = 26.3\ hr$ CALCULATED ENDURANCE

$ROC_{service} := \eta_P \cdot \left(\frac{P_{max} \cdot \frac{\rho_{service}}{\rho_{sea}}}{W} - \sqrt{\frac{2}{\rho_{service} \cdot \sqrt{\frac{3 \cdot C_{D0}}{K}}} \cdot \frac{W}{S}} \cdot \frac{1.155}{LDMAX \cdot \eta_P}\right) = 2.8355\ \frac{m}{s}$ CALCULATED RATE OF CLIMB AT SERVICE CEILING

$ROC_{absolute} := \eta_P \cdot \left(\frac{P_{max} \cdot \frac{\rho_{absolute}}{\rho_{sea}}}{W} - \sqrt{\frac{2}{\rho_{absolute} \cdot \sqrt{\frac{3 \cdot C_{D0}}{K}}} \cdot \frac{W}{S}} \cdot \frac{1.155}{LDMAX \cdot \eta_P}\right) = 1.8369\ \frac{m}{s}$ CALCULATED RATE OF CLIMB AT ABSOLUTE CEILING